A Molecular Engineering Approach: Multi-Functional Binders Design for Lithium-Sulfur Battery

Jiaxu Qin

A dissertation

submitted in partial fulfillment of the

requirements for the degree of

Doctor of Philosophy

University of Washington

2022

Reading Committee:

Alex K.-Y. Jen, Chair

Jihui Yang

Xiaosong Li

Program Authorized to Offer Degree

Molecular Engineering and Sciences

University of Washington

Abstract

A Molecular Engineering Approach: Multi-Functional Binders Design for Lithium-Sulfur Battery

Jiaxu Qin

Chair of the Supervisory Committee:

Alex K.-Y. Jen

Materials Science & Engineering

Lithium-sulfur (Li-S) batteries have attracted great attention as the next-generation batteries due to their high theoretical gravimetric energy density of ~2510 Wh/kg in comparison to ~400 Wh/kg for lithium-ion (Li-ion) batteries. Besides, sulfur has advantages, including abundant reserves, low price, and environmental friendliness. However, the practical application of Li-S batteries is hindered by several challenges of sulfur cathode such as dissolution of lithium polysulfides (LiPSs) in the electrolyte, the cracks issue caused by volume change of active materials during cycling, and poor conductivity, which reduce the capacity and cycle life of

practical cells significantly. Even worse, these challenges become more severe when fabricating high-loading sulfur cathode, which is the path to the commercial application of Li-S batteries.

In this doctoral dissertation, I have developed a "bottom-up" molecular engineering strategy to achieve high-loading, long-cycle-life sulfur cathode based on a multi-functional binders design. To confine LiPSs, Chapter 2 demonstrates the design and synthesis of novel binder PENDI based on redox active naphthalene diimide (NDI), which confines LiPSs through chemical interactions and redox mediation effect. The detailed redox mediation mechanism of PENDI to reduce the accumulation of LiPSs is proposed, providing a promising strategy to prevent the dissolution of LiPSs *via* an organic redox mediator. Chapter 3 presents the strategy to mitigate cracks by reversibly crosslinking PENDI with triPy crosslinker based on pi-pi interaction. The resulting PENDI/triPy supramolecular network demonstrates not only enhanced mechanical properties, but also tunable self-healing properties. Besides, a strategy to decouple macro-scale properties from the covalent structure of supramolecular polymers is reported to tune both mechanical and self-healing properties over a wide range, without changing the structure of polymer components. Building upon Chapter 2 and Chapter 3, Chapter 4 integrates the molecular designs into sulfur cathode and details the optimization of high-loading, long-cycle-life sulfur cathodes by mechanically stabilizing sulfur cathode with PENDI-based binders. By utilizing triPy crosslinker and PVDF additive, both the toughness and stiffness of PENDI-based binders are dramatically improved, enabling the fabrication of sulfur cathode with high areal discharge capacity (> 4.1 mAh/cm^2, C/10 rate) and high cathode discharge capacity (> 10 mAh).

Table of Contents

LIST OF FIGURES

LIST OF TABLES

ACKNOWLEDGEMENTS

I would like to thank everyone who has worked with me, mentored me, and supported me during my study at University of Washington. Thank you so much!

First, I would like to express my sincere gratitude to my advisor Dr. Alex Jen for guiding and supporting me in the past several years. Dr. Jen is always passionate and energetic. His dedication to research and fearless courage when facing challenges inspire me a lot. Thank you to Dr. Jihui Yang for advising me during our cooperative project and supporting me for the training in his lab. Thank you to Dr. Sei-Hum Jang for not only mentoring me about my research but also teaching me about integrity, critical thinking, and communication skills, *etc*. The valuable characteristics and skills that I have learned and seen from you all will keep guiding my future life. I really appreciate it.

Next, I would like to thank my fellow students Dr. Dion Hubble, Dr. Ray Lin, Dr. April Li, and Dr. Ian Murphy who worked closely in my PhD. Thanks Dion and Ray, as you are the ones that not only taught me skills in battery fabrication and materials synthesis, but also materially contributed to the experiments in my dissertation. Thank you to April for sharing your valuable insights about batteries.

I would like to thank Dr. Alshakim Nelson, Paul Neubert, and Doug Ballard from my department Molecular Engineering & Sciences Institute (MolES). Thanks for your help, patience, and support which make my experience in MolES wonderful.

Of course, I must thank my parents and sisters. Thank you for your love and support. Thank you to my lovely nephews and nieces. You are the sunshine in my life which helps me get through the rainy days.

Thank you to my dear friends Moke Mao, Yanjun Yang, Yunsong Zhang, Rongchao Lin, Yiyu Tian, Liang Pan, Siyang Li, Jingshuo Feng, Shaoquan Yu, Yongli Huang, Yangyang Wang who have shared my highs and lows.

The work in this dissertation is supported by the Department of Energy, Office of Energy Efficiency and Renewable Energy (EERE), under Award Number DE-EE0007791. Besides, thank you for the support from Clean Energy Institute (CEI) Graduate Fellowship.

Thank you all!

CHAPTER 1: INTRODUCTION

1.1 BATTERIES

The inevitable depletion of fossil fuel and severe environmental pollution and greenhouse effect caused by burning fossil fuel have made the need for clean energies extremely urgent. Energy storage is playing an increasingly important role today than any time before. Low-cost energy storage devices with high energy density are highly desired to stabilize the supply of clean energy and accelerate the developments of electric vehicles, portable electronic devices, *etc*.[1] Since the first introduction in 1991, commercial lithium-ion (Li-ion) batteries have enabled the tremendous developments of portable electronic devices and EVs.[2,3] Compared to alternative metal-ion batteries, Li-ion batteries offer the highest specific energies and highest power densities due to the nature of lithium as the lowest reduction potential of any element and the third lightest element.[4]

1.1.1 Basic Components of Li-ion Batteries

Rechargeable Li-ion Batteries are devices to reversibly convert between chemical energy and electrical energy. As shown in **Figure 1-1**, the typical components of Li-ion batteries consist of graphite anode, metal oxide cathode, organic carbonate electrolyte, and separator.[5] During discharge process, the anode and cathode undergo half-cell reactions to produce electrical energy and supply it to external circuit. Meanwhile, Li^+ will migrate inside the electrolyte between electrodes to balance the current flow. A separator is used to prevent internal short circuit by physically separating electrodes and allowing the migration of ions. Besides the nature of half-cell reactions, the cycle life of the batteries also highly relies on the mechanical integration of cell and

electrode architectures. Taking the graphite anode for example, graphite undergoes an intercalation half-cell reaction to deliver a specific discharge capacity of 372 mAh/g. To maintain the electron pathway for the half-cell reaction, conductive carbon is usually added to connect graphite particles. Meanwhile, a robust polymeric binder is used to glue the anode materials together and consequently enhances the mechanical integrity and stabilize the discharge capacity of anode.

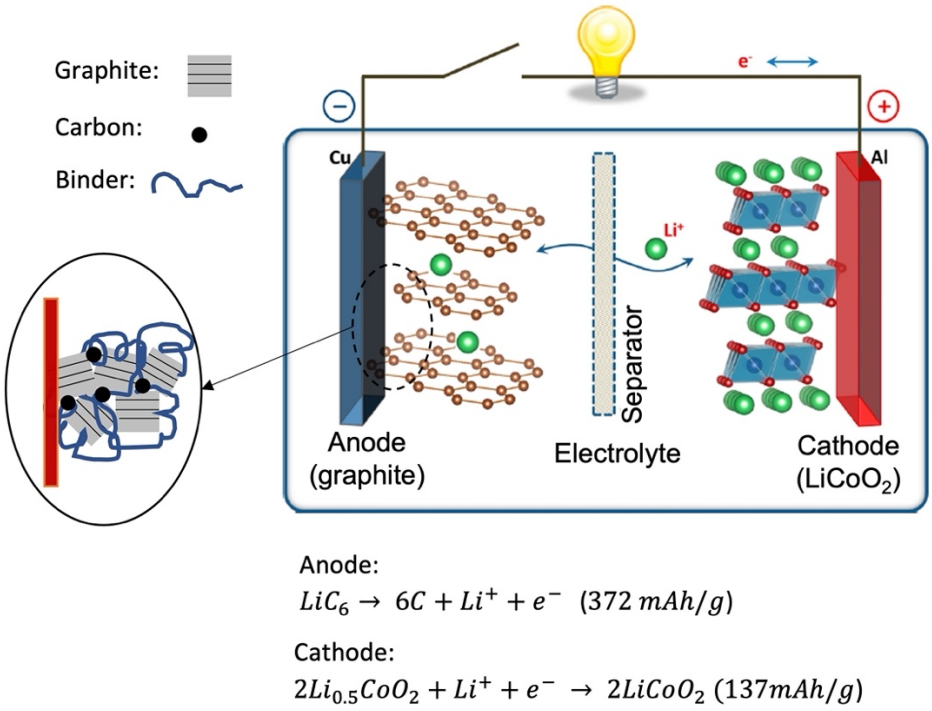

Figure 1-1. The half-cell reactions and device configuration of Li-ion batteries with $LiCoO_2$ cathode and graphite anode.[6,7]

1.1.2 Performance Metrics

Different batteries share the similar performance metrics, which are used to evaluate their performances, and understand the reaction mechanisms. As introduced in **Section 1.1.1**, Li-ion batteries charge and discharge through conducting the half-cell reactions. Due to the difference in electrode potential, an open-circuit voltage (OCV, measured in V) is formed between anode and

cathode. Due to the existence of internal battery resistance R_b, the operational voltages at discharge (V_{dis}) and charge (V_{ch}) processes are different from OCV (shown in **Equation 1-1**, **Equation 1-2**). During the discharge process, the operational voltage V_{dis} is $R_b I_{dis}(q, I_{dis})$ lower than VOC, where q, I_{dis} represent the state of charge and ionic current, respectively. During the charge process, the operational voltage V_{ch} is $R_b I_{ch}(q, I_{ch})$ higher than VOC. $R_b I_{dis}$ and $R_b I_{ch}$ represent the polarization (measured in V) during discharge and charge processes of the batteries.

$$V_{dis} = VOC - R_b I_{dis}(q, I_{dis}) \qquad (1-1)$$

$$V_{ch} = VOC + R_b I_{ch}(q, I_{ch}) \qquad (1-2)$$

Capacity is used to measure the electric energy that batteries can release during discharge process and store during charge process, measured in ampere-hour (Ah), or mAh. Specific capacity (mAh/g) and volumetric capacity (mAh/cm^3) represent the electric energy per mass or per volume. The theoretical capacities of electrodes are the specific capacity when the half-cell reactions are fully conducted theoretically. From the prospective of the full cell, we also care about the energy density of the cell, which is calculated by integrating voltage over capacity. The specific energy (Wh/kg) and energy density (Wh/L) are obtained based on specific capacity and volumetric capacity. Besides, other important definitions and terminologies used in batteries are summarized in **Table 1-1**.

Table 1-1. Definition and explanation of important performance metrics for batteries.

Name	Unit	Definition/Explanation
Active materials	unitless	The materials that conduct the half-cell reactions in the electrodes.
Mass loading	mg/cm^2	Mass of active materials coated on the current collector per unit area.
Electrical conductivity	S/cm	The ability of material to conduct electron.
Ionic conductivity	S/cm	The ability of material to conduct ion and anion through electrolyte.

C-rate	h^{-1}	A C-rate is used to represent discharge current to normalize against battery capacity. C-rate measures the rate at which a battery is discharged relative to its maximum capacity. For example, 1C rate and C/10 rate mean that the discharge currents will discharge the entire battery in 1 hour and 10 hours, respectively.
Cycle	unitless	One full charge, followed by one full discharge.
Coulombic efficiency	unitless (%)	For particular cycle, the coulombic efficiency represents the ratio between discharge capacity to charge capacity.
Capacity retention	unitless (%)	Capacity retention represents the ratio between a particular cycle to that of an earlier cycle.
Cycle life	unitless	The number of completed cycles before the capacity retention drops below a target value (80% for example).

1.2 LITHIUM-SULFUR BATTERIES

Despite their dominating applications in rechargeable batteries, Li-ion batteries are reaching their performance and cost limits after having been studied and optimized for decades, which can't meet the urgent desire for energy storage devices with lower cost and higher energy density, especially in electric vehicles (EVs). More and more researchers are looking for solutions beyond traditional Li-ion batteries. Among the "beyond-lithium" systems, lithium-sulfur (Li-S) batteries are receiving great attention due to their high theoretical gravimetric energy density of ~2510 Wh/kg, which is up to five-fold compared to conventional Li-ion batteries (**Figure 1-2**).[8,9] The sulfur cathode delivers theoretical specific discharge capacity as high as 1675 mAh/g,[10] which is comparable with lithium metal anode with theoretical specific discharge capacity of 3860 mAh/g. Besides, sulfur has advantages, including abundant reserves, low price, and environmental friendliness.[11]

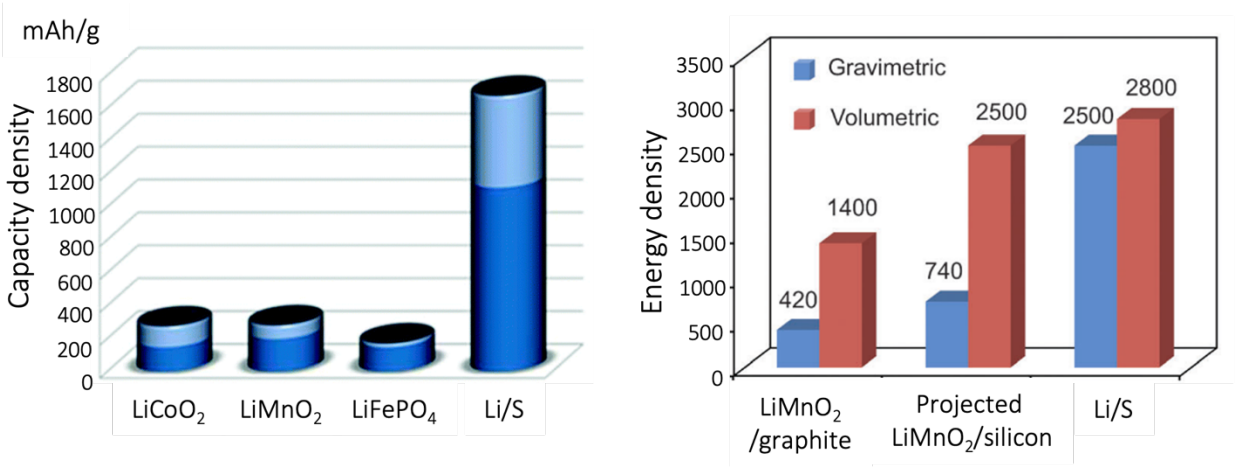

Figure 1-2. Comparisons of capacity and energy densities between Li-S batteries and Li-ion batteries. The units of energy density are Wh/kg for gravimetric energy density and Wh/L for volumetric energy density.[8,9]

1.2.1 Operating Principles of Li-S Batteries

Typically, Li-S Batteries consist of sulfur cathode, lithium metal anode, organic electrolyte, and separator (as shown in **Figure 1-3**). The reversible Li-S rection undergoes a 16-electron conversion process (**Equation 1-3**). Due to the difference (~2.2 V) of electrochemical potential between anode and cathode, the electrons (e^-) will be driven from the anode side to the cathode side during the discharge process. Lithium anode will be oxidized into Li^+ and lose electrons (**Equation 1-4**). The calculated specific discharge capacity of anode based on the weight of Li metal is 3861 mAh/g. Meanwhile, the cathode side will be reduced from elemental S_8 to Li_2S after receiving electrons (**Equation 1-5**). The calculated specific discharge capacity of cathode based on the weight of sulfur is 1673 mAh/g.

$$16Li + S_8 \leftrightarrow 8Li_2S \quad (1-3)$$

$$Li \rightarrow Li^+ + e^- \quad (1-4)$$

$$S_8 + 16Li^+ + 16e^- \rightarrow 8Li_2S \quad (1-5)$$

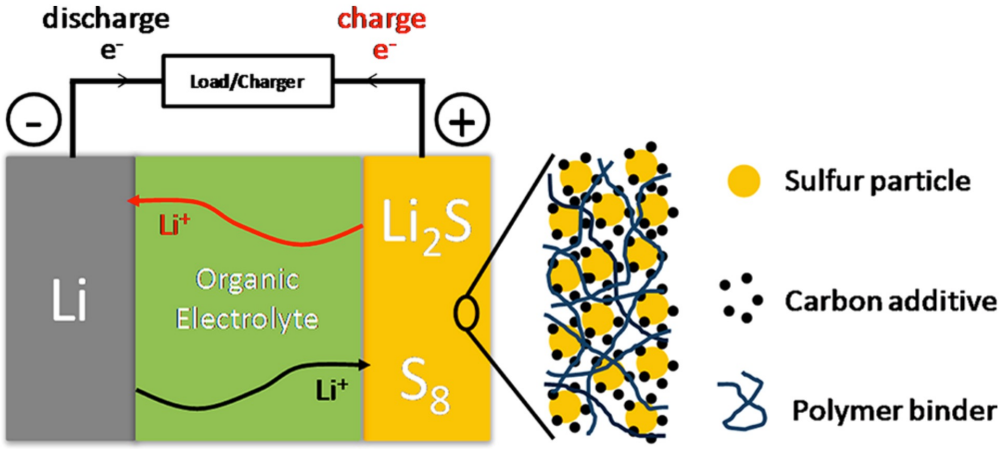

Figure 1-3. Illustration of the charge (line in red) and discharge (line in black) processes involved in Li-S batteries.[12]

Ether-based organic electrolytes, such as lithium bis(trifluoromethanesulfonyl)imide (LiTFSI) in 1,3-dioxolane (DOL) and 1,2-dimethoxyethane (DME), are wildly used to migrate Li^+ during cycling. Besides this Li^+ ion pathway in electrolyte, a stable electron pathway in electrodes is indispensable for cell cycling. Due to poor electron conductivity of sulfur, conductive additives, such as carbon black, are added in cathode. A polymeric binder is used to maintain the mechanical integrity of sulfur cathode.

1.2.2 Reaction Mechanism of Sulfur Cathode

During the cycling process of cathode, sulfur transforms between elemental sulfur and Li_2S *via* multi-step reaction with lithium.[13] The multi-step reactions generate lithium polysulfides (LiPSs) including Li_2S_x ($3 <= x <= 8$) gradually and then generate Li_2S_2 and final product Li_2S during discharge process. Based on the change of voltage profiles (**Figure 1-4**), this "conversion" reactions consist of two discharge plateaus at 2.37 and 2.16 V *vs*. Li/Li^+, respectively. During the first plateau, elemental S_8 is reduced into long-chain LiPSs (Li_2S_x, $4 <= x <= 8$) which releases a

specific discharge capacity of 418 mAh/g. Continuously, the long-chain LiPSs are further reduced into shorter LiPSs (Li_2S_x, 1 <= x <= 3), which releases the reminding specific discharge capacity of sulfur cathode. Due to the good solubility of the intermediates (Li_2S_x, 3 <= x <= 8) in DOL/DME electrolyte, the reaction in the first plateau demonstrates faster reaction kinetics than that in the second plateau. During the second reaction step, dissolved LiPSs are reduced into solid insoluble short-chain LiPSs, leading to a slower reaction kinetics.[14]

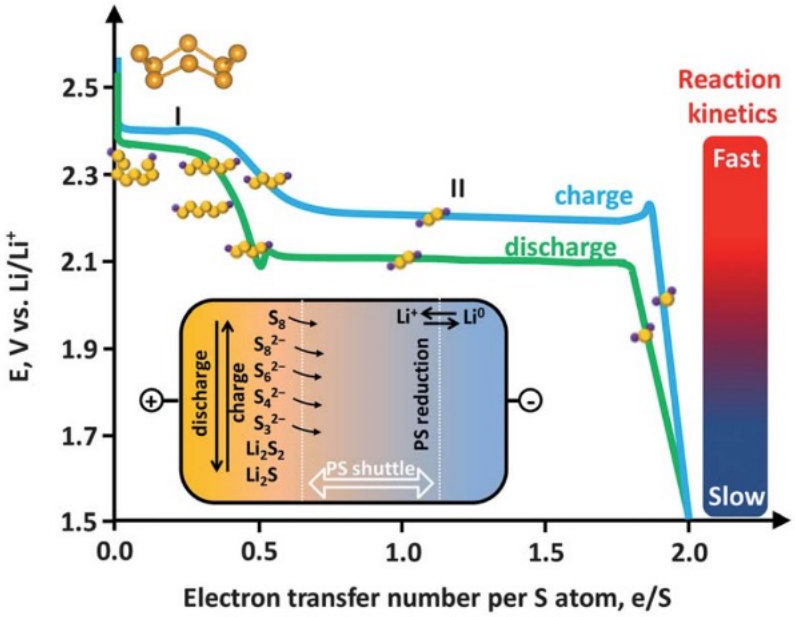

Figure 1-4. Discharge/charge voltage profile of sulfur cathode. During discharge and charge processes, Li_2S_x ($1 \leqslant x \leqslant 8$) are generated. [14]

1.3 MAJOR CHALLENGES OF SULFURE CATHODE

Despite their theoretical promise, the practical applications of Li-S batteries are significantly hindered by the technical challenges of sulfur cathode, including: (1) dissolution of LiPSs (Li_2S_x, $3 \leqslant x \leqslant 8$) in organic electrolyte; (2) volume change of active materials during

cycling; (3) insulating nature of sulfur and sulfides, *etc*.[15–17] These challenges become more severe when fabricating sulfur cathode with high sulfur loading (> 4 mg/cm^2).

1.3.1 Volume Change During Cycling

During the discharge process, elemental sulfur is reduced into Li_2S. The significant change in density of active materials from 2.07 g/cm^3 (elemental sulfur) to 1.66 g/cm^3 (Li_2S) leads to the volume expansion (~80%) in cathode during discharge process.[18,19] Once the binder is not tough enough to withstand the expansion stress, the mechanical integration of the cathode will be damaged, leading to the formation of cracks. Although the expanded volume could recover during the charge process, cracks can't be recovered once formed. Such repeated change in volume of active materials leads to the pulverization of cathode, as well as the detachment of sulfur cathode from Al conductive current collector.[20] As shown in **Figure 1-5**, Chen et *al*.[18] demonstrated the cracks formed in sulfur cathode *via* scanning electron microscopy (SEM). The direct influence of cracks is that the conductive pathway of electron will be broken immediately, causing the decay of capacity by forming "dead" sulfur which will not conduct half-cell reaction in the following cycles. Once the cracks start to form, the mechanical properties of the cathode will keep decreasing, leading to more severe cracks in the following cycles. Meanwhile, the accessibility of electrolyte will become easier in the cathode, consequently, increasing the dissolution of LiPSs into the bulk electrolyte.

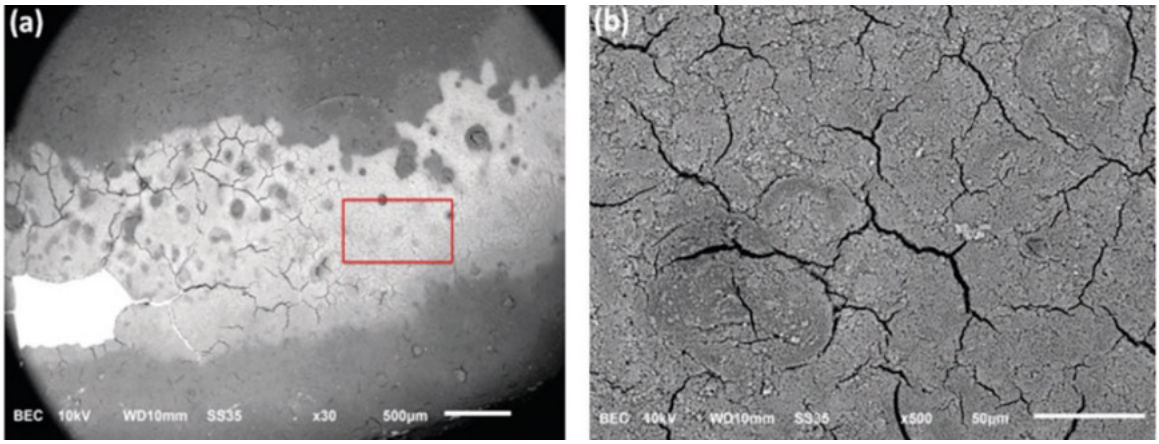

Figure 1-5. SEM images of sulfur cathodes: (a) surface of sulfur cathode; (b) a close view of the red rectangle in (a).[18]

1.3.2 Dissolution of LiPSs in Electrolyte

With the accumulation of LiPSs during cycling, soluble LiPSs (Li_2S_x, 3<= x <= 8) will diffuse out from cathode to bulk organic electrolyte. This diffusion of LiPSs causes the loss of active sulfur, leading to capacity decay immediately. Even worse, once reaching the anode side, soluble LiPSs will react with lithium metal to produce lower order LiPSs, which may diffuse back to cathode side again (**Figure 1-6**). This internal short-circuit process based on LiPSs is the "LiPSs shuttle effect" problem, leading to a decrease in coulombic efficiency. Besides the direct capacity decay of cathode side, the anode side is also sulfuring from the side reactions which consume electrolyte and lithium metal. Meanwhile, the produced insoluble LiPSs will deposit on the anode surface, which further slows down the battery reaction kinetics due to its poor electrical conductivity.

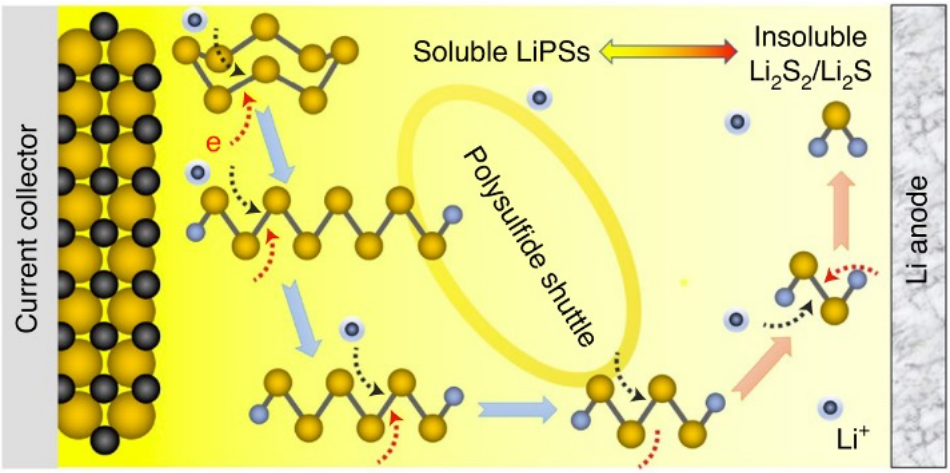

Figure 1-6. Illustration of the sulfur reduction reaction process and shuttle effect in Li-S batteries involving the evolution of LiPSs.[21]

1.3.3 Insulating Nature of Sulfur and Li_2S

Both elemental sulfur and Li_2S are insulating for Li^+ and electrons.[20] For example, the electrical conductivity of sulfur is around 5×10^{-30} S/cm, which is manifested at the reduced reaction kinetics in the sulfur cathode.[22] In the second discharge plateau (**Figure 1-4**), the reduction of LiPSs involves a solid-solid reaction process: $Li_2S_2 + 2Li^+ + 2e^- \rightarrow 2Li_2S$. It's quite difficult for sulfur cathode to achieve the theoretical capacity due to the sluggish reaction kinetics.[23] Moon *et al*.[24] reported that there is still unreacted sulfur even after 50 cycles, resulting in the decrease of discharge specific capacity and energy density.

1.3.4 Sulfur Cathode with High Sulfur Loading

A higher sulfur loading is desired for practical applications.[25] However, all the discussed challenges of sulfur cathode will become more severe with the increase of sulfur loading. First, a thicker sulfur cathode will slow down the diffusion of electron and ions due to polarization, leading

to the increase of internal resistance. A decreased V_{dis} and an increased V_{ch} are expected to be observed. Second, high sulfur loading will increase the accumulation of LiPSs near cathode, leading to more significant LiPSs dissolution and shuttle effect problem. To balance the cathode half-cell reaction, more Li metal will involve in the half-cell reaction in the anode side. The mentioned side reactions in the anode side will consume more electrolyte and LiPSs. A thicker cathode will make it more difficult to fabricate intact cathode due to the increased tension stress during fabricating cathode film and packing cell. The accumulated stress due to volume change during cell cycling brings more risk to form cracks. Consequently, it's more changeling to achieve long-cycle-life sulfur cathode with higher sulfur loading.

1.4 CURRENT RESEARCH

1.4.1 Design of Sulfur Matrixes

Tremendous efforts have been devoted to improve the performance of sulfur cathode by designing the host materials for sulfur.[26] Carbonaceous materials are intensively investigated due to their high electrical conductivity, diverse structures, *etc*. Nazar and co-workers[27] reported to utilize a highly ordered carbon (CMK-3) as host material to not only physically confine sulfur inside the carbon channel with a width of 3-4 nm, but also improve the electrical conductivity of sulfur cathode. Porous carbon materials, including microporous (pore size < 2 nm),[28] mesoporous carbon (2 nm < pore size < 50 nm),[29] and microporous carbon (pore size > 50 nm) were also studied.[30] By confining sulfur inside microporous carbon, Xin and co-workers[28] synthesized small sulfur molecules $S_{2\text{-}4}$ as active material for sulfur cathode, which avoids the formation of soluble LiPSs. The resulting cathode with smaller sulfur demonstrated a high capacity retention of 96% over 200 cycles at 0.1C rate. Li and co-workers[29] reported the effects of sulfur-filling condition,

as well as the pore sizes of mesoporous carbon, on cathode performances. Besides high specific surface area, graphene possesses superior electrical conductivity.[31] The surface functional groups, including -OH, C=O, -COOH, provides graphene with active sites to anchor LiPSs.[32,33] Nazar's work demonstrated graphene oxide (GO) triggers the oxidization of LiPSs into thiosulfate, which further mediates the conversion of soluble LiPSs.[34] Different from porous structure with openings, hollow sulfur matrixes, including carbon, TiO_2 spheres are developed to entrap sulfur in the sealed structures.[19,35] The reported sulfur–TiO_2 yolk–shell nanoarchitecture demonstrated low capacity fading rate of 0.033% per cycle.[19] However, the kinetics of Li ion diffusion was slowed down due to the barrier of the sealed shell structure, leading to significant overpotential.

Besides physically trapping LiPSs and improving electrical conductivity of sulfur cathode, sulfur matrixes are also designed to entrap LiPSs *via* chemical interactions (**Figure 1-7**). Non-polar carbon materials interact with LiPSs with low binding energies 01-0.7 eV *via* van der Waals forces.[36] Heteroatom-doped sulfur matrixes confine LiPSs through the dipole-dipole interaction with a binding energy of 1.3-2.6 eV.[37–39] Taking advantaging the stronger binding energy of 2.6-3.5 eV, stoichiometric metal oxides and sulfides are widely studied as sulfur matrixes to solve the LiPSs dissolution problem, including Ti_4O_7, MnO_2.[34,40] Since polysulfide anions are Lewis bases, host materials with Lewis acid characteristics are used to interact with sulfur through metal-sulfur bonding.[41,42]

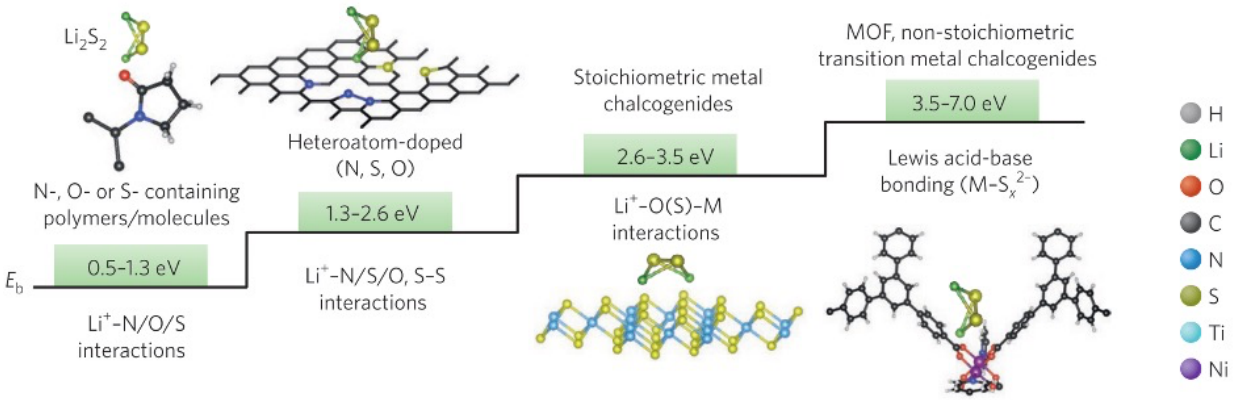

Figure 1-7. Binding energies for chemical interactions between LiPSs with sulfur matrixes based on computations. Li_2S_2 is used as representative LiPSs.[43]

1.4.2 Functional Binders

As the indispensable component in cathode, a binder not only glues active materials and conductive carbon together, but also ensures the integration of sulfur cathode with well conductive pathway for both electron and Li ion.[44–47] Design of functional binders is crucial to mitigate LiPSs dissolution, improve electrical/Li^+ conductivity,[48] and fabricate high-loading cathodes,[49] *etc*. Despite its successful application in Li-ion batteries, the effect of polyvinylidene fluoride (PVDF) on mitigating LiPSs diffusion is unsatisfactory. Compared with PVDF, poly(ethylene oxide) (PEO) owns higher Li ion and electrical conductivity.[50] Especially, the partial dissolution and welling nature of PEO in organic electrolyte could improve the wettability of sulfur surface, consequently reducing the Li ion transfer resistance.[51–53] Functional binders with polar groups are widely studied to confine LiPSs through dipole-dipole interaction. Chen and co-workers fabricated amino functional group (AFG) binder by polymerizing hexamethylene diisocyanate (HDI) with polyethylenimine (PEI) polymer.[54] Compared with linear PVDF, this AFG binder was featured with abundant polar amine groups and hyperbranched networks structures, resulting in capacity retention of 91.3% over 600 cycles at 2C rate and high sulfur loading. Li Gao's group investigated

the effect of conductive binder poly(9, 9-dioctylfluorene-co-fluorenone-co-methylbenzoic ester) (PFM) on sulfur cathode.[55] Due to the improved conductivity and strong interaction with LiPSs, PFM accelerated the precipitation of solid Li_2S during discharge process, which reduces the shuttle effect greatly. Zhang *et al*. reported a multifunctional binder by crosslinking PEO with tannic acid, which not only retard shuttle effect but also improve sulfur loading to 5 mg/cm^2.[53] Similarly, Liu and co-workers reported a biopolymer binder with robust crosslinked structure to enable sulfur cathode with remarkably high sulfur loading of 19.8 mg/cm^2, which is also low-cost and environmentally friendly.[56]

1.4.3 Design of Separator

Although LiPSs have dissolved in electrolyte, a functional separator still could mitigate the shuttle effect by preventing the diffusion of LiPSs through the separator. A bifunctional separator modified by black-phosphorus nanoflakes was prepared by Sun and co-workers to entrapment LiPSs *via* strong binding energy and re-activation of the trapped LiPS due to its high electron and Li-ion conductivities.[57] Bai *et al*. developed a metal-organic framework (MOF)-based battery separator which selectively sieved Li ion and suppressed the diffusion of LiPS.[58] Hwang et al. designed a dual-functional graphene–polypropylene–Al_2O_3 separator with LiPSs absorbability and electrocatalytic effect.[59] A cathode with greatly enhanced reaction kinetics of LiPSs redox reactions was achieved. Although functioned separators help inhibit the diffusion of LiPS to the anode side, considerable amount of LiPSs have already dissolved into the electrolyte, leading capacity decay.[59–61]

1.4.4 Cathode Additives and Coating Treatment

A functional coating layer on sulfur matrix or separator could offer a LiPSs diffusion barrier, which suppresses the dissolution of soluble LiPSs to a certain degree. For example, PEO coating layer on carbon matrix was proven to improve cell performances by providing a chemical gradient of LiPSs.[27] The increased cathode performances were attributed to the improved solvent system by partially dissolve PEO in electrolyte.[51] Conductive polyaniline layers were used to coat the sulfur, forming the core−shell and yolk−shell structures.[62] Compared with core-shell structure, the yolk-shell coated layer-sulfur exhibits more stable cycling performance due to the existence of excess volume to mitigate volume expansion stress of sulfur species. Meini *et al*. repotted the addition of redox mediators in electrolyte to reduce the activation voltage of Li_2S, consequently improve the utilization of active materials.[63] Hydrophilic MgO nanoparticles was used as additive to entrap LiPSs through chemical interactions.[64]

Although various strategies may improve the performances of sulfur cathode to a certain extent, few of them are promising to solve all the problems of sulfur cathode simultaneously. For instance, despite the improved LiPSs trapping ability, sulfur cathodes with nanostructured carbon are still too fragile to fabricate with high sulfur loading. The high porosity of nanostructured materials usually leads to relative low packing density. Given the fact that most sulfur matrixes are unsealed, the dissolution and accumulation of LiPSs are inevitable. Therefore, a novel design to solve multi-problems is highly desired. Among all the criteria for commercially practical sulfur cathode, high sulfur loading is prerequisite. To compete with current Li-ion batteries, an areal density higher than 4 mg/cm^2 is desired for sulfur cathode. Afterwards, a high initial specific discharge capacity and good cycling stability are needed.

1.5 THESIS OBJECTIVES AND OVERVIEW OF CHAPTERS

To solve these problems, here I propose a molecular engineering strategy to develop multi-functional PENDI-based binder system. By utilizing molecular interaction principles, the resulting binders are effective to confine LiPSs and mitigate volume expansion cracks efficiently, consequently achieving high-loading, long-cycle-life sulfur cathode for Li-S batteries. As shown in **Figure 1-8**, PENDI is designed based on redox active naphthalene diimide (NDI). First, redox active NDI mediates the transformation of long-chain soluble LiPSs into insoluble short-chain LiPSs and polythionate, which decreases LiPSs diffusion significantly. Second, carbonyl groups in NDI and the formed NDI^{2-} dianions from the reaction between NDI and LiPSs, further confine LiPSs *via* dipole-dipole and ion-dipole interactions. Besides, a supramolecular network structure is formed by crosslinking PENDI with triPy through the reversible pi-pi interactions between NDI group and Py group, which mechanically stabilizes sulfur cathode. The reversible pi-pi interactions not only help dissipate tension stress to reduce the formation of cracks, but also potentially self-heal the cracks that have already formed.

To demonstrate the design concepts stepwise, this thesis consists of the following chapters:

Chapter 1 introduces the background of batteries and Li-S batteries. The challenges faced by sulfur cathode, and the corresponding current research to solve the challenges are summarized and discussed. Then the design concept of multi-functional binder system based on polymer PENDI is proposed for high-loading, long-cycle-life sulfur cathode.

Chapter 2 investigates the redox properties of PENDI which confines LiPSs through chemical interactions and redox mediation. The detailed redox mediation mechanism based on NDI and its strong interactions with LiPSs are systematically studied. The resulting PENDI exhibits superior LiPSs confining effect compared with conventional PVDF binder.

Chapter 3 investigates the design of crosslinked supramolecular network structure based on PENDI and triPy crosslinker. First, the reversible pi-pi interaction and different binding modes between NDI and Py are studied. Second, self-healing polymer system based on polymer PENDI and triPy crosslinker are designed to mitigate cracks. Then different strategies to modulate the self-healing and mechanical properties of the resulting network structure are proposed to extend its application potentials.

Building upon Chapter 2 and Chapter 3, Chapter 4 integrates the molecular designs into the application of PENDI-based binder system in sulfur cathode. A series of PENDI-based binder systems are fabricated and optimized to achieve high-sulfur-loading, long-cycle-life sulfur cathodes by improving the mechanical properties, including toughness, Young's modulus, *etc*.

Chapter 5 summarizes the results and conclusions from this work. Outlooks for next step are also made to improve the cathode performances further.

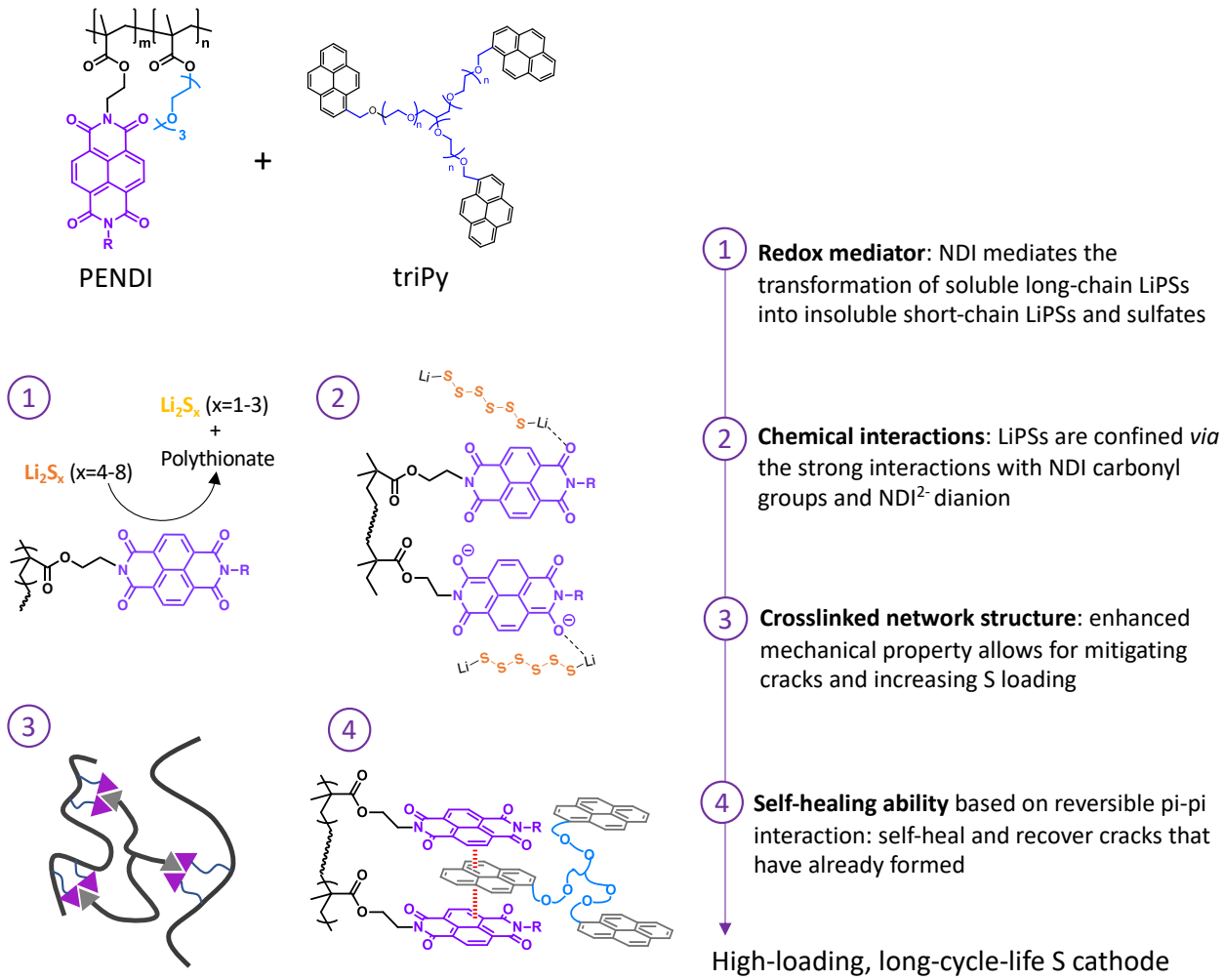

Figure 1-8. Design concepts of the multi-functional binder based on PENDI for high-loading, long-cycle-life sulfur cathode in Li-S batteries.

CHAPTER 2: REDOX ACTIVE BINDER FOR LITHIUM-SULFUR BATTERIES TO CONFINE LITHIUM POLYSULFIDES THROUGH REDOX MEDIATION AND CHEMICAL INTERACTIONS

2.1 INTRODUCTION

2.1.1 Motivation

Low-cost energy storage devices with high energy density are highly desired to accelerate the developments of electric vehicles, portable electronic devices, and utilization of clean energy, *etc.*[22] Li-S battery is receiving increased attention due to its high theoretical gravimetric energy density of ~2510 Wh/kg, which is up to five-folds compared to the conventional Li-ion batteries.[10] The sulfur cathode delivers theoretical discharge capacity as high as 1675 mAh/g. Nevertheless, the development of sulfur cathode is still hindered by several challenges, especially the dissolution of LiPSs (Li_2S_x, $3 <= x <= 8$).[13] During cycling process, sulfur transforms between elemental sulfur and Li_2S *via* multi-step reactions with lithium.[13] However, LiPSs (Li_2S_x, x = 3-8) are soluble in organic bulk electrolyte, leading to loss of active sulfur, consequently capacity decay.[22] Besides, due to the higher density of sulfur than that of Li_2S, the fully discharge reaction causes significant volume expansion (~80%), which potentially cracks cathode and decays discharge capacity.[18]

Numerous efforts have been devoted to prevent the dissolution of LiPSs from sulfur cathode.[13,43] Nanostructured carbons such as mesoporous carbon,[65,66] graphene/graphene oxide (GO) sheets,[67] and carbon nanotubes[59] are well developed as host matrixes for sulfur to confine LiPSs and improve electronical conductivity.[68] Given the fact that most nanostructured carbons are made of porous channels with openings however, soluble LiPSs will eventually dissolve from

the physical confinements. The second strategy to prevent the dissolution is to anchor LiPSs *via* chemical interactions by using host materials with functional group modified surfaces or binders with the functional groups.[69,70] For instance, various binders with heteroatom-containing polar groups have been proposed to confine LiPSs *via* dipole-dipole chemical interactions.[49,71,72]

Although the physical spatial confinement and chemical adsorption could mitigate the diffusion of soluble LiPSs, the accumulation of LiPSs can occurs in the cathode side. To address the LiPSs accumulation fundamentally, more and more attention is paid to the developments of redox active materials.[48,63,73] Different from passively lowering the diffusion of LiPSs *via* physical confinement and chemical interaction, redox active materials provide a strategy which actively reduce the accumulation of LiPSs directly.[34] Due to their electrochemical activities under the operation voltage of S cathode, redox active materials facilitate the electrochemical reaction kinetics of S cathode.[74–76] For example, metal oxides with redox potentials in a target window (2.4 V - 3.05 V vs. Li/Li^+) were reported by Nazar's group to trigger the formation of functional thiosulfate groups.[77] As shown in **Figure 2-1**, thiosulfate groups then mediate the conversation of long-chain LiPSs into insoluble polythionate and Li_2S_2/Li_2S by catenation reaction. This redox mediation effect through thiosulfate-polythionate conversion decreases the accumulation of soluble LiPSs significantly to achieve Li-S cells with very low LiPSs solubility and long life (up to 2,000 cycles).[34] However, most reports on LiPSs redox mediators are mainly limited to inorganic materials as host materials or additives, including manganese dioxide (MnO_2), cobalt diselenide ($CoSe_2$) nanodots, vanadium dioxide (VO_2), and titanium dioxide (TiO_2) nanoparticles.[77–80]

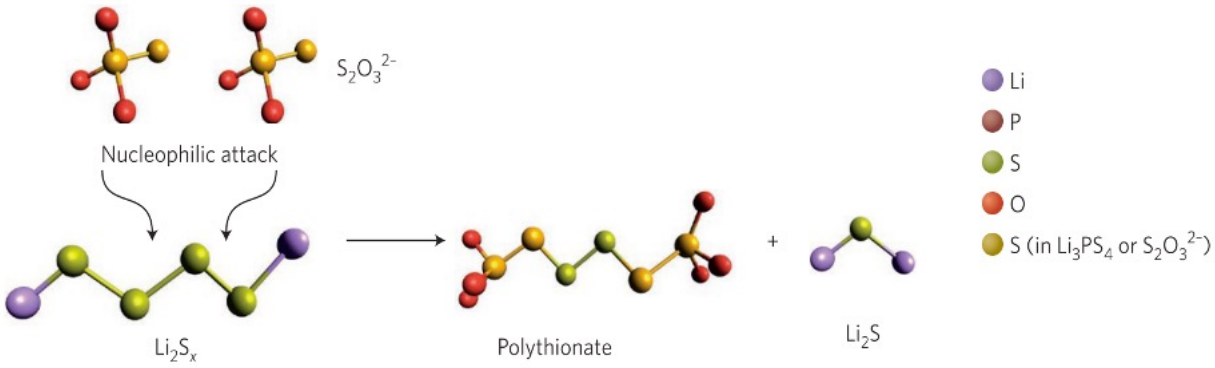

Figure 2-1. The catenation reaction mechanism to confine LiPSs by thiosulfate-polythionate conversion.[43]

2.1.2 Rational and Overview

Herein, I report a novel design of redox active binder PENDI (a side-chain co-methacrylate with a side-chain group naphthalenetetracarboxylic diimide (NDI)) to achieve sulfur cathode with high-capacity retention. As shown in **Figure 2-2**, the resulting PENDI binder improves sulfur cathode performance *via* the redox mediation and strong chemical interactions of NDI on LiPSs: First, NDI transforms soluble long-chain LiPSs (Li_2S_x, x=4-8) to short-chain LiPSs and mediates the conversion of LiPSs to thiosulfate and polythionate, which prevents the dissolution of LiPSs due to the low solubility of reduction products Li_2S_2 and Li_2S, and oxidation products thiosulfate and polythionate. Second, the NDI groups containing multiples of polar carbonyl groups which entrap LiPSs *via* strong dipole-dipole interactions. Besides, stable NDI^{2-} dianion is formed from NDI, which has been reported to interact with Li^+ strongly.[81] Consequently, soluble LiPSs could be confined further by the dipole-dipole and ion-dipole interactions.

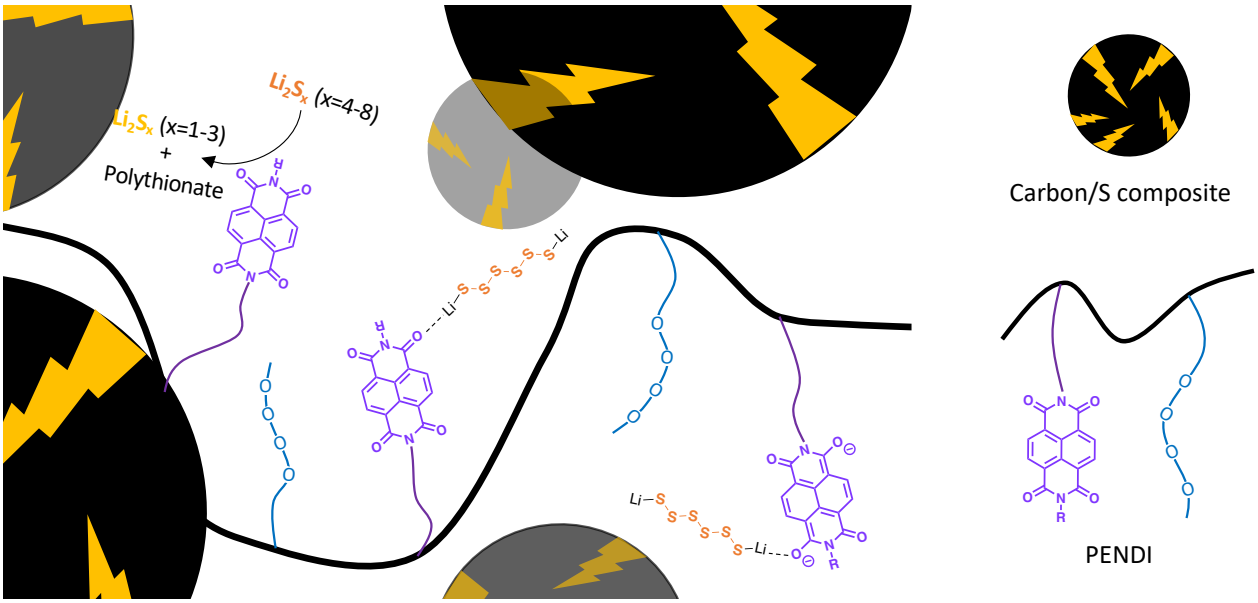

Figure 2-2. Schematic illustration of the design and multiple functions of NDI in PENDI binder, including mediated oxidation of LiPSs to thiosulfate-polythionate, and interactions of LiPSs with NDI carbonyl groups and NDI^{2-} dianion *via* dipole-dipole and ion-dipole interactions.

2.2 EXPERIMENTAL SECTION

2.2.1 Materials

Solvents, including tetrahydrofuran (THF, 99.9%, Aldrich), ethanol (99%, Aldrich), dichloromethane (DCM, 99.8%, Aldrich), for chemical synthesis were purified by distillation. Mesoporous carbon MJ430 (Porous Carbon CNovel™ ; Toyo Tanso USA, Inc.) was washed with 2 M HCl in ethanol for purification. Tetraethylene glycol dimethyl ether (G4, ≥99%, Aldrich), anhydrous 1,3-dioxolane (DOL, 99.8%, Aldrich), anhydrous 1,2-dimethoxythane (DME, 99.8%, Aldrich) were dried with 4Å molecular sieves and then stored in an argon-filled glovebox (Vacuum Technology Inc, <0.01ppm H_2O and O_2) before use. Lithium bis-(trifluoromethanesulfonyl)imide (LiTFSI) and $LiNO_3$ were purchased from 3M and dried at 120°C under argon, then stored/used

in an argon-filled glovebox. Lithium chips (99.9%, 15.6mm diameter, 0.45mm thickness) and other cases used for coin cell assembly (including o-ring, spring, spacer, caps) were purchased from MTI Corp and stored/used in an argon atmosphere glove box. All other chemicals and reagents were purchased from Aldrich.

2.2.2 Characterization

The ^{1}H and ^{13}C NMR spectra were recorded on a Bruker AV500 spectrometer using $CDCl_3$ or d_6-DMSO as a solvent. Mass spectrometry (MS) was performed on a Bruker APEX III 47e Fourier transform mass spectrometer. Thermogravimetric (TGA) analyses were conducted on a Shimadzu TGA-50 thermogravimetric analyzer under nitrogen at a heating rate of 10 °C min^{-1}. UV-vis spectra were recorded on a Varian Cary 5000 UV-Vis-NIR spectrophotometer. All samples used for UV-vis tests were prepared with dichloromethane as the solvent. Differential scanning calorimetry (DSC) measurements were performed in a heat–cool–heat cycle (–40 to 220 °C, 10 °C min^{-1}; 220 to –40 °C, –10 °C min^{-1}; –40 to 220 °C, 10 °C min^{-1}). An OlymScope was used for optical imaging tests. X-ray photoelectron spectroscopy (XPS) experiments were conducted using Kratos AXIS Ultra DLD. A Model 600 electrochemical workstation from CH Instruments, Inc. was used for Cyclic Voltammetry (CV) experiments.

2.2.3 Synthesis of N-hexyl-1,4,5,8-naphthalenetetracarboxy-1,8-monoanhydride-4,5-monoimide (**2**) [1]

As shown in **Scheme 2-1**, to a stirred suspension of 1 (5.72 g, 20.0 mmol) in DI water (300 mL) was dropwise added n-hexylamine (12.1 g, 120 mmol) through an addition funnel at 0 °C

[1] The synthesis of PENDI was conducted under the cooperation with Francis Lin.

during which the solution turned clear. The reaction mixture was stirred overnight and slowly allowed to warm to room temperature, then refluxed for 2 hours and again cooled to 0 °C followed by the addition of 10% $HCl_{(aq)}$ (100 mL). The precipitate was collected by filtration and washed with water and ice-cold methanol, which was then refluxed in a mixture of $HCl_{(conc.)}$ (40 mL) and THF (20 mL). The suspension was again filtered, and the solid collected was washed consecutively with water, methanol, and ice-cold acetone to afford 2 as a pale-yellow solid (6.61 g, 94%). ^{1}H NMR (d_6-DMSO, 500 MHz) δ 8.67 (m, 4H), 4.03 (t, J = 7.5 Hz, 2H), 1.65 (m, 2H), 1.29–1.36 (m, 6H), 0.87 (t, J = 7.5 Hz, 3H); ^{13}C NMR (d_6-DMSO, 125 MHz) δ 162.31, 158.66, 131.82, 130.39, 128.43, 127.08, 126.07, 123.67, 39.02, 30.93, 27.25, 26.15, 21.95, 13.89; HRMS (m/z, ESI) calculated for $C_{20}H_{17}NO_5$ 351.1107, found 351.1116.

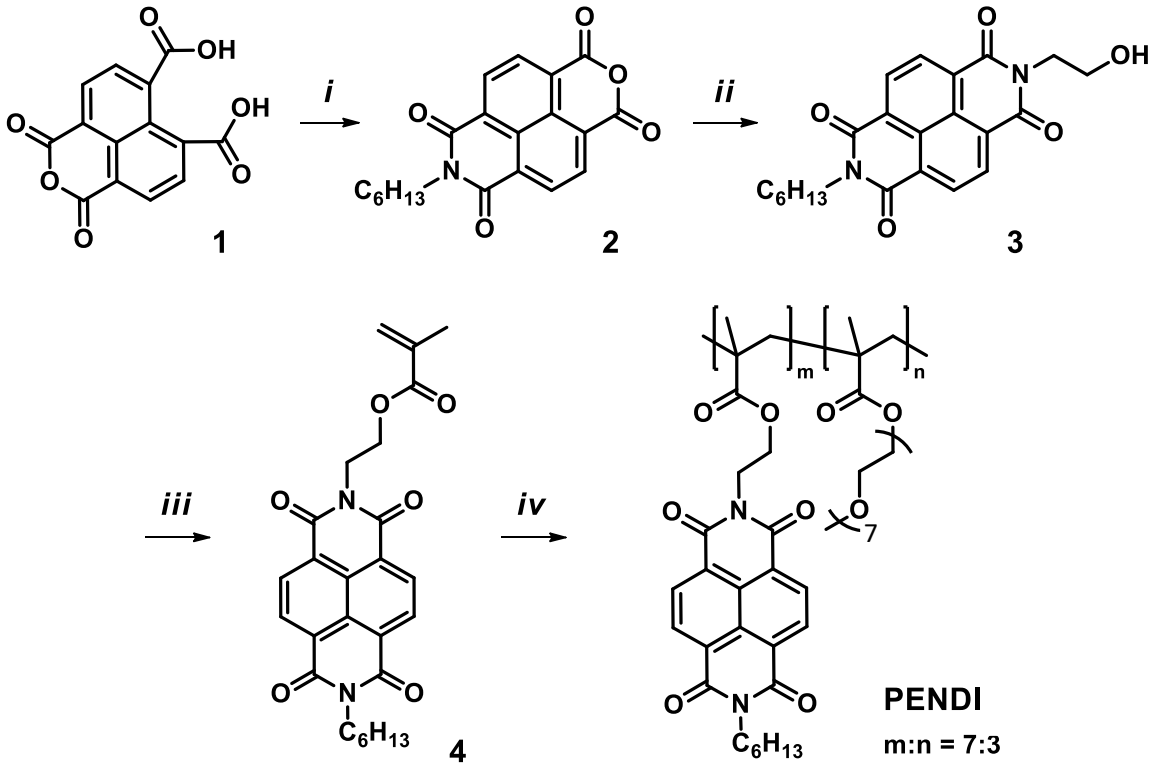

Scheme 2-1. Synthetic routes of PENDI. Reagents and conditions: (i) a) 1-Hexylamine, H_2O, 0 °C, then refluxed; b) 10% $HCl_{(aq)}$, 0 °C; c) THF/$HCl_{(conc.)}$, (v/v=1:2). (ii) Ethanolamine, EtOH, 80 °C.

(iii) Methacryloyl chloride, Et_3N, DCM/THF (v/v=1:1), 40 °C. (iv) Oligomeric ethylene oxide methyl ether methacrylate, AIBN, THF, 70 °C. All chemical reactions were conducted under the protection of argon.

2.2.4 Synthesis of N-hexyl-N′-(2-hydroxyethyl)-1,4,5,8-naphthalenetetracarboxydiimide (**3**)

To a stirred suspension of **2** (5.27 g, 15.0 mmol) in ethanol (150 mL) was dropwise added ethanolamine (1.10 g, 18 mmol) through an addition funnel at room temperature. The reaction mixture was then refluxed and stirred overnight. The precipitate was collected by filtration and washed with ice-cold methanol to afford 3 as a pale-yellow solid (5.44 g, 92%). ^{1}H NMR (d_6-DMSO, 500 MHz) δ 8.53 (m, 4H), 4.83 (t, J = 5 Hz, 2H), 4.13 (t, J = 5 Hz, 2H), 4.00 (t, J = 7.5 Hz, 2H), 3.64 (m, 2H), 1.63 (m, 2H), 1.30–1.36 (m, 6H), 0.87 (t, J = 7.5 Hz, 3H); ^{13}C NMR (d_6-DMSO, 125 MHz) δ 162.28, 162.15, 130.11, 130.08, 125.95, 125.84, 125.74, 57.56, 42.06, 30.68, 27.10, 25.93, 21.69, 13.58; HRMS (m/z, ESI, $[M + H]^+$) calculated for $C_{22}H_{23}N_2O_5$ 395.1607, found 395.1618.

2.2.5 Synthesis of N-hexyl-N′-(2-[methacryloyl]ethyl)-1,4,5,8-naphthalene tetracarboxydiimide (**4**)

To a stirring suspension of **3** (5.52 g, 14.0 mmol) in a mixed solvent of THF (70 mL) and DCM (70 mL), with trace amounts of 4-methoxyphenol, was added distilled Et_3N (1.56 g, 15.4 mmol) and then cooled to 0 °C, after which freshly distilled methacryloyl chloride (1.61 g, 15.4 mmol) was added dropwise. The reaction mixture was gently heated to 40 °C and stirred overnight. After cooling to room temperature, the mixture was poured into cold methanol. The precipitate was collected by filtration and then washed with ice-cold methanol to afford 4 as a pale-yellow

solid (5.56 g, 85%). ^{1}H NMR ($CDCl_3$, 500 MHz) δ 8.74 (m, 4H), 6.02 (s, 1H), 5.51 (s, 1H), 4.57 (t, J = 5 Hz, 2H), 4.50 (t, J = 5 Hz, 2H), 4.18 (t, J = 6.5 Hz, 2H), 1.84 (s, 3H), 1.74 (m, 2H), 1.33–1.44 (m, 6H), 0.89 (t, J = 0.89, 3H); ^{13}C NMR ($CDCl_3$, 125 MHz) δ 167.18, 162.84, 162.70, 135.87, 130.91, 126.81, 126.29, 125.96, 61.75, 40.97, 39.47, 31.45, 27.98, 26.69, 22.50, 18.19, 14.00; HRMS (m/z, ESI, $[M + H]^+$) calculated for $C_{26}H_{27}N_2O_6$ 463.1869, found 463.1876.

2.2.6 Synthesis of Poly (N-ethyl-N′-hexyl-1,4,5,8-naphthalenetetracarboxydiimidyl methacrylate-co-oligomeric ethylene oxide methyl ether methacrylate) (PENDI)

To a mixture of **4** (693 mg, 1.5 mmol), oligomeric ethylene oxide methyl ether methacrylate (228 mg, 0.6 mmol) and AIBN (4 mg, 1.2 mol%) in a sealed flask was added THF (3 mL). The reaction mixture was degassed through 3 freeze–pump–thaw cycles and heated at 70 °C for one day with vigorous stirring. After cooling to room temperature, the mixture was poured into cold methanol. The precipitate was collected by filtration and washed with methanol to afford PENDI-C_6 as a white solid (730 mg, 93%). ^{1}H NMR ($CDCl_3$, 500 MHz) δ 8.39 (b, 28H), 4.02 (b, 48H), 3.52 (b, 30H), 3.31 (b, 9H), 1.60 (b, 34H), 1.30 (b, 72H), 0.88 (b, 21H); GPC (M_n = 19.2 kDa, PDI = 2.67).

2.2.7 Fabrication of Sulfur Cathode[2]

Mesoporous carbon MJ430 was used as the host material for sulfur to fabricate melt-infiltrated S/C composite (**Table 2-1**, **Figure 2-3a**). By mixing S/C composite, carbon nanotube as conductive additive, PENDI or PVDF as binder (70:5:25 by weight) in N-methyl-2-pyrrolidone, a cathode slurry was made, followed by blade-coating on the surface of C-coated Al foil (18 μm

[2] The fabrication of sulfur cathode and assembly of Li-S coin cell were conducted under the cooperation with Dion Hubble and Yun (April) Li.

in thickness, MTI corporation). After heat treatment in vacuum at 50 °C overnight, the resulting composite cathode film was punched into discs. After weighting and calculating the amount of sulfur, the sulfur cathodes were used for cell assembly.

2.2.8 Assembly of Li-S Coin Cell

The test cells were assembled in 2032 coin-type structures (**Figure 2-3b**). All operations were conducted inside an argon filled glove box. First, the sulfur cathode in the center of a metal cap (large cap, diameter = 20 mm) was placed, followed by placing a Celgard 2500 separator on top of it. Then 7 mL of electrolyte with (1 M LiTFSI) and 2 wt% $LiNO_3$ in DOL/DME (v/v =1:1)) was added for 1 mg of sulfur, followed by placing a hollow circular plastic o-ring. Then a piece of Li metal chip, a spring spacer and a smaller metal cap were added in sequence. The cell was sealed by mechanical press. The cell performances were evaluated at room temperature in a voltage window of 1.7-3.1 V vs. Li/Li^+ at various C rates by using an Arbin battery tester (1C = 1675 mAh/g).

Table 2-1. The components and corresponding weight ratios of cathode slurry for fabricating cathode film.

Components	Weight ratio	Description
S/C composite	70 wt.%	MJ430/S (50 wt.%)
Binder	25 wt.%	PENDI/PVDF
Conductive additive	5 wt.%	CNT
Electrolyte	7 ul/1 mg S	DOL/DME (v/v = 1:1), 1M LiTFSI, 1 wt.% $LiNO_3$

Separator	-	Celgard 2500

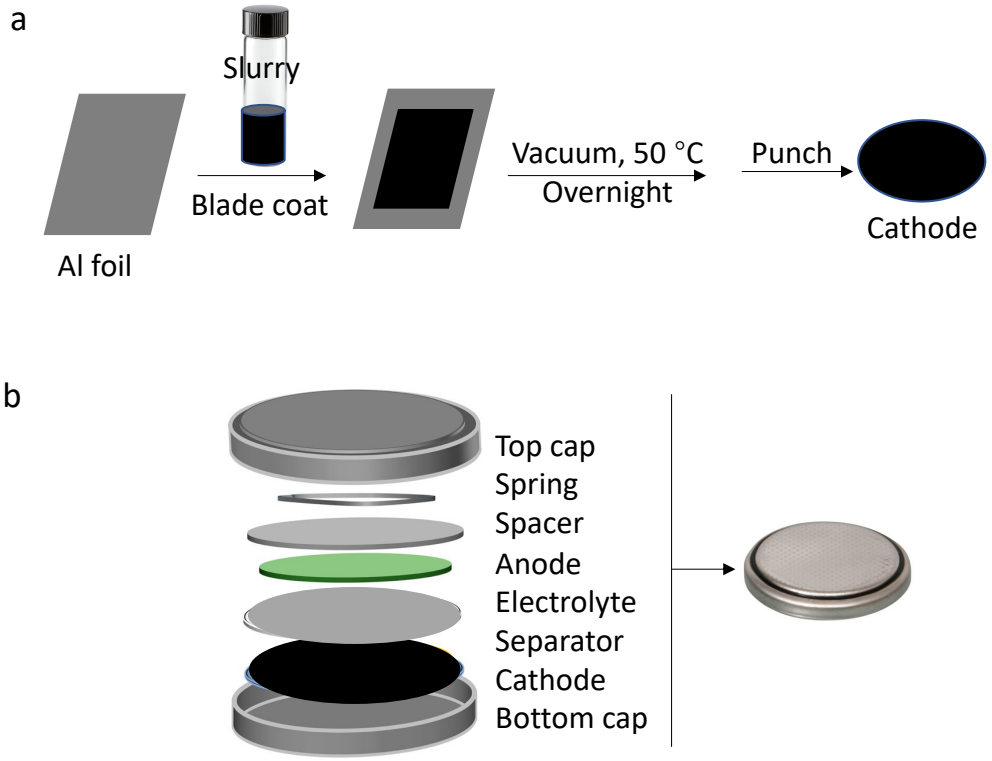

Figure 2-3. (a) Fabrication of sulfur cathode by blade-coating of cathode slurry, followed by heat treatment; (b) Components used for assembling coin cell.

2.3 RESULTS AND DISCUSSION

2.3.1 Design and Synthesis of PENDI

NDI derivatives are well studied as n-type semiconductors in the organic electronics field.[82] Conventionally, NDI derivatives are designed as a small molecules[83] or a rigid semiconductive polymers with NDI in the polymer backbone[84]. As the indispensable component in cathode, however, binders are desired to be flexible polymer to entangle and bind cathode components

together and ensure the integrity of cathode. Here, we design the NDI-based binder as a copolymer with NDI and oligomeric ethylene oxide (OEO) as side-chain groups. The existence of OEO group not only increases the flexibility of the resulting polymer (PENDI, Mn =19.2 kDa, PDI = 2.67, shown in **Figure 2-4a**), but also improves its electrolyte affinity.[52] PENDI also demonstrates good thermal stability (**Figure 2-4b**) with a decomposition temperature of 323 °C.

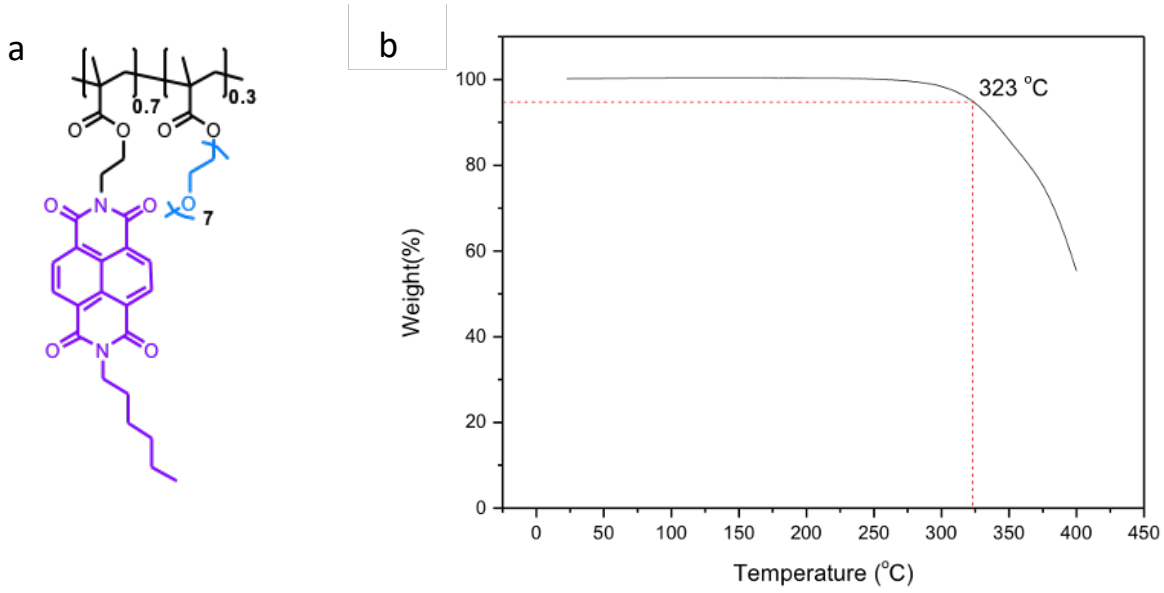

Figure 2-4. (a) Molecular structure of PENDI; (b) Thermogravimetric analysis of PENDI with a nitrogen flow of 50 mL/min and a heat rate of 10 °C/min.

2.3.2 Interaction between PENDI and LiPSs

First, we conducted direct visual experiment to qualitatively investigate the interaction between PENDI and LiPSs. PVDF (Mw=600 kDa) was used for comparison. As shown in **Figure 2-5a**, 10 mg each of polymer powders were placed in empty vials, followed by addition of reddish-brown solution of Li_2S_8 (~10mM) in Li(G4)TFSI (lithium bis(trifluoromethylsulfonyl)imide (LiTFSI) in tetraglyme (G4)). Li_2S_8 was used as representative LiPSs to simulate the LiPSs environment at the initial discharge state. Li(G4)TFSI was use as solvent due to its excellent ability

to dissolve LiPSs,[27] and low volatility which helps maintain the constant volume of solvent during the experiment.[85] The Li_2S_8 solutions were absorbed by the polymer powders immediately. PVDF powder turned into reddish-brown which is the same color as Li_2S_8 solution. On the contrary, PENDI powder turned immediately into dark black from original white color, which demonstrates the existence of strong molecular interactions. Then additional solvent was added into the vials and mixed by stirring for 1 hour to qualitatively estimate strength of the interactions. Polymers with strong interactions could confine LiPSs in the polymer with limited dissolution. Resulting solutions were syringe filtered to remove the solid polymers. Polymers, insoluble LiPSs and soluble LiPSs confined by polymers were filtered out. Then the filtrates were diluted to conduct the UV-Vis spectra. The diluted solution of pristine Li_2S_8 solution in compatible concentration was used as reference for comparison. As shown in **Figure 2-5b**, the diluted filtrate from PVDF sample exhibits yellow color, similar to that of the reference. The corresponding UV-Vis absorption peak PVDF sample is slightly lower than that of the reference. The majority of soluble LiPSs were dissolved in the filtrate. Despite its polarity, PVDF shows limited interaction with LiPSs. On the other hand, filtrate from PENDI sample shows negligible absorption peak. This shows that PENDI interacts strongly with dissolved LiPSs to remove from the solution.

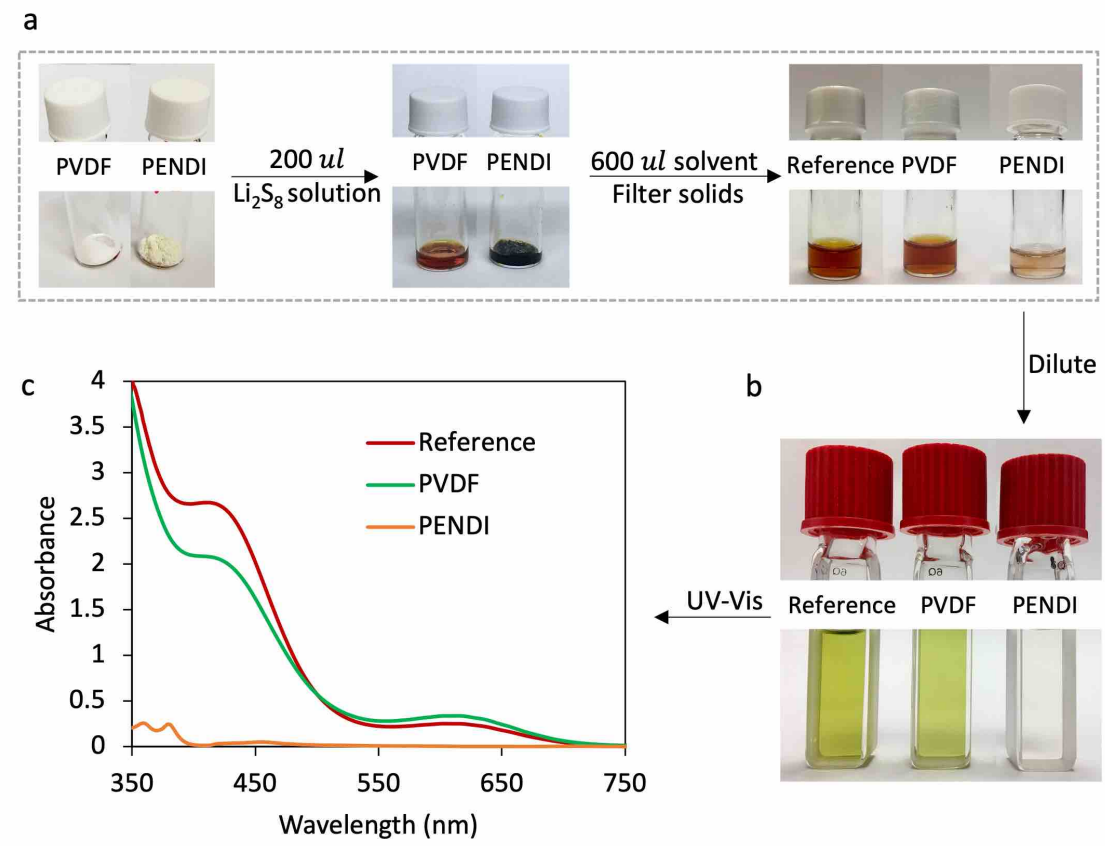

Figure 2-5. Optical images and UV-Vis spectra of experiments to measure interactions between LiPSs and PENDI. (a) Adding reddish-brown LiPSs solutions into polymers, followed by filtration; (b) The diluted filtrates; (c) Corresponding UV-Vis spectra of the diluted filtrates.

2.3.3 Interactions of NDI Derivatives with LiPSs

Computational studies based on first-principles calculations provide important insights into the interactions between LiPSs with polar groups.[43,86–88] A computational screening of functional groups grafted on polymers demonstrates that the carbonyl (C=O) group shows the highest binding energy with Li_2S among functional groups with lone pairs on oxygen, nitrogen, and halogen atoms.[86] In our design, PENDI contains NDI with abundant carbonyl groups which could help entrap LiPSs *via* chemical interactions efficiently. To investigate the strong interaction between

LiPSs and carbonyl groups of NDI in PENDI experimentally, XPS experiments were performed for the mixtures of LiPSs and PENDI.[34,77] The interactions between LiPSs and functional groups can be detected based on the peak shift of S in S2p XPS spectra.[89,90] A peak shift of S2p spectrum to higher binding energy is expected due to decreased electron density withdrawn from LiPSs by the interactions.[91]

In detail, Li_2S_4 was used as a representative LiPSs due to its proven consistency during the XPS experiments.[34,91] LiPSs, such as Li_2S_8 used above for dissolution experiments is known to produce elemental sulfur and shorter LiPSs due to disproportionation reaction,[92] is not recommended for XPS study. Li_2S_4 was synthesized by stoichiometrically mixing elemental S_8 and Li_2S_2 in DOL/DME (v/v = 1:1).[54] Then mesoporous carbon and PENDI were added into the Li_2S_4 solution successively (**Figure 2-6a**). Addition of mesoporous carbon provides a large surface area for the reaction between PENDI and LiPSs, as well as simulating the composition in real sulfur cathode. The well mixed mixture was casted on silicon wafer, followed by heat treatment at 50 °C for 4 hours to remove solvent, forming a cathode film for XPS experiments. PENDI was added gradually to form two test samples with different concentration of PENDI, labeled as LiPS-C-PENDI-2 and LiPS-C-PENDI-1. The molar ratios between NDI groups and Li_2S_4 are 1:2 and 1:1 for LiPS-C-PENDI-2 and LiPS-C-PENDI-1, respectively. For comparison, samples of LiPS (Li_2S_4, **Figure 2-6b**), and LiPS-C (Li_2S_4 + mesoporous carbon, **Figure 2-6c)** were fabricated and compared.

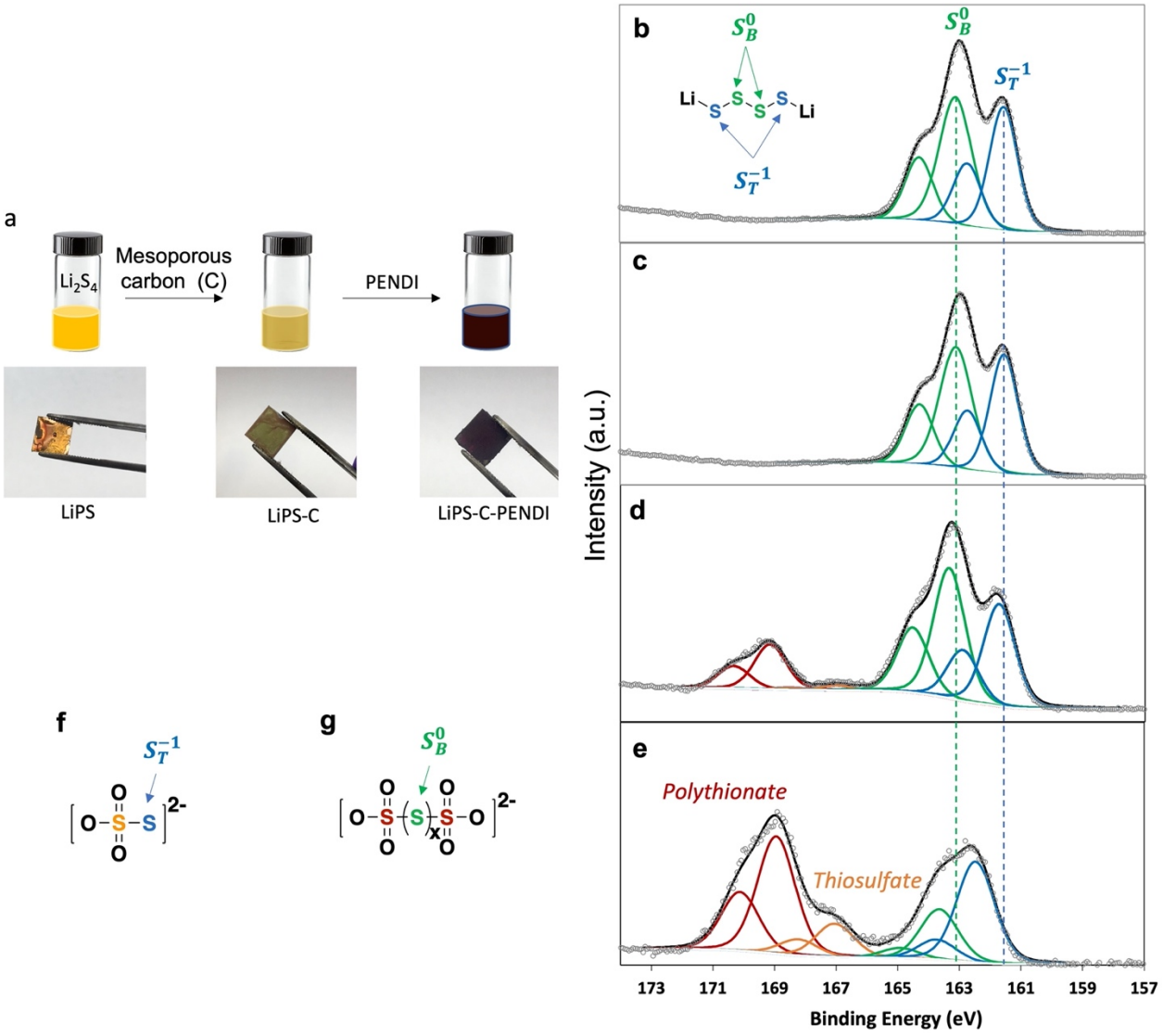

Figure 2-6. (a) Optical images of samples of LiPS, LiPSs-C, and LiPS-C-PENDI for XPS experiments. S2p XPS spectra of LiPS (b), LiPS-C (c), LiPS-C-PENDI-2 (d), and LiPS-C-PENDI-1 (e); (f) thiosulfate and (g) polythionate complexes: blue = sulfur in thiosulfate that bears the negative charge, green = bridging sulfur in the polythionates.[34]

The XPS spectrum of LiPS (**Figure 2-6b**) shows two $S2p_{3/2}$ contributions at 161.6 and 163.0 eV with a ratio around 1:1, referring to the terminal (S_T^{-1}) and bridging (S_B^0) sulfur atoms. This result shows a typical XPS spectrum of Li_2S_4.[34] The XPS spectrum of LiPS-C (**Figure 2-6c**)

shows the similar result to LiPS, which suggests that the mesoporous carbon neither brings in a new source of sulfur peaks nor changes the state of Li_2S_4. After adding PENDI, LiPS-C-PENDI-02 spectrum (**Figure 2-6d**, **Table 2-2**, NDI:Li_2S_4 = 1:2 by mole) exhibits two higher binding energy contributions at 161.8 and 163.4 eV, which represent a + 0.3 eV and + 0.4 eV shift for S_T^{-1} and S_B^0, respectively. We attribute the shifts of $S2p_{3/2}$ peaks in LiPS-C-PENDI-2 spectrum to the interaction between LiPSs with electron-deficient NDI groups: electrons are withdrawn from S due to the electron deficiency of C=O groups in NDI. After doubling the amount of PENDI, this interaction becomes more significant in the spectrum of LiPS-C-PENDI-1 (**Figure 2-6e**, **Table 2-2**, NDI:Li_2S_4 = 1:1 by mole) as suggested by the shift of binding energies of S_T^{-1} and S_B^0 by + 0.9 and + 0.6 eV, respectively.

Table 2-2. Binding energy (eV) of S2p XPS spectra.*

Samples	S_B^0	Peak shift of S_B^0	S_T^{-1}	Peak shift of S_T^{-1}
LiPS	163.0	0 eV	161.5	0 eV
LiPS + C	163.0	0 eV	161.5	0 eV
LiPS-C-PENDI-2	163.4	+0.4 eV	161.8	+0.3 eV
LiPS-C-PENDI-1	163.6	+0.6 eV	162.4	+0.9 eV

**LiPSs + C is used as reference for calculating the peak shift of S_B^0 and S_T^{-1}.*

2.3.4 Redox Properties of NDI

The redox properties of NDI were investigated by CV spectrum with dibutyl-NDI (dbNDI) as model compound. As shown in **Figure 2-7a**, NDI exhibits a stepwise reduction process at 2.53 and 2.45 V *vs*. Li/Li^+ in the operation voltage window of S cathode (1.5-3.5 V *vs*. Li/Li^+). Li_2S_8 is selected as a representative LiPSs to simulate the LiPSs environment at the initial discharge stage.

Li_2S_8 (**Figure 2-7b,** line in red) is reduced at 2.37 and 2.16 V *vs.* Li/Li^+ separately, which corresponds to the two discharge plateaus of sulfur cathode. Then we mixed dbNDI with Li_2S_8 in different molar ratios, followed by CV measurements. When we add increased concentration of Li_2S_8 into dbNDI solution, the reduction peaks of dbNDI decrease first with the molar ratio between Li_2S_8 and dbNDI of 1 : 3 (**Figure 2-7b,** line in blue) and 2 : 3 (**Figure 2-7b,** line in green), and then disappear after adding equal molar concentration of Li_2S_8 (**Figure 2-7b,** line in orange). This demonstrates that dbNDI is reduced gradually with increasing concentration of Li_2S_8 before the CV measurements.

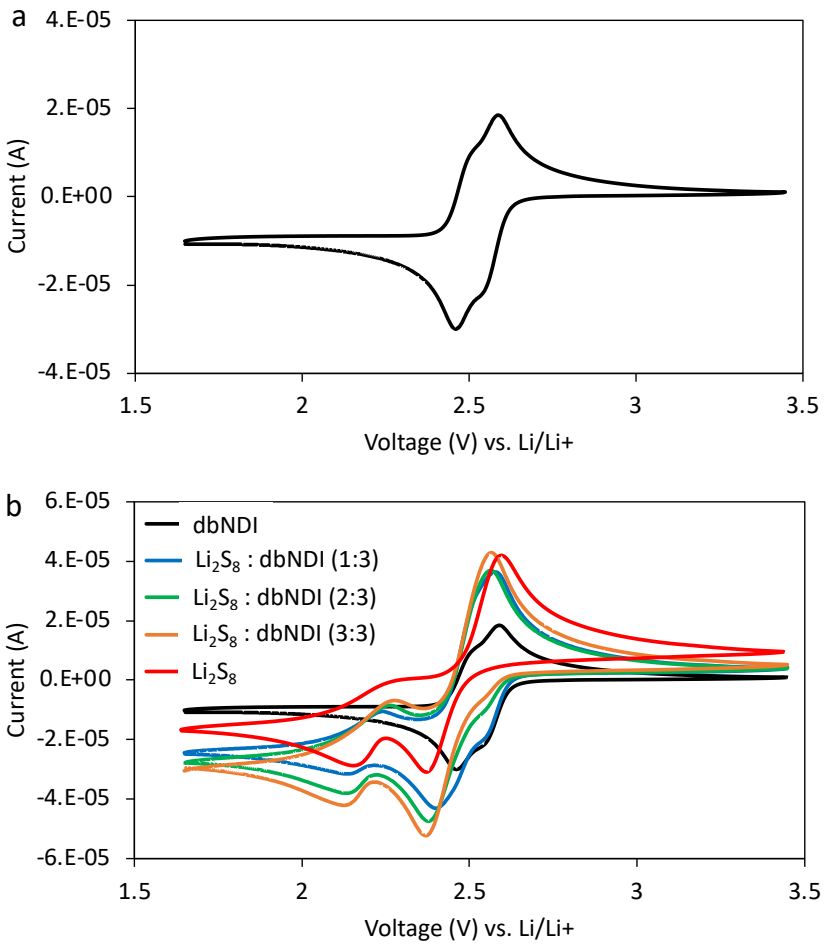

Figure 2-7. (a) CV spectra of a model compound dbNDI; (b) CV spectra of dbNDI and Li_2S_8 mixed solutions in DOL/DME (v/v = 1:1) with varying ratios. (Scan rate = 0.01 V/s).

We further studied the reduction process of NDI by investigating the change of UV-Vis absorption spectra. As shown in **Figure 2-8a**, the solutions of dbNDI and Li_2S_8 in DOL/DME (v/v = 1:1) are colorless and yellow, respectively. We first measured the absorption spectra of dbNDI and Li_2S_8 individually before mixing them together. After adding dbNDI into the Li_2S_8 solution, the color of the solution changes to dark black immediately. We then varied the molar ratio between dbNDI and Li_2S_8 from 1:1 to 1:6, followed by UV-Vis spectrometry measurements. As shown in **Figure 2-8a**, dbNDI (line in purple) in neutral state shows characteristic absorption peak at 359 nm. After adding Li_2S_8 solution with a molar ratio of 1 : 1, the peak of neutral dbNDI (359 nm) decreases slightly and a new peak at 483 nm develops, which corresponds to the $dbNDI^{\cdot-}$ radical anion.[81] When the ratio of dbNDI : Li_2S_8 increase to 1 : 2, more neutral dbNDI is reduced into $dbNDI^{\cdot-}$ radical anion as indicated by the decrease of peak at 359 nm and increase of peak at 483 nm simultaneously. Meanwhile, the characteristic peak of $dbNDI^{2-}$ dianion appears at 407 nm and increases rapidly with increasing concentration of Li_2S_8. Therefore, in with LiPSs, NDI converts to radical anion and dianion gradually (**Figure 2-8b**). The existence of NDI^{2-} dianion has been proven to strongly interact with Li^+,[81] which could entrap LiPSs through the electrostatic force.

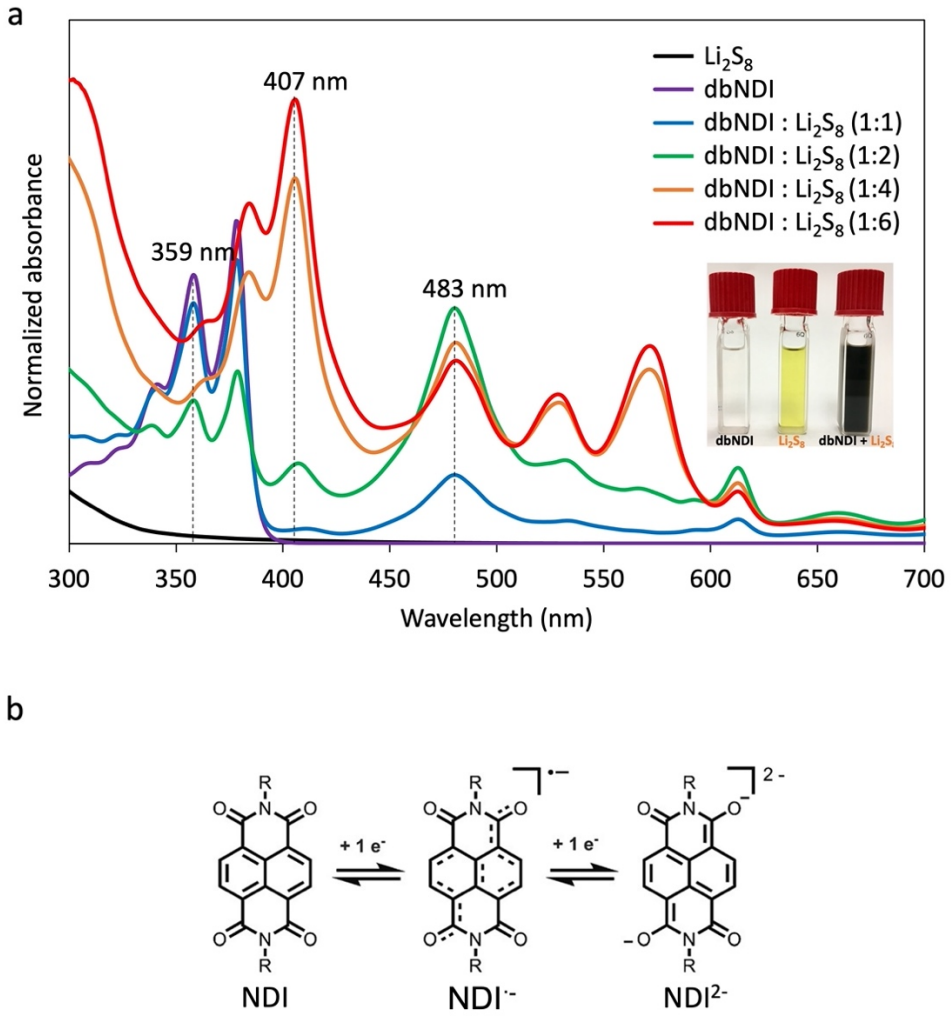

Figure 2-8. (a) UV-Vis spectra of dbNDI and Li_2S_8 mixture in DOL/DME (v/v = 1:1) with different ratios; (Inset) Optical image of solutions of dbNDI, Li_2S_8 and their mixture with equal molar ratio in DOL/DME; (b) Two-step reduction process of dbNDI to form $dbNDI^{\cdot-}$ radical anion and then NDI^{2-} dianion.

2.3.5 Oxidation of LiPSs Mediated by PENDI

Besides the peak shifts of S_T^{-1} and S_B^0, LiPS-C-PENDI-2 spectrum (**Figure 2-6d**) shows two more sulfur environments compared with LiPS-C (**Figure 2-6c**). The new $S2p_{3/2}$ peak at 166.9 eV agrees with the binding energy of polythionate complexes. Another new weak $S2p_{3/2}$ peak at

168.8 eV refers to the binding energy of thiosulfate. Compared with LiPS-C-PENDI-2, the spectrum of LiPS-C-PENDI-1 with higher concentration of NDI (**Figure 2-6e**) shows stronger peaks of both polythionate complexes and thiosulfate. We attribute the formation of thiosulfate and polythionate to the oxidation of LiPSs. Similar LiPSs conversion was observed in Nazar's reports where metal oxides were used as redox mediators for S cathode.[77] Metal oxides with redox potential in the electrochemical window of 2.4 V-3.5 V vs. Li/Li^+ were shown to oxidize LiPSs into thiosulfate, which further confines LiPSs by catenation reaction to produce polythionates and lower LiPSs. Besides metal oxides, this redox mediator effect *via* thiosulfate-polythionate conversion also extended to other materials, such as GO.[34] Redox potential of NDI in our design also falls in the electrochemical window (**Figure 2-7a**). Similarly, we propose a two-step reaction route of LiPSs with PENDI binder as shown in **Equation 2-1** and **Equation 2-2**: First, as shown in **Equation 2-1**, LiPSs is oxidized into thiosulfate mediated by NDI. In addition to the desired redox potential in the target range, an abundant sources of oxygen, such as metal oxides and GO is required for the transformation of LiPSs to thiosulfate.[34] Oxide, hydroxyl, and carbonyl groups on the surface of mesoporous carbon (**Figure 2-9**) is proposed as source oxygen for the transformation in our design. Second, as shown in **Equation 2**, catenation of LiPSs to thiosulfate to produce the polythionate $S_xO_6^{2-}$ and a lower LiPSs was observed. Polythionate complexes with x = 3 to 6 are mostly observed.[93] Both polythionate and Li_2S_2/Li_2S have low solubilities in DOL/DME electrolyte, further preventing the dissolution of LiPSs. Different from the metal oxide redox mediators[77], our design incorporates an organic redox mediator molecularly engineered as a component of a polymeric binder.

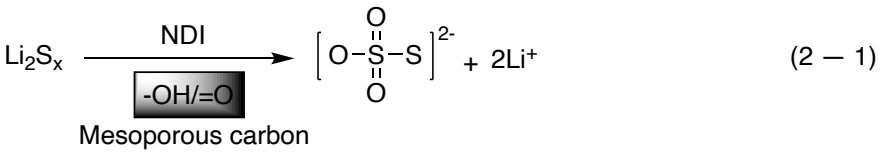

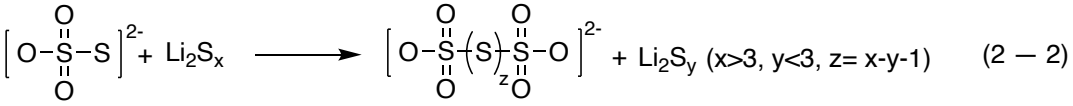

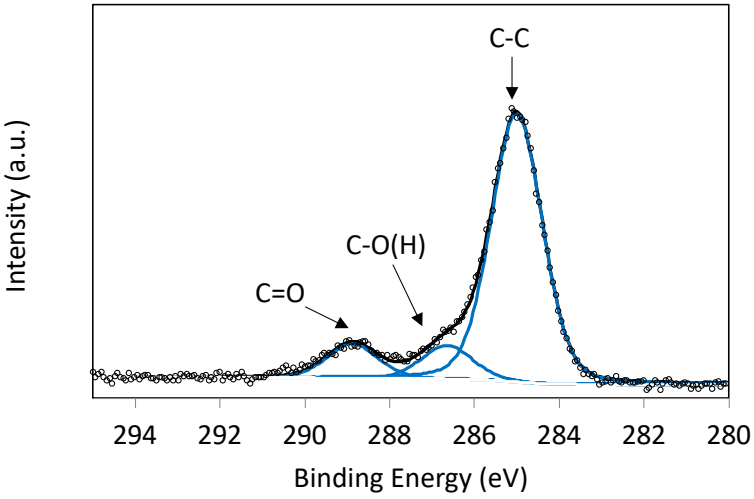

Figure 2-9. C1s XPS spectrum of mesoporous carbon.

Compared with LiPS-C, significant deference in the ratio between $S_T^{-1}$and S_B^0 peaks are observed for LiPS-C-PENDI-2 (**Figure 2-6c**) and LiPS-C-PENDI-1 (**Figure 2-6d**). Based on the proposed mechanism (**Equation 1** and **Equation 2**), we attribute this to the differences in distribution of products in each sample. As shown in **Figure 2-6f** and **Figure 2-6g**, thiosulfate and polythionate provide strong contribution of $S_T^{-1}$and S_B^0, respectively. As an intermediate, the peak intensity of thiosulfate and its ratio to polythionate in XPS spectrum will be affected by the relative reaction rates of **Equation 1**, which produces thiosulfate, and **Equation 2**, which consumes thiosulfate. In the case of LiPS-C-PENDI-2, the negligible signal of thiosulfate demonstrates that

majority of the thiosulfate has transformed into polythionate which enhances to the signal of S_B^0 at 163.4 eV. With the molar ratio of NDI:Li_2S_4 as 1:2 in LiPS-C-PENDI-2, we speculate that **Equation 2** conducts a faster reaction rate, which converts the generated thiosulfate from **Equation 1** to polythionate immediately, leading to the fast disappearance of thiosulfate. In the case of LiPS-C-PENDI-1 with NDI:Li_2S_4 as 1:1 by mole, the doubled concentration of NDI will speed up **Equation 1** greatly, which increases the peak ratio between thiosulfate to polythionate. The accumulated thiosulfate, consequently, enhances the peak intensity of S_T^{-1} at 162.4 eV. Meanwhile, accompanied by the formation of polythionate, LiPSs would be converted into shorter LiPSs. The deposition of insoluble Li_2S_2/Li_2S on the sample would further enhance the intensity of S_T^{-1} peak.

2.3.6 Cell Performances

To evaluate the effect of PENDI binder on LiPSs confinement, sulfur cathodes using PENDI as binders were fabricated. Sulfur cathodes using polyvinylidene fluoride (PVDF) as a polymeric binder were fabricated as a reference. As shown in **Figure 2-10**, test cells with the sulfur cathode shows initial specific discharge capacity of 1207 mAh/g at 0.1 C rate. Then the specific discharge capacity stabilizes to 890 mAh/g after 200 cycles, corresponding to discharge capacity retention of 74%. Although the specific discharge capacity of the resulting cathode with PVDF reaches around 1179 mAh/g initially, capacity of the cathode decreases dramatically in the first 10 cycles, followed by smooth decrease. The discharge capacity remains 526 mAh/g after 100 cycles (capacity retention of 43%), and 315 mAh/g after 200 (capacity retention of 27%). Compared to cell with PVDF binder, cell with PENDI binder produces remarkably increased discharge capacity

retention by 47% after 200 cycles. The comparisons between cathode performances with different binders shows that PENDI is superior in confining LiPSs and improving capacity retention.

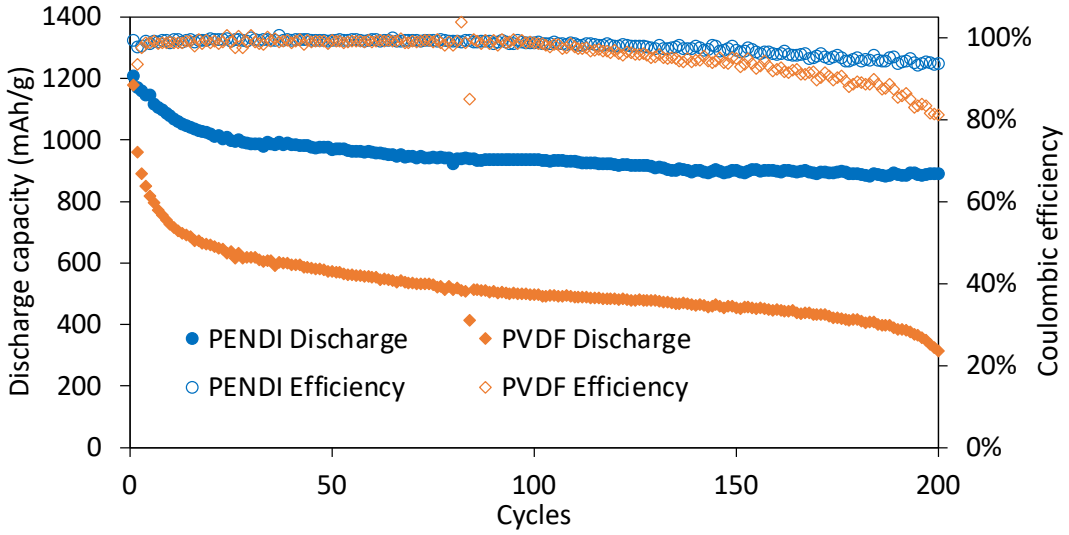

Figure 2-10. Cell performance of cathodes with PENDI and PVDF binders (sulfur loading = 1 mg/cm^2).

The LiPSs confinement is confirmed by the SEM characterizations of cathodes with different binders after 50 cycles (**Figure 2-11**). The cathodes were washed with DOL/DME to remove electrolyte and soluble LiPSs before SEM experiments. Before cycling, both fresh cathodes with PENDI and PVDF binders demonstrate similar porous morphology, consisting of typical MJ430 mesoporous carbon with diameter around 1-5 μm (**Figure 2-11**).[69] After 50 cycles, precipitate layers are observed on both cathodes at the fully discharged state (1.7 V vs. Li/Li$^+$).[92] Differently, due to its strong interaction with LiPSs and redox mediator effect, PENDI binder prevents the loss of polysulfides by confining soluble LiPSs and converting them into principates. Consequently, cathode with PENDI binder possesses a thicker, more uniform precipitate layer without visible aggregations. The resulting discharge capacity at 50th cycle reaches 969 mAh/g, which is much higher than that (571 mAh/g) of cathode with PVDF binder. After converting to

fully charged state (2.9 V vs. Li/Li^+), the cathode with PENDI binder exhibits porous morphology again, showing significant decrease in the volume of precipitate layer compared with the fully discharged state. We attribute the volume decrease of precipitate layer to the effective conversion from Li_2S at fully discharged state to denser sulfur at fully charged state.[18]

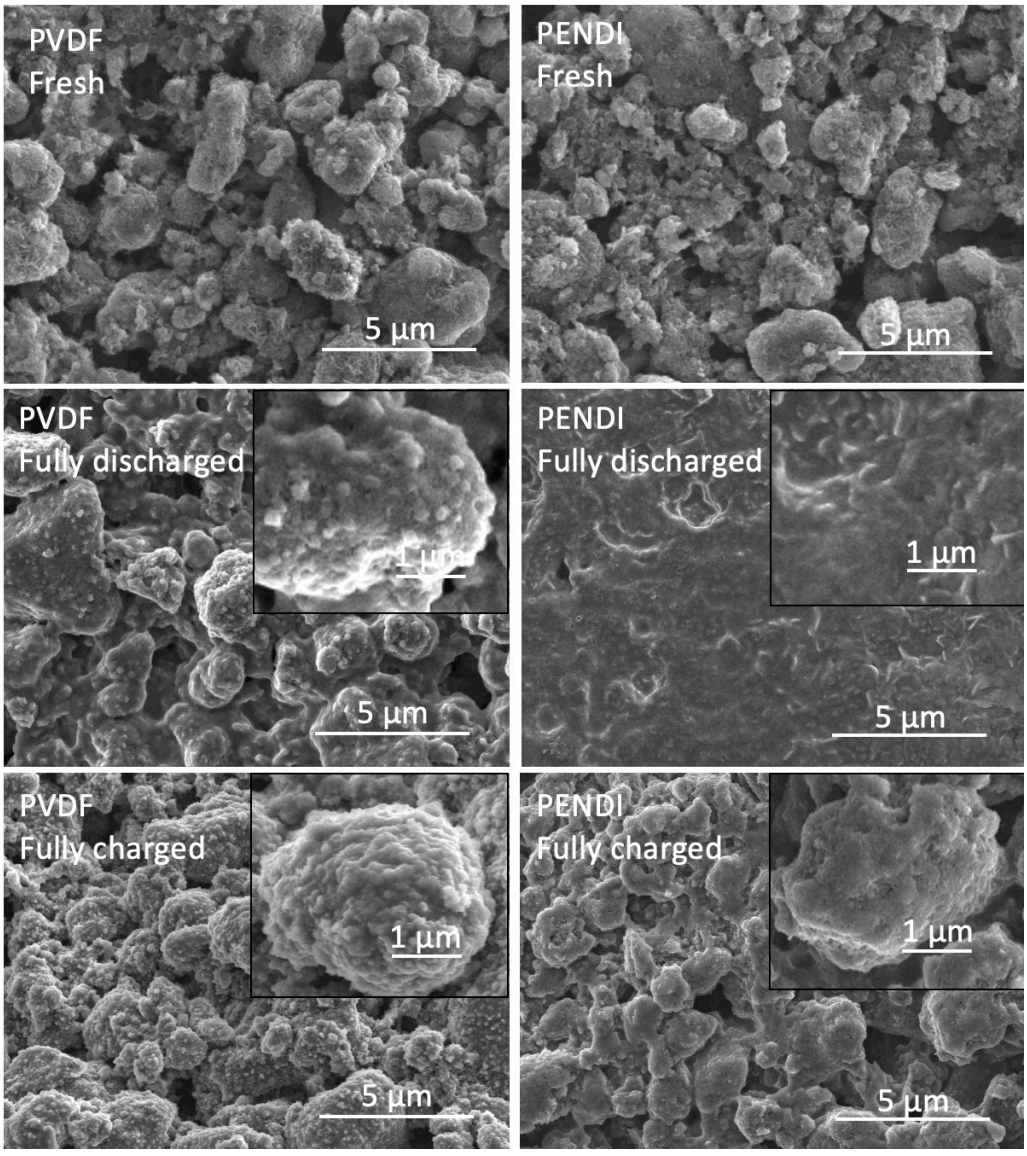

Figure 2-11. SEM images of cathodes with PENDI and PVDF binders at the fully discharged and fully charged states of the 50th cycle at 0.1C rate. SEM images of fresh cathode before cycling are used for comparison.

The discharge/charge voltage profile of cathodes at different cycles are shown in **Figure 2-12a and 2-12b**. All cathodes demonstrate typical discharge curve with two plateaus, related to the phase change reactions between solid and liquid LiPSs. Cathode with PVDF binder demonstrates much faster capacity decay, resulting from faster polysulfides loss. Over potentials at the beginning of the 1st charge curves are observed for both cathodes. This universal characteristic over-potential peak was referred to the two-phase reaction of converting solid Li_2S into liquid LiPSs.[94] This extra driving force is needed to nucleate the new phase (soluble LiPSs). This over-potential is known to disappear if soluble polysulfide (0.2 M, Li_2S_8) was added into the electrolyte intentionally. In the case of cathode with PVDF binder (**Figure 2-12b, inset)**, the over-potential peak shows a clearly decreasing trend with the increasing cycles. The peak disappears completely at the 50th cycle, which demonstrates that considerable amount of soluble polysulfides nuclei has already existed in the electrolyte, therefore extra free energy for phase nucleation of soluble polysulfides is not required anymore.[94] Conversely, the over-potential peak of cathode with PENDI binder still appears even after 50 cycles without fading (**Figure 2-12a, inset**). We speculate that this is because soluble LiPSs have been entrapped and converted into solid Li_2S efficiently at fully discharged state. Extra free energy is still needed due to the lack of soluble LiPSs at the beginning of charge process.

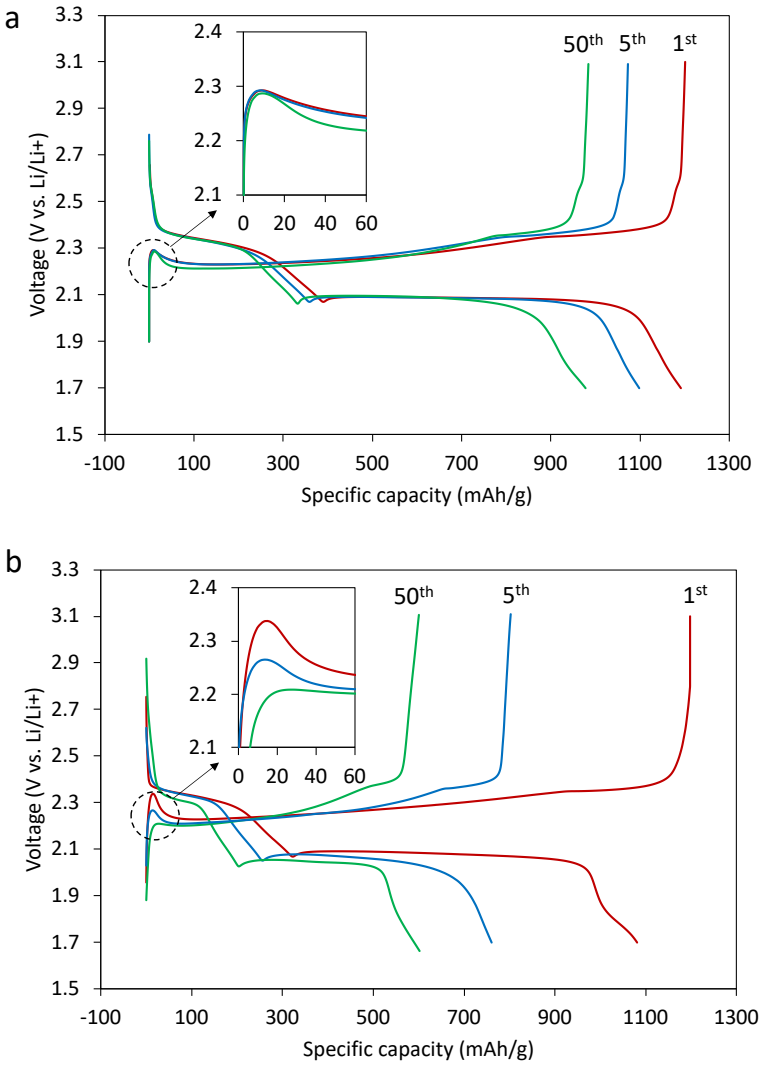

Figure 2-12. The discharge/charge voltage profiles of cathodes with PENDI binder (a) and PVDF binder (b) at different cycles. (Inset) Zoom-in images of the over-potential peaks at the beginning of the charge curves. Unites in both insets are the same as the figures.

2.4 CONCLUSIONS

In summary, I designed a multi-functional binder based on redox active NDI groups to achieve sulfur cathode with high-capacity retention. The resulting PENDI binder prevents the dissolution of LiPSs through the redox mediation and chemical interaction with NDI groups. The

redox active NDI groups mediate the transformation of soluble long-chain LiPSs into insoluble short-chain LiPSs and polythionate, which reduces the accumulation of soluble LiPSs. Meanwhile, NDI groups demonstrate strong interactions with LiPSs *via* dipole-dipole interaction with abundant carbonyl groups. The existence of NDI^{2-} dianion also contributes to trap LiPSs *via* ion-dipole interactions. The cell performance measurements show PENDI binder is superior in improving capacity retention of S cathode compared to PVDF.

CHAPTER 3: TUNING SELF-HEALING AND MECHAINCAL PROPERTIES OF PENDI/TRIPY POLYMERS

This chapter is reproduced from the article, Jiaxu Qin *et al*. "Tuning self-healing properties of stiff, ion-conductive polymers" *J. Mater. Chem. A*, 2019, 7(12): 6773-6783.[95]

3.1 INTRODUCTION

3.1.1 Motivation

Besides dissolution of LiPSs, the volume expansion/shrinkage problem of cathode active materials during the discharge/charge processes also causes significant capacity decay. The repeated volume change of active materials induces the formation of cracks due to tension stress. Other processes, including fabricating cathode film, packing coin cell, also bring more risk of cracking. The irreversible formation of cracks breaks the conductive pathways of both electrons and ions, consequently leading to capacity decay. This issue becomes more pronounced when fabricating sulfur cathode with higher sulfur loading and larger cathode area.

Here, I propose to utilize the reversible interactions in self-healing materials to dissipate the strain energy of sulfur cathode. The reversible interactions enable the formation of crosslinked structure which enhances the mechanical properties. The breaking of reversible interactions helps dissipate strain energy to prevent cracking. Despite the formation of cracks, the self-healing nature enables the material to self-heal under heat or light treatments. Consequently, sulfur cathode with self-healing binder could stand much higher tension stress and then enable the fabrication of sulfur cathode with higher sulfur loading.

Besides energy storage, materials exhibiting self-healing behaviors are very desirable for electrochemical devices across a number of emerging applications.[96–100] For example, artificial skin, flexible electronics, sensors, and soft robotics may all suffer from strain-induced cracking during normal operation due to mechanical activity, resulting in loss of conductive pathways and reduction in device performance.[19,101–103] Introduction of a self-healing feature into such devices can help reform these pathways after breakage, with associated recovery of performance.[104–106] Organic polymers are a natural choice of platform to introduce self-healing behavior into electrochemical devices, given their combined good processability, mechanical flexibility, and inexhaustible varieties of molecular structures.[107–109]

In general, self-healing in polymers results from the reformation of broken molecular linkages between polymer chains. Self-healing polymers are usually crosslinked *via* reversible noncovalent interactions[110–117] or dynamic covalent interactions,[113,118,119] with the resulting macro-scale properties (such as self-healing temperature and tensile modulus) being determined by the overall strength and density of such crosslinking interactions. These interactions are, in turn, tightly coupled to the spatial structure of the polymers at the molecular level. Most previous studies take the logical approach of altering macro-scale properties through re-engineering of molecular structure, including modification of polymer backbones[108,120] and side-chains,[21,22] copolymerization,[22,23] and hybridization of polymers and inorganic materials.[24,25] Each new target application requires an entirely new polymer design, which makes most individual materials only suitable for a small group of applications, due to the narrow range of properties achievable for a particular structure.

For instance, an effective battery binder would likely require a vastly different tensile modulus than a biosensor,[126–129] as well as the ability to self-heal under a wide range of operating

temperatures,[130,131] as opposed to the narrow range of temperatures associated with the human body.[132,133] Given the tight coupling of molecular structure to properties,[134] common sense dictates that these two applications would thus require polymers with vastly different designs. However, the design, synthesis, and optimization of entirely new organic materials is a challenging and time-consuming endeavor, with the resulting new materials suffering from their own narrow range of usability. While this design-property feedback loop has encouraged development of a wide range of creative molecular structures, it has also limited the ability of the field to respond to new challenges on a timescale that allows widespread utilization of self-healing polymers in real devices.

3.1.2 Rational and Overview

In this chapter, I introduce a self-healing supramolecular polymer system in which the polymer PENDI – containing naphthalenediimide (NDI) side chains – is physically crosslinked by trivalent linker triPy-containing pyrene (Py) units *via* reversible face-to-face quadrupole-quadrupole interactions between NDI and Py. To regulate the self-healing and mechanical properties of the polymer system, we first optimized the spatial structure of PENDI. This method tunes the crosslinking behavior by modulating polymer structure directly. Besides, we report a novel strategy to decouple the crosslinking behavior, including binding strength and density, of the self-healing systems simply by adding small molecules. By adding small molecules which also contain these functionalities, we demonstrate modulation of different binding modes between NDI and Py, which possess different strengths via stoichiometry control, as well as modulation of the density of interactions between NDI and Py units on polymer chains (as opposed to interactions with the free, small molecules). This allows us to develop a series of self-healing materials in

which both crosslinking density and binding strength are tunable without modifying the polymer structure or composition. Consequently, self-healing polymer system PENDI/triPy with tunable self-healing and mechanical properties is achieved. The resulting system possesses good ionic conductivity and good compatibility with carbon. Finally, we demonstrate the possible application in different areas.

3.2 EXPERIMENTAL SECTION

3.2.1 Materials

Solvents, including anhydrous tetrahydrofuran (THF, 99.9%, Aldrich), anhydrous dimethylformamide (99.8%, Aldrich), anhydrous dichloromethane (DCM, 99.8%, Aldrich), for chemical synthesis were purified by distillation. Mesoporous carbon MJ430 (Porous Carbon CNovel™; Toyo Tanso USA, Inc.) was washed with 2 M HCl in ethanol for purification. Anhydrous 1,3-dioxolane (DOL, 99.8%, Aldrich), anhydrous 1,2-dimethoxythane (DME, 99.8%, Aldrich) were dried with 4Å molecular sieves and then stored in an argon-filled glovebox (Vacuum Technology Inc, <0.01ppm H_2O and O_2) before use. Lithium bis-(trifluoromethanesulfonyl)imide (LiTFSI) and $LiNO_3$ were purchased from 3M and dried at 120°C under argon, then stored/used in an argon-filled glovebox. Lithium chips (99.9%, 15.6mm diameter, 0.45mm thickness) and other cases used for coin cell assembly (including o-ring, spring, spacer, caps) were purchased from MTI Corp and stored/used in an argon atmosphere glove box. All other chemicals and reagents were purchased from Aldrich and were used as received without purification.

3.2.2 Characterization

The ^{1}H and ^{13}C NMR spectra were recorded on a Bruker AV500 spectrometer using $CDCl_3$ or d_6-DMSO as a solvent. Mass spectrometry (MS) was performed on a Bruker APEX III 47e Fourier transform mass spectrometer. Thermogravimetric (TGA) analyses were conducted on a Shimadzu TGA-50 thermogravimetric analyzer under nitrogen at a heating rate of 10 °C min^{-1}. UV-vis spectra were recorded on a Varian Cary 5000 UV-Vis-NIR spectrophotometer. All samples used for UV-vis tests were prepared with dichloromethane as the solvent. DSC measurements were performed in a heat–cool–heat cycle (–40 to 220 °C, 10 °C min^{-1}; 220 to –40 °C, –10 °C min^{-1}; –40 to 220 °C, 10 °C min^{-1}). About 5 mg of the sample was used for each test. A Bruker ICON AFM in the contact mode was used to determine the Young's modulus of polymer films. AFM tips were calibrated with a radius of around 10 nm, spring constant of around 0.4 N m^{-1}, and sensitivity of around 50 nm V^{-1}. An OlymScope was used for optical imaging tests. NMR spectra, UV-Vis spectra experiments were conducted the same as **Section 2.2.2**. All the samples for UV-Vis, XPS, CV experiments were prepared in a glove box filled with argon.

3.2.3 Synthesis of PENDI

Materials are prepared and synthesized based on **Section 2.2**. PENDI was synthesized following the procedures described in **Section 2.2.3**-**Section 2.2.6**. TriPy crosslinker and dbNDI were prepared based on **Scheme 3-1**.[120,135]

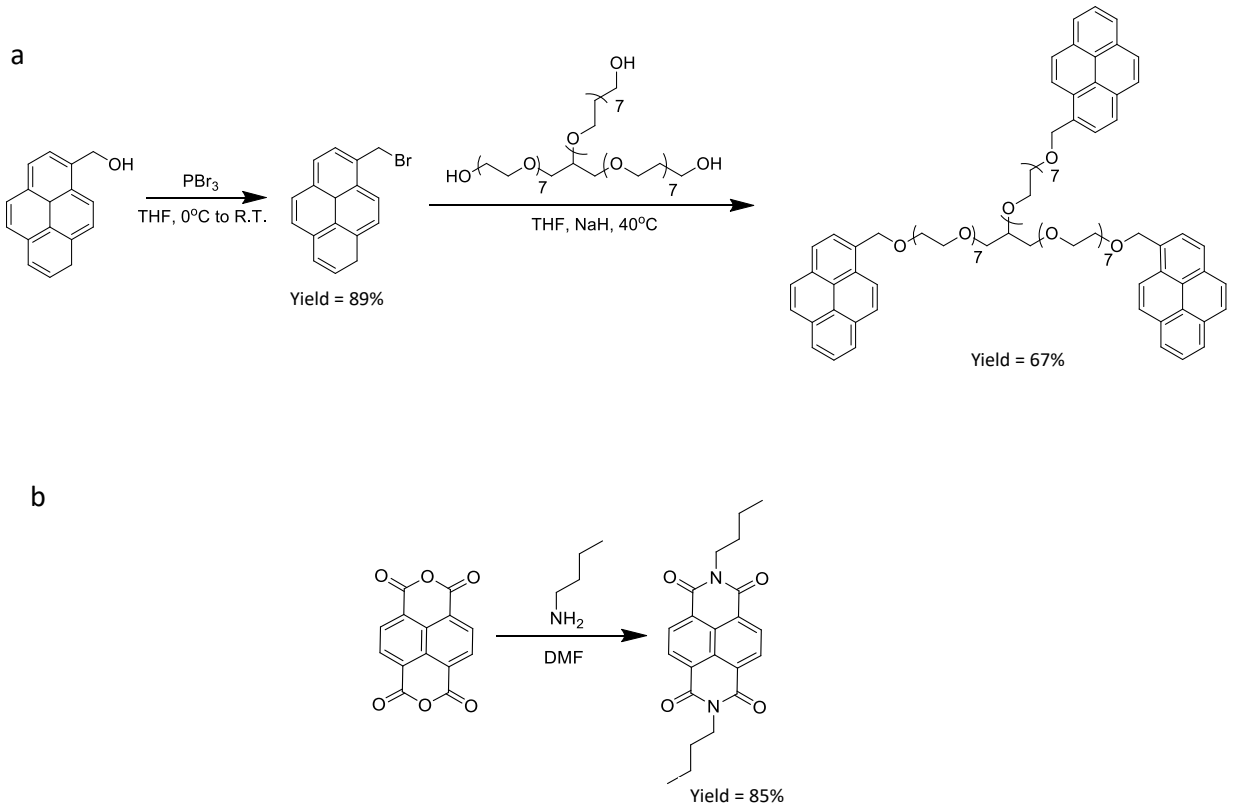

Scheme 3-1. Synthetic routes of triPy (a) and dbNDI (b). TriPy crosslinker and dbNDI were prepared according to literature procedures with modifications.[120,135]

3.2.7 Determination of Quadrupole–Quadrupole Charge Transfer (CT) Interaction Strength

The association constant of different CT binding modes was estimated by the UV-Vis dilution method: the absorbance (A) of the characteristic peak is measured with the varying concentration (c, 0.002–0.02 M) of the CT complexes. Based on the Beer–Lambert law, **Equation 3-1** shows the relationship between the association constant (K_a), c, and A. By plotting data in figures, K_a can be calculated without requiring the knowledge of constant parameters $\in$ and l. Using this method, the complexation energy of different complexes could be determined, respectively.

$$\frac{c}{A} = \left(\frac{1}{K_a \epsilon l}\right)^{0.5} \frac{1}{A^{0.5}} + \frac{1}{\epsilon l} \qquad (3-1)$$

3.2.8 Self-Healing Measurements

As shown in **Figure 3-1a**, different PENDI/triPy films were fabricated with a diameter of 1 cm and thickness of 0.1 cm. The polymer films were cut into two pieces and brought into contact without additional pressure. Then heat treatments for varying times at different temperatures were conducted, followed by optical imaging tests.

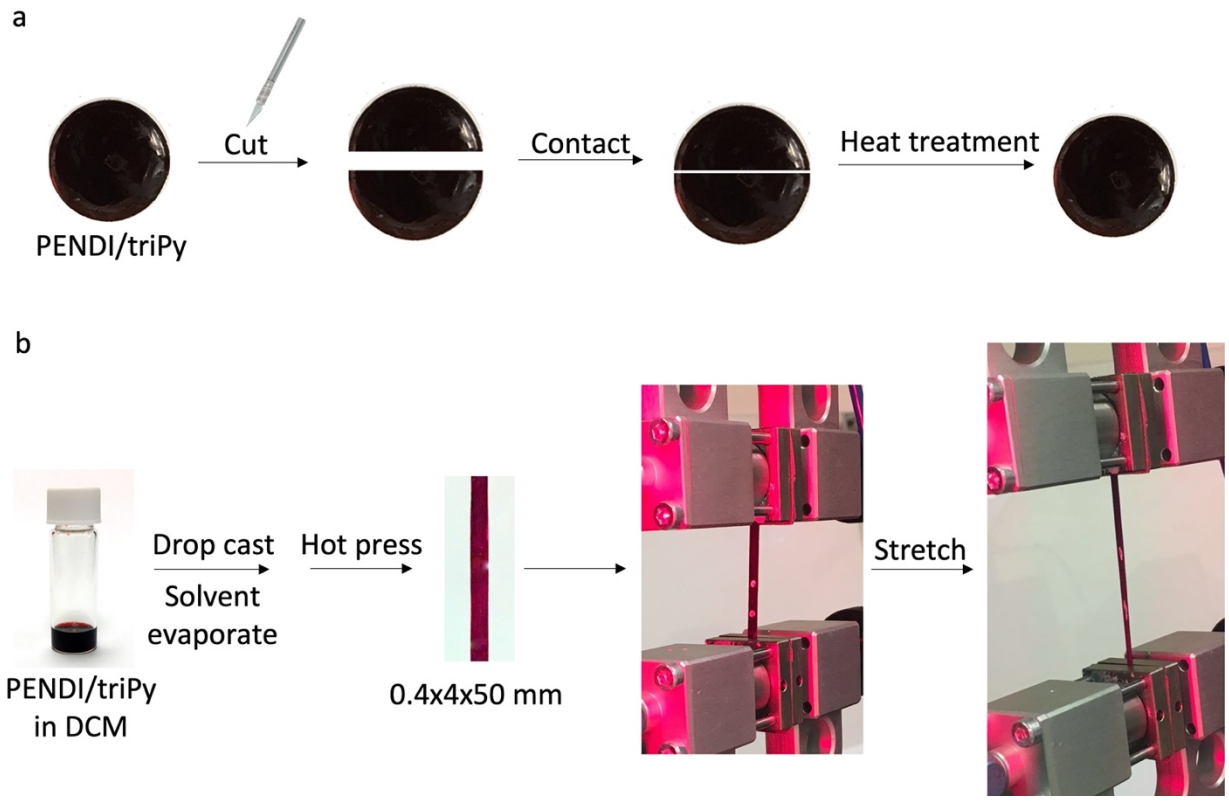

Figure 3-1. (a) Self-healing measurement of PENDI/triPy film by contacting the cut films followed by heat treatment at different temperatures; (b) Sample fabrication and uniaxial tensile tests of PENDI/triPy films.

3.2.9 Uniaxial Tensile Measurements

As shown in **Figure 3-1b**, PENDI and triPy were dissolved in DCM and then cast on glass, flowed by solvent evaporation under vacuum at 50 °C to remove DCM. The dried PENDI/triPy polymer films were fabricated into a specific size of 0.4 × 4 × 50 mm by hot press. The uniaxial tensile tests were conducted using a LoadFrame (Instron-5585) at room temperature with a loading rate of 50 mm/min.

3.2.10 Fabrication of Sulfur Cathode

The fabrication of sulfur cathode follows the same procedure as **Section 2.2.7** except that the binders used in this section is PENDI/triPy.

3.2.11 Assembly of Lithium–Sulfur Coin Cell

The assembly of lithium-sulfur coin cell in this section is the same as **Section 2.2.8**.

3.3 RESULTS AND DISCUSSION

3.3.1 Characterization of the Intermolecular Interactions

To understand the nature of intermolecular interactions between NDI and Py derivatives, model compounds dibutyl-NDI (dbNDI) and pyrene (Py) were studied. The formation of face-to-face charge transfer (CT) complexes resulting from intermolecular quadrupole–quadrupole interactions between electron-deficient NDI derivatives and electron-rich Py is represented in **Figure 3-2a**. The formation of this complex was confirmed by mixing Py and dbNDI (1:1 in mole) in dichloromethane. As shown in **Figure 3-2b**, the color turns into dark red brown after mixing colorless Py solution and light brown dbNDI solution. The UV-vis experiment in **Figure 3-2c**

demonstrates that the dark red brown color refers to a new absorbance peak at 500 nm wavelength, implying the formation of a 1:1 CT complex between Py and dbNDI.

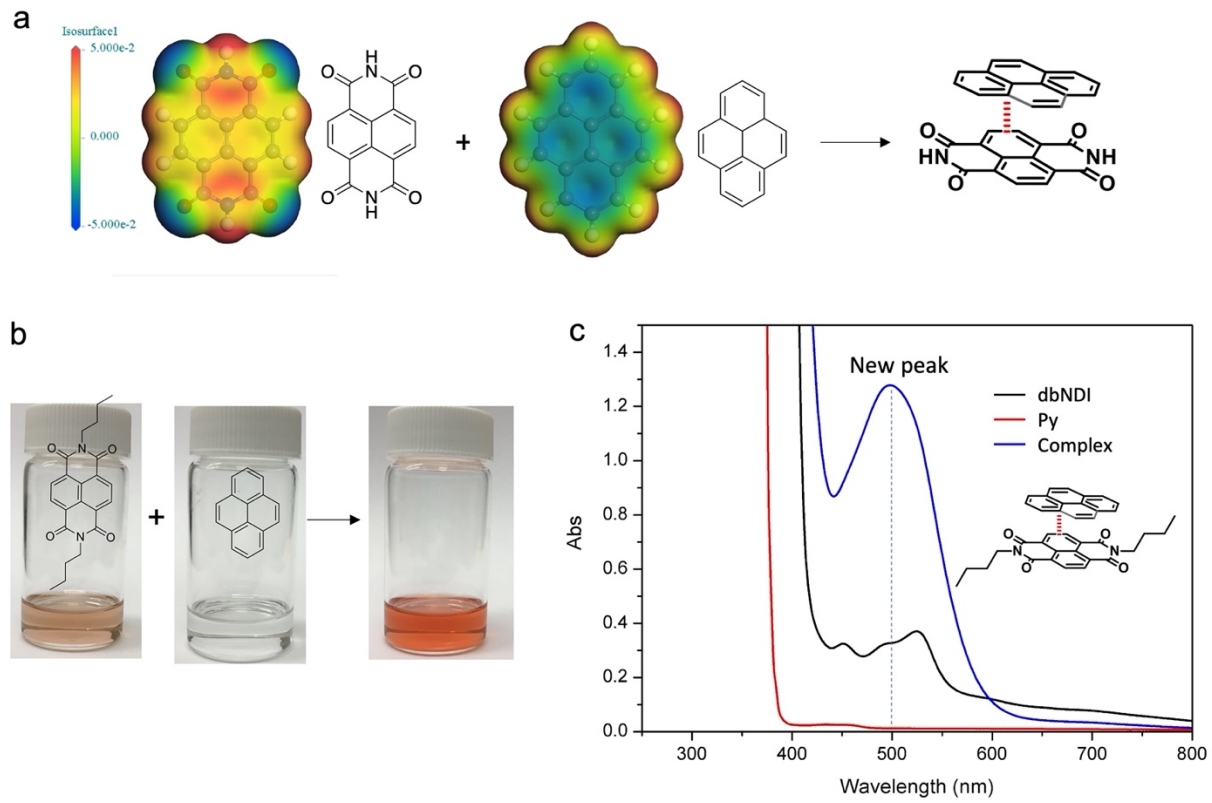

Figure 3-2. Charge transfer complex between Py and NDI derivatives. (a) Electrostatic potentials of electron-deficient 1,4,5,8-Naphthalenetetracarboxdiimide (NDI) and electron-rich Py based on Material Studio DMoL^3 simulation. (b) Optical images and (c) UV-Vis spectra of Py (0.03 M), dbNDI (0.03 M), and their equimolar complex (0.03 M) solutions in dichloromethane at room temperature.

Interestingly, when the molar ratio between dbNDI and Py was changed while maintaining the same overall molar concentration, we found that an additional characteristic absorbance peak emerged at 514 nm when dbNDI was in excess (**Figure 3-3a**). This absorbance peak reached a

maximum value at a dbNDI:Py ratio of 2:1 (**Figure 3-3b**), suggesting a new complex structure of this stoichiometry.

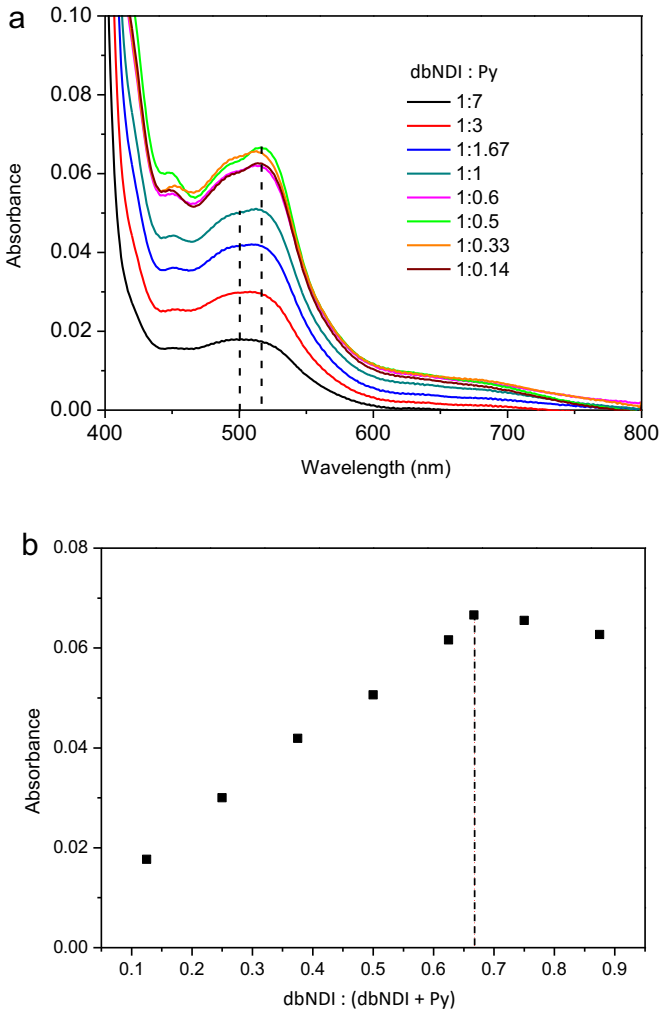

Figure 3-3. (a) UV-Vis spectrum and corresponding (b) Job plot of dbNDI-Py mixture in DCM with various molar ratios (total concentration of dbNDI and Py was kept constant as 0.004 mol/L) at room temperature.

Concurrently, the formation of complexes was observed with different binding modes in the H^1 NMR spectra of dbNDI and Py mixtures. The aromatic ring proton signals are highlighted in **Figure 3-4**. In pure dbNDI, proton **d** was observed to appear as a peak at 8.75 ppm. After mixing

dbNDI and Py in a ratio of 1:3, the position of proton **d** shifted upfield to around 8.53 ppm, presumably due to the shielding effect of Py via π–π interaction. Decreasing the ratio to 1:1 caused only a slight change in the position of this peak; however, further decreasing the amount of Py resulted in a noticeable shift back downfield. This behavior suggests the formation of a new complex in which proton d is shielded less significantly by electron density on Py.

Besides simply shifting positions, the signal of proton **d** on the dbNDI ring also changed the structure with the varying molar ratio: in pure dbNDI, proton **d** possesses a single peak, whereas a small additional peak appeared upon the introduction of an excess of Py (dbNDI:Py = 1:3), implying the formation of a long-lived complex which breaks the symmetry of aromatic protons on dbNDI. This new peak became more apparent when the ratio was increased to dbNDI: Py = 1:1. Upon increasing the concentration of dbNDI even further such that dbNDI is in excess (dbNDI:Py = 2:1 and 3:1), an additional new peak appeared, indicating yet another break in the symmetry and implying the formation of different types of complexes. The synchronicity of both NMR and UV-vis data suggests two types of binding modes in this system corresponding to 1:1 and 2 : 1 ratios of dbNDI : Py, as well as modulation of the dominant binding mode through stoichiometry control.

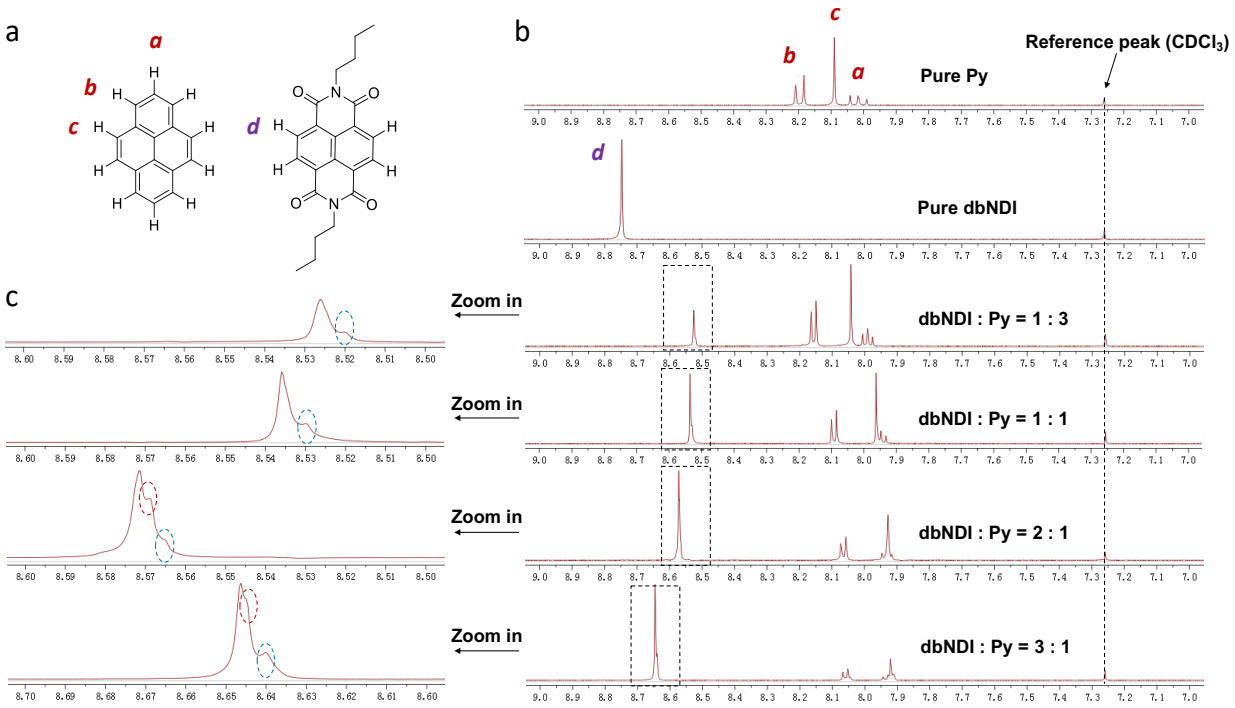

Figure 3-4. NMR spectra of dbNDI and Py mixtures with different molar ratio in chloroform-d. (a) The two model compounds Py and dbNDI. (b) The aromatic ring proton signals of model compounds. (c) The signal peak change of proton d in dbNDI by zooming in the rectangle area in (b).

The average free energies of complexation of these two interaction modes were further estimated by using the UV-Vis dilution method in dichloromethane (DCM) (**Figure 3-5** and **Table 3-1**).[39,40] We found that the free energy of complexation of the 1:1 complex (–8.19 kJ mol^{-1}) is significantly weaker than that of the 2:1 complex (–16.49 kJ mol^{-1}).

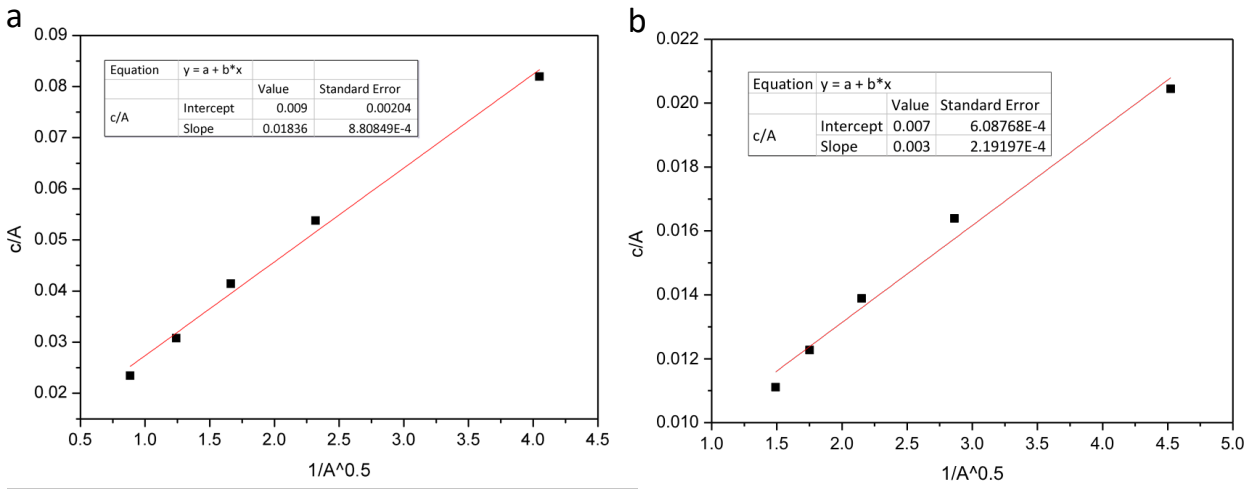

Figure 3-5. UV-Vis dilution method plots of (a) 1:1 complex and (b) 2:1 complex in DCM at room temperature.

Table 3-1. Association Constant and Free Energy of Complexation

Binding modes	Association constant	Free energy of complexation
1 : 1 complex	26.7 M^{-1}	-8.19 kJ/mol
2 : 1 complex	777.8 M^{-1}	-16.49 kJ/mol

The large difference in binding energy of these complexes, in addition to the tunability of NDI/Py interactions based on stoichiometry, makes this combination an intriguing choice for crosslinking units in a self-healing polymer. Here we note a few important points: first, in most self-healing polymers, changing the concentration of crosslinking groups only results in modulation of crosslinking density.[118,120] Interestingly, in our system, it appears that changing the ratio between NDI and Py not only can tune the crosslinking density, but also fundamentally change the predominant binding mode, and therefore the binding energy. This means that, in

principle, we can tune polymer properties over a wide range by simply changing the ratio between NDI units and Py units. Second, when adjusting this ratio, NDI and Py units do not need to come from the polymer side chains. Instead, they can be added in the form of small molecule dopants. Such additives would encourage, and participate in, the formation of one complex over another without altering the number of crosslinking units available. Thus, we can dope small molecules into the polymer to change both binding mode and crosslinking density, providing a general and rational molecular design strategy to control material properties over a wide range without having to change the structure of the polymer itself.

3.3.2 Design of Self-healing Polymers

The aforementioned tunable interaction modes between NDI and Py derivatives were used as the basis for self-healing in our PENDI/triPy supramolecular polymer. Specifically, PENDI/triPy utilizes the triPy crosslinker to reversibly crosslink PENDI *via* π–π interactions between NDI side chains and Py units (**Figure 3-6**). Each feature of this system is selected rationally: the rigid methacrylate backbone of PENDI is expected to provide the PENDI/triPy system with a high Young's modulus, while the oligo(ethylene glycol) (OEG) chains present in both PENDI and triPy provide chain flexibility, which also enhance the Li^+ conductivity. The molecular mobility of NDI side chains can be tuned by modulating alkyl group R, consequently, modulating the binding strength with Py unit. The length of OEG unit is controlled by x, which provides "molecular handle" to adjust ionic conductivity of resulting PENDI polymer.

We designed and synthesized PENDI-C3 (**Figure 3-6a**) as first-generation PENDI by replacing designing alkyl group R as propyl group. As shown in **Figure 3-b**, PENDI-C3 is difficult to form continuous film by drop cast method. The resulting film is brittle, which attributes to the

rigid backbone and the stacking effect between NDI molecules. After adding triPy crosslinker into PENDI-C3 solution with molar ratio between NDI unit and Py unit as 1 : 1, a red continuous film was fabricated. This color change agrees with our previous UV-Vis experiments, implying the formation of CT complex between NDI and Py units.

The self-healing property of PENDI-C3/triPy film was initially tested by optical images comparison of damaged film before and after heat treatment. **Figure 3-6c** shows that the resulting film self-heals the damaged area after heat treatment under 60 °C for 30 mins. However, a lower self-healing temperature, such as near room temperature, is much more desired for practical application in battery system. That's because a lower self-healing temperature could not only endow the system with higher self-healing efficiency, but also avoid the potential risk of side reactions in both electrodes and electrolyte under high temperature.

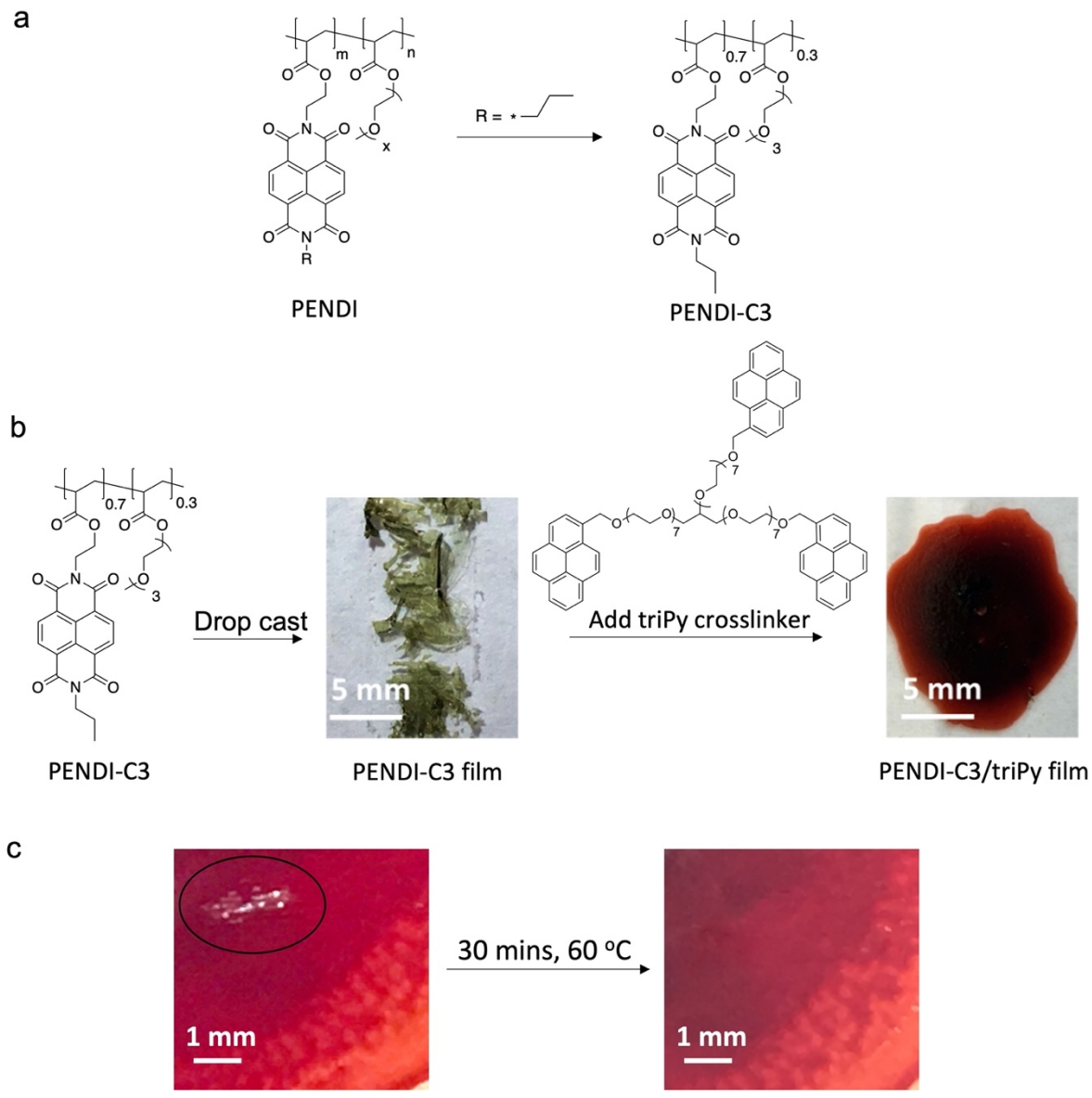

Figure 3-6. Fabrication and self-healing property experiment of PENDI-C3/triPy film. (a) Design of PENDI-C3 as the first generation of PENDI polymer. Mn = 34.6 kDa, PDI = 1.09; (b) Fabrication of PENDI-C3 and PENDI-C3/triPy films by drop cast method. Dissolve PENDI-C3 or PENDI-C3/triPy in chloroform first, and then drop cast the solution on glass, followed by vacuum evaporation for 12 hours at room temperature; (c) Optical images of the damaged and healed PENDI-C3/triPy film after heat treatment under 60 °C for 30 mins.

The straightforward way to modulate the self-healing temperature of PENDI-C3/triPy is to modulate the binding strength between NDI and Py. The free energy of complexation between Py unit and NDI unit in PENDI-C3/triPy was tested in DCM at room temperature as -12.44 kJ/mol. To weaken the binding strength, then we designed and synthesized the second generation PENDI as PENDI-C6 by changing the substituent group R in NDI form propyl group to longer hexyl group (**Figure 3-7a**). A longer substituent group R will increase the molecular mobility of NDI side chain, which decrease its free energy of complexation with Py unit. As shown in **Figure 3-7b**, the grass transition temperature of resulting PENDI-C6 (113 °C) is much lower than that of PENDI-C3 (168 °C), implying higher mobility and weaker interaction of side chain in PENDI-C6 than PENDI-C3. The free energy of complexation between PENDI-C6 and triPy crosslinker (ΔG=-9.43 kJ/mol) is weaker than that between triPy crosslinker and PENDI-C3 (ΔG= -12.44 KJ/mol), implying lower self-healing temperature.

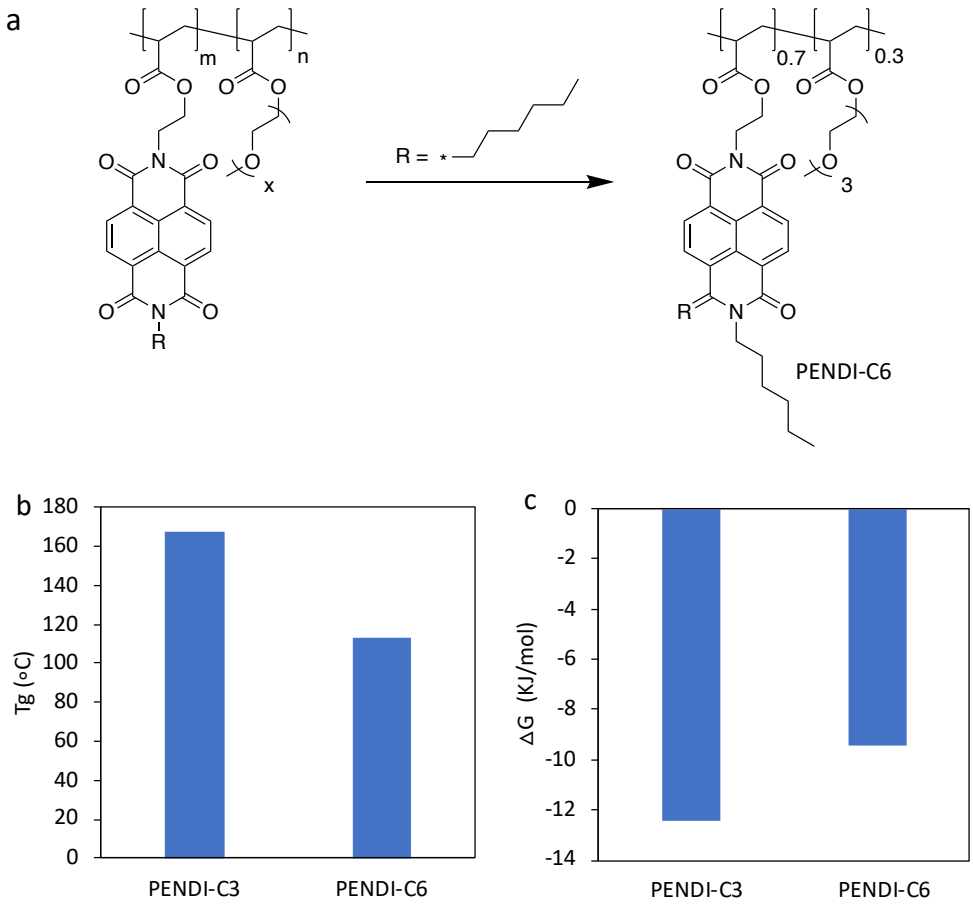

Figure 3-7. Comparisons between second generation PENDI (PENDI-C6) and first generation PENDI (PENDI-C3). (a) Molecular structure of PENDI-C6; (b) Glass transition temperature of PENDI-C6 and PENDI-C3; (c) Free energy of complexation for forming NDI-Py complex in PENDI-C3/triPy and PENDI-C6/triPy. Complexes are dissolved in DCM at room temperature. The molar ratio between NDI unit and Py unit is 1 : 1.

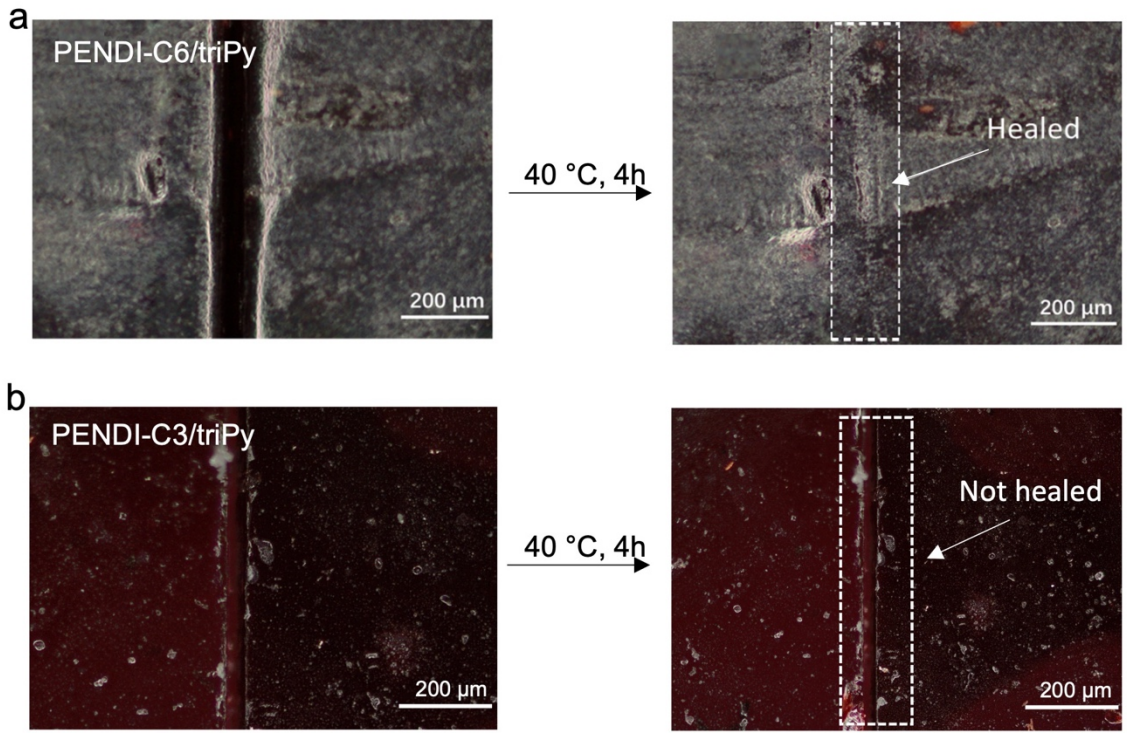

Figure 3-8. Self-healing property experiments of PENDI-C6/triPy (a) and PENDI-C3/triPy (b) under heat treatment at 40 °C.

Solid film consisting of PENDI-C6 and triPy crosslinker (with the molar ratio between NDI and Py units of 1:1) was prepared by drop casting from DCM solution. A self-healing test of the PENDI-C6/triPy film was performed by cutting the film into two pieces, then putting them together and heating for 4 h at 40 °C. Optical microscope images (**Figure 3-8a**) from before and after heating treatment show complete self-healing of the cut. On the contrary, the solid film of PENDI-C3/triPy (same method and ratio, Figure 3-8b) can't heal even after heat treatment for 24h at this temperature. PENDI-C3/triPy film shows the similar healing rate (heal the cut after 4 h) around 60 °C.

Even with optimal mechanical properties, cracking damage may still develop in self-healing polymers, especially over long-term use. Typically, the cracking of polymers originates

from microscale or even nanoscale defects. To mimic this damage, an AFM tip was used to indent the surface of PENDI-C6/triPy and PENDI-C6 films, resulting in two hole-like damage features with diameters of around 500 nm, respectively (**Figure 3-9**). The shape of the damaged area in PENDI-C6 is a triangular cone, similar in shape to the AFM tip. The height profile along the selected black line reveals that both holes have a depth around 60 nm and surrounding bumps with height around 50 nm. Interestingly, the damage hole in PENDI-C6/triPy was much wider and less defined than that in the PENDI-C6 film. Also, there is no distinct bump around the hole in PENDI-C6/triPy. We attribute this difference to the crosslinking effect of triPy. Without triPy, brittle PENDI-C6 dissipates the indentation energy from the AFM tip by both cracking and extrusion of surface, forming a sharp hole and bump. After adding triPy, PENDI-C6/triPy can dissipate the indentation energy by reversibly disrupting the CT interactions instead. The non-covalently crosslinked supramolecular structure allows PENDI-C6/triPy to dissipate energy over a much larger area. Consequently, PENDI-C6/triPy demonstrates higher resistance to crack formation. The height profiles alone the linear area in the films were measured again after heat treatment at 40 ˚C for varying times. The damaged area of PENDI-C6 barely changed even after heat treatment for 6 h, showing no self-healing property. By contrast, after heat treatment only for 2 h, the depth of the hole in PENDI-C6/triPy film decreased from around 50 nm to 20 nm, demonstrating apparent self-healing property. Raising the heat treatment time to 6 h, only a slight trace of the damaged area with a depth of 6 nm was observed. We hypothesize that this self-healing effect of PENDI-C6/triPy film is due to the rebuilding of the CT interactions following breakage.

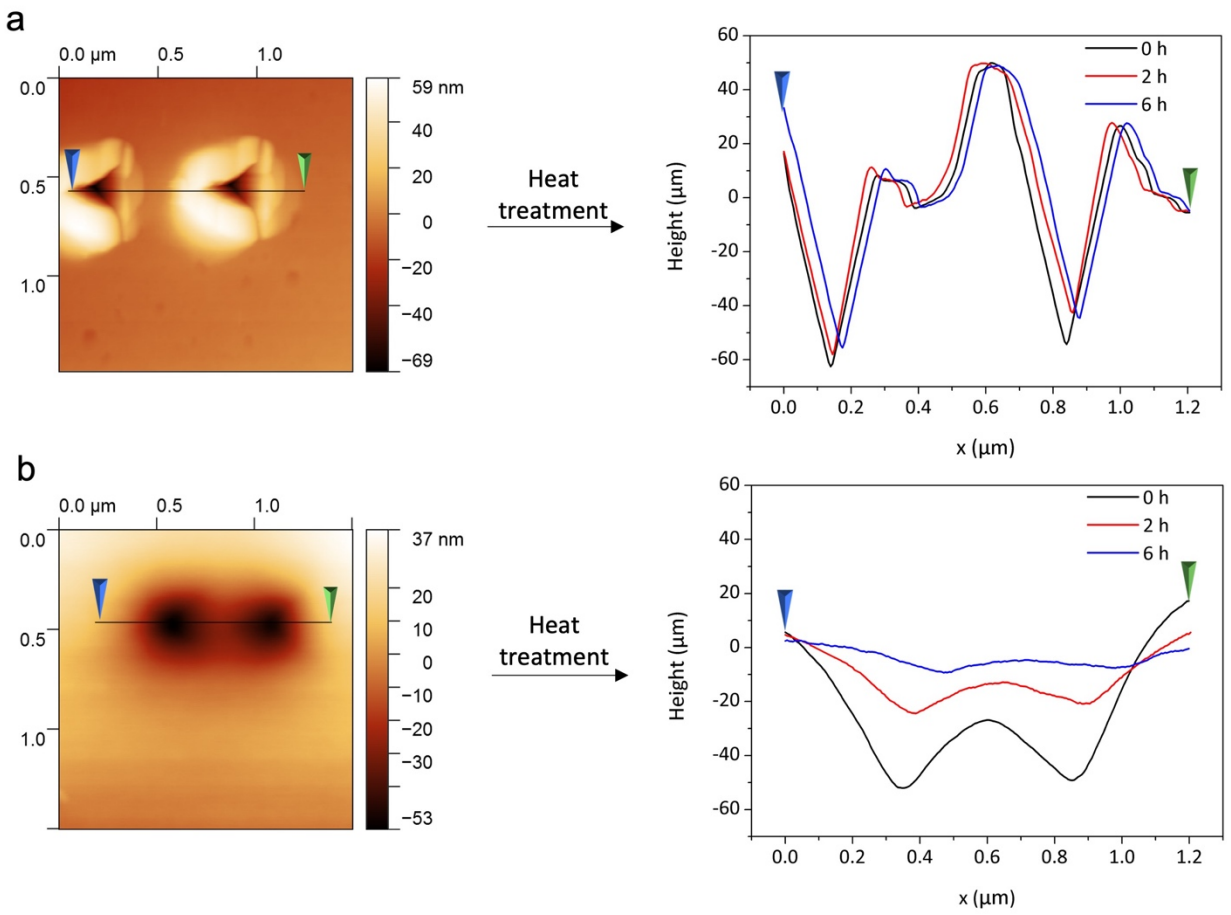

Figure 3-9. AFM height profiles of PENDI-C6 (a) and PENDI-C6/triPy (b) films after being punched by AFM tip followed by heat treatment at 40 °C for different times.

3.3.3 Modulation of Self-healing Properties by Doping Small Molecules

The interaction between NDI and Py functions as the "molecular handle" to module the self-healing property of PENDI/triPy system. As demonstrated so far, we optimized the self-healing temperature by weaking the free energy of complexation. The modulated PENDI endows the system with variable self-healing temperature. However, in this method the development of any new-generation PENDI requires entirely design and synthesis processes, which is quite time-consuming.

Inspired by the different binding models between NDI and Py which can be simply controlled by their molar ratio, we propose a novel strategy to modulate the self-healing property of PENDI/triPy systems. By simply doping small molecules into PENDI/triPy system, the binding strength and crosslinking density of the supramolecular polymer can be determined and modulated. Based on this strategy, three PENDI-C6/triPy (denoted as PP) composites, corresponding to different model compound doping strategies were designed. As depicted in **Figure 3-10a**, PP-1 composite consists of PENDI-C6 and triPy crosslinker with a molar ratio between NDI and Py units of 1:1. Based on our study of molar ratio control in the substituent compounds, the crosslinking mode should be predominantly 1:1 binding complex. To modulate the crosslinking density without changing polymer structure, an additional half molar equivalent of small molecule additive Py was added relative to total NDI side chains present, forming PP-Py composite (**Figure 3-10b**). Then PP-Py composite should possess the 1:1 binding mode almost exclusively, but with a lower crosslinking density than PP-1, as half of the NDI sidechains are tied up in non-crosslinking interactions with free Py molecules. Similarly, by adding half molar equivalent of additive dbNDI relative to total Py units present into PP-1, we created the PP-dbNDI composites (**Figure 3-10c**). Due to the stacking interaction between small molecule dbNDI and Py units, the amount of free NDI side chains will be higher than Py units. The excessive NDI moieties present in this system ensures that the majority of Py units will be bound in the stronger 2:1 mode, without significantly changing the overall density of total crosslinks formed.

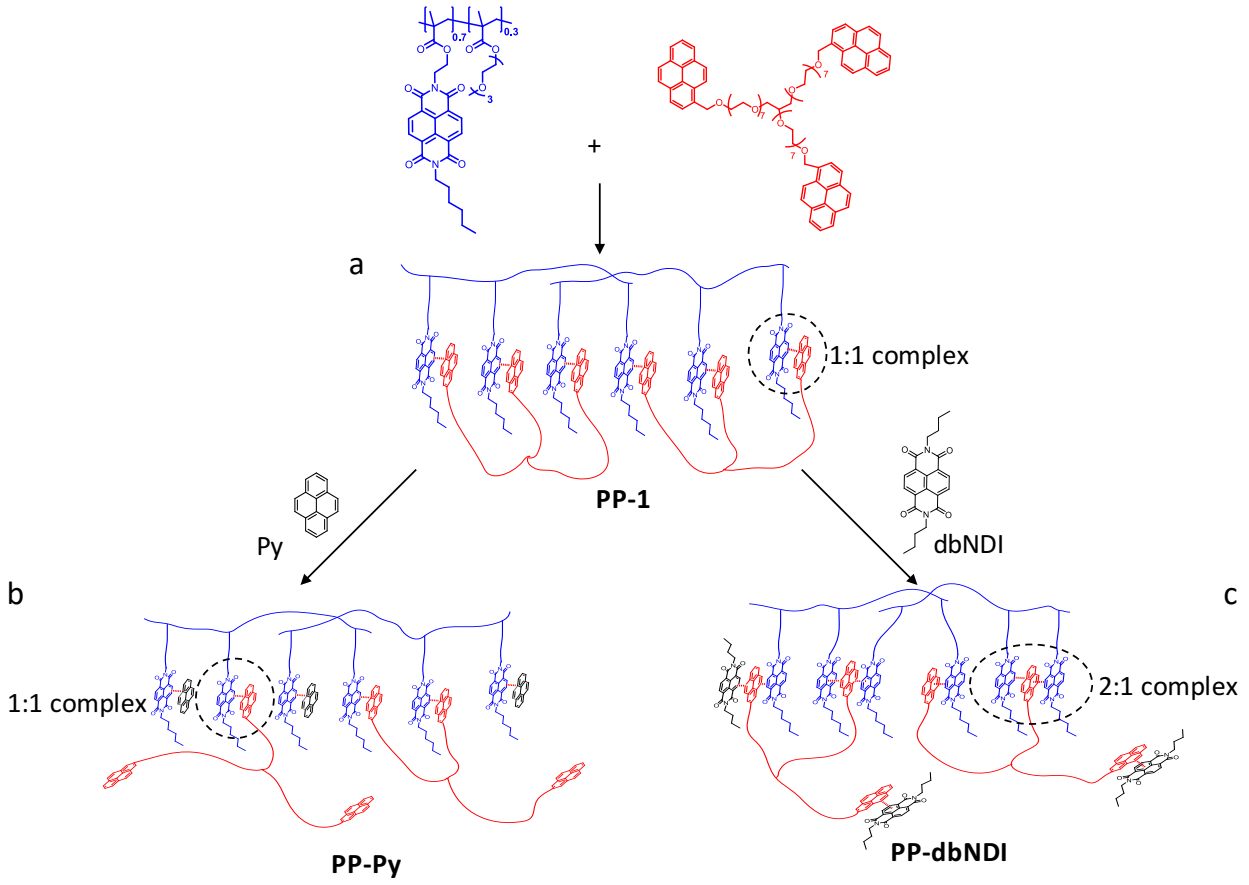

Figure 3-10. Design concept for PP supramolecular polymers and tuning of binding modes. (a) Structural design of PP-1, utilizing triPy to crosslink PENDI-C6 with an equal molar ratio of NDI sidechains and Py units; (b) Structure of PP-Py, with 1:1 complexes favored by occupying half of NDI side chains of PENDI with free Py; (c) Structure of PP-dbNDI, with 2:1 complexes favored by the addition of model compound dbNDI.

The Young's moduli of these polymer composites were first probed *via* AFM to investigate the effect of different binding modes on mechanical properties (**Figure 3-11**). The 3D Young's modulus maps reveal that PP-1 possesses a large average modulus of 92 MPa. We hypothesize that this is because PENDI-C6, with a high glass transition temperature (T_g = 113 °C) and Young's modulus of 104 MPa (**Figure 3-12**), provides a high baseline stiffness owing to its rigid methacrylate backbone. PP-Py possesses a Young's modulus that is slightly lower than PP-1 at 62

MPa. We attribute this to the lower crosslinking density in PP-Py, due to the existence of model compound Py which occupies NDI sidechains. On the other hand, the Young's modulus of PP-dbNDI (241 MPa) is much higher than that of PP-1. This drastic increase can be explained by a shift in predominant interaction mode from the 1:1 complex to the much stronger 2:1 complex. Accordingly, the Young's modulus increases significantly due to the higher energy required to break the CT complex. Notably, all composites exhibit Young's moduli far greater than the majority of self-healing materials in literature (<10 MPa).[138–141] This is because most of the previously reported self-healing polymer designs, including soft gels, elastomers, and even hybrid organic-inorganic composites, typically sacrifice stiffness to achieve self-healing properties. The high stiffness of our design should help maintain the physical integrity of materials which suffer from volume expansion or deformation damage.

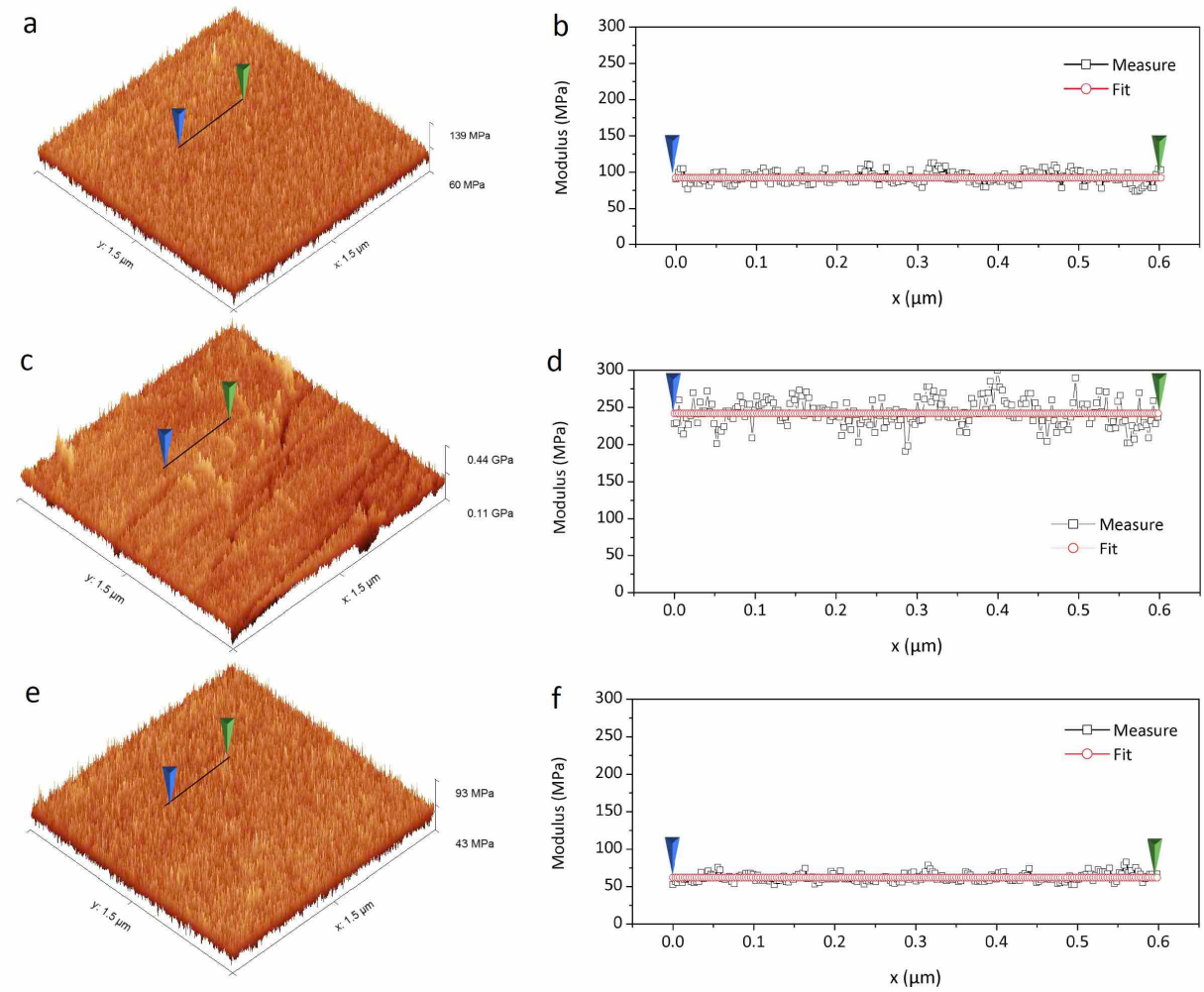

Figure 3-11. 3D Young's modulus maps generated *via* AFM experiments, along with the measured and fitted average (black and red lines, respectively) Young's moduli of selected linear area in PP-1 (a and b), PP-dbNDI (c and d), and PP-Py (e and f).

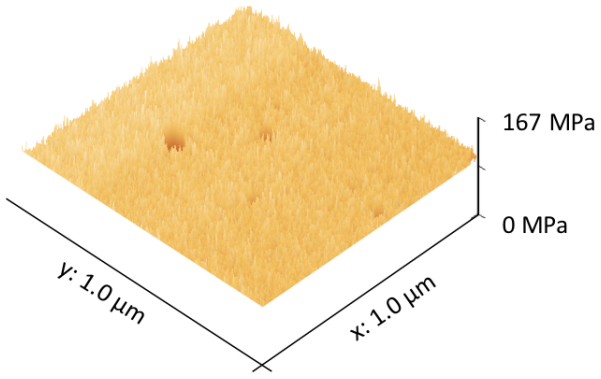

Figure 3-12. 3D AFM Young's modulus map of PENDI-C6.

The mechanical properties of the polymers were further studied by uniaxial tensile experiments. As shown in **Figure 3-13a**, the measured moduli (116 MPa for PP-1, 70 MPa for PP-Py, and 219 MPa for PP-dbNDI) generally agree with the AFM experiment results. Tensile test results also reveal that the PP systems possess high maximum tensile stress (> 2.1 MPa), especially for PP-dbNDI (3.48 MPa). To visually demonstrate this resilience, constant stress of about 1 MPa was applied to a PP-1 film for 1 h at room temperature, resulting in no obvious deformation (**Figure 3-13b**). This high stiffness and high yield point suggest that the polymer is highly resistant to deformation and cracking, which can be helpful to maintain the physical integrity of mechanically active devices.

Additionally, PP polymers possess good stretchability. To demonstrate this, PP-Py was coated on a polydimethylsiloxane (PDMS) substrate. The substrate was then stretched to 100% strain and released ten times, followed by observation under an optical microscope. The optical images show that PP-Py can be stretched by 100% without cracking (**Figure 3-13c**). Wrinkles were, however, observed after releasing PP-Py from stretching, implying that PP-Py shows partially plastic deformation during this process, as would be expected by the prior tensile test results.

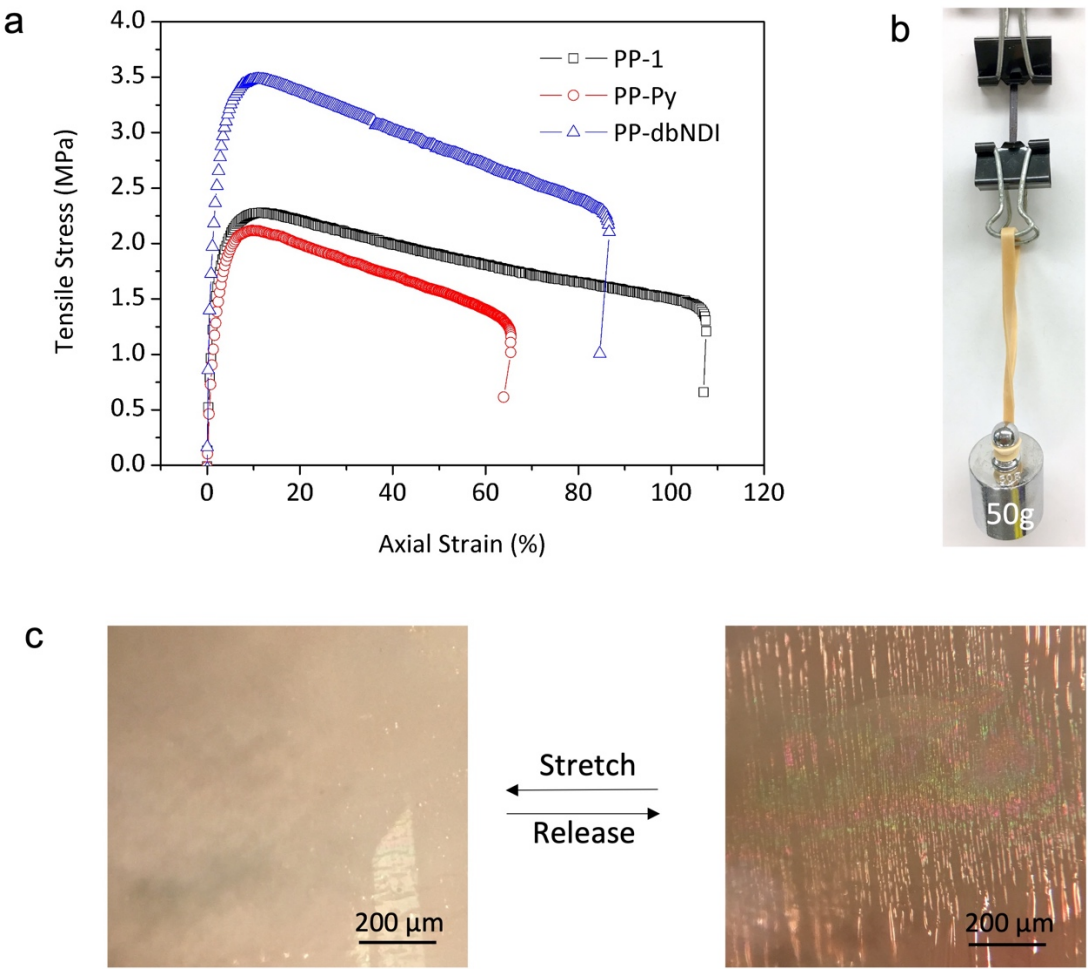

Figure 3-13. Characterization of mechanical properties. (a) Tensile stress-strain curves of PP-1, PP-Py, and PP-dbNDI under a loading rate of 50 mm/min at room temperature. (b) Constant stress experiment of 1 MPa applied to PP-1 film for 1 hour. (c) Stretchability test of PP-Py on PDMS substrate.

To further investigate the effect of different binding modes between NDI and Py groups on self-healing properties, we conducted self-healing tests with bulk polymer films (**Figure 3-1a**). The polymer films were cut into two pieces and then lightly contacted together without additional pressure. These broken films were heat treated at varying temperature for varying time, then observed by optical imaging. As shown in **Figure 3-14**, PP-dbNDI displayed distinct self-healing

properties after heat treatment at 60 °C for 2 h (**Figure 3-14a**). The cut on PP-1, on the other hand, had almost disappeared after healing at 50 °C for 2 h (**Figure 3-14b**). PP-1 was unable to heal at 30 °C, however, even after heat treatment for 24 h (**Figure 3-14c**). PP-Py demonstrated significant healing after heat treatment at 40 °C for 2 h (**Figure 3-14d**) and even at 30 °C for 24 h (**Figure 3-14e**). We attribute the higher self-healing temperature of PP-dbNDI to its stronger binding mode, which requires more thermal energy to break reversible interactions. Although PP-1 and PP-Py possess the same binding mode, the lower self-healing temperature of PP-Py can be explained by its lower crosslinking density.

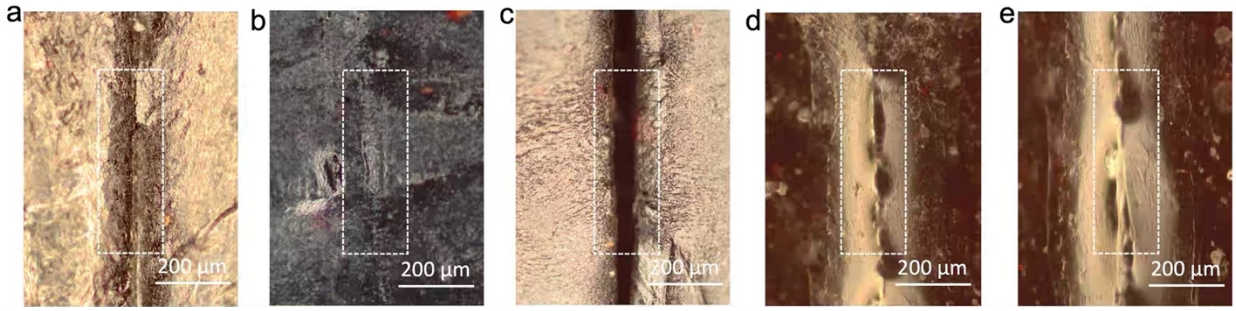

Figure 3-14. Optical images of PP polymer films after cutting and heat treatment. (a) PP-dbNDI after heat treatment at 60 °C for 2 h; (b) PP-1 after heat treatment at 50 °C for 2 h; (c) PP-1 after heat treatment at 30 °C for 24 h; (d) PP-Py after heat treatment at 40 °C for 2 h; (e) PP-Py after heat treatment at 30 °C for 24 h.

Therefore, despite sharing the same polymer components, their sensitivities to temperature are different. Based on this interesting feature, we fabricated a double-layer PP composite thin film by assembling and then pressing PP-Py and PP-dbNDI together (**Figure 3-15a** and **Figure 3-15b**). As shown in **Figure 3-15c**, the double-layer thin film was first bended to the side of PP-dbNDI. Under heat treatment of 60 °C, the bended film gradually became straight and then automatically bended to the opposite side (the side of PP-Py) in 60 s. We attribute this bending shift to the much weaker 1:1 binding mode in PP-Py than that of 2:1 binding mode in PP-dbNDI: after fabricated

by pressing, the polymer chains of the bulk films were stretched, leading to shrinkage stress within the films. Meanwhile, the polymer chains were reversibly crosslinked via pi-pi interactions, which locked the polymer chains and impeded their shrinkage. When the temperature went up to 60 °C, the reversible interactions began to break and rebuild much more quickly, leading to the unlocking and shrinkage of polymer chains. The much quicker shrinkage of PP-Py drives the composite films to bending to its side.

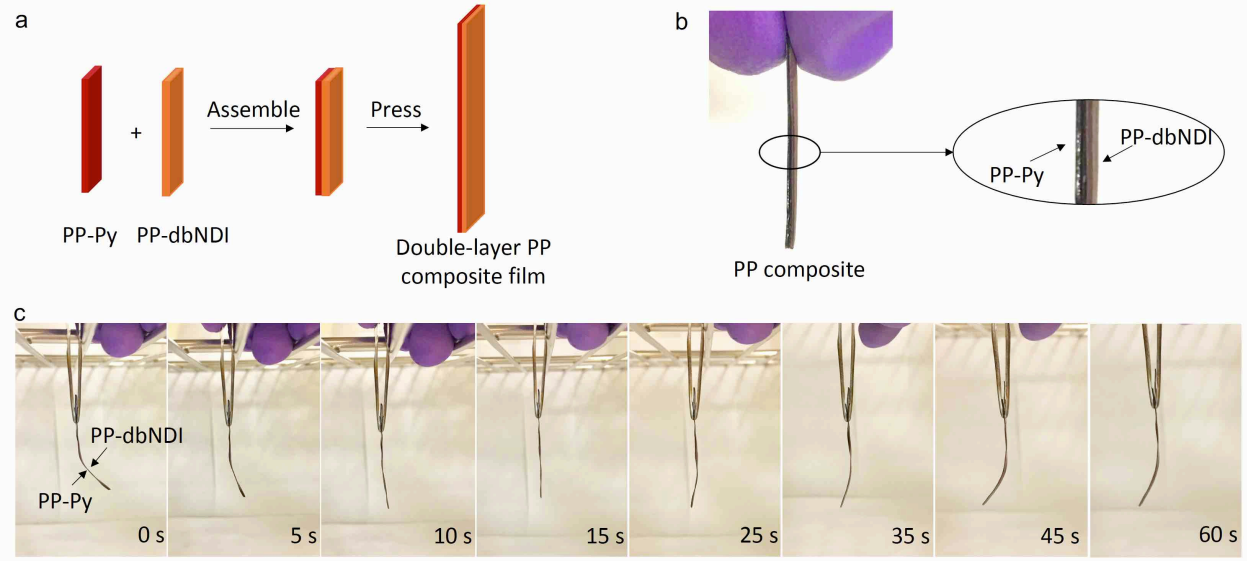

Figure 3-15. (a) Schematic representation of the fabrication of double-layer PP composite film; (b) Optical images of the PP-Py/PP-dbNDI double-layer composite film; (c) The bending shift process of PP-Py/PP-dbNDI double-layer composite film under 60 °C within 60 s.

Uniaxial tensile tests were further conducted after cutting and healing the films to quantitatively investigate the self-healing efficiency of PP-1, PP-dbNDI, and PP-Py at different temperatures of 40, 50, and 60 °C (**Figure 3-16a, b, c**). The self-healing efficiency was estimated by the recovery of maximum tensile stress. As shown in **Figure 3-15d**, even after heat treatment at 40 °C, all samples show self-healing efficiencies higher than 55%. Due to its weaker binding strength and lower crosslinking density, PP-Py possesses highest self-healing efficiency, which is

higher than 85% even after heat treatment at 40 °C. **Figure 3-16e** reveals that all healed films still possess high Young's moduli (> 60 MPa), which helps increase the durability and lifetime of materials. Note that since films were healed from a fully broken state with no added pressure, air bubbles or inhomogeneous thicknesses may well have negatively impacted these results. Compared with previous reports (shown in **Figure 3-17**), the polymer systems reported here not only possess very high Young's moduli (63-250 MPa), but also self-heal at relatively low temperatures (30-60 °C). Such a combination not only makes these materials suitable for devices in high-stress applications, but also allows these devices to enjoy self-healing benefits under mild thermal conditions.

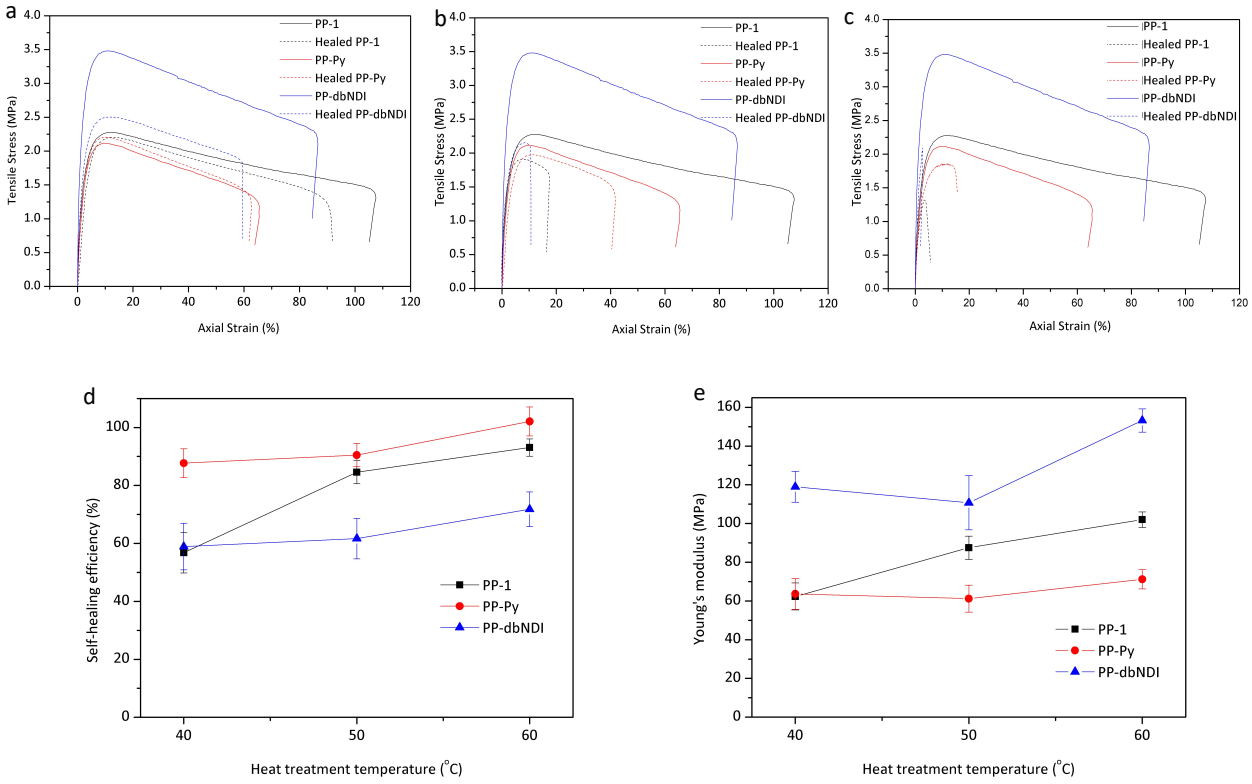

Figure 3-16. The self-healing property tests of PP polymer films. Stress-strain tests prior to damage (solid line) and after healing (dotted line) by heat treatment for 12 hours at different temperature: (a) 60 °C, (b) 50 °C, (c) 40 °C. Self-healing efficiency tests (d) and Young's moduli

recovery (e) of PP polymer films after cutting and heat treatment at different temperature for 12 hours, respectively.

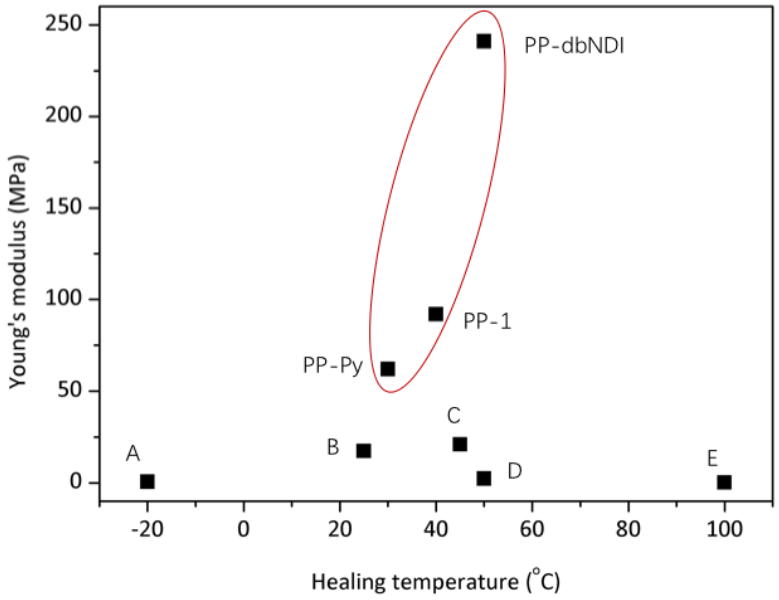

Figure 3-17. Comparison between our design and previous studies (A,[142] B,[142] C,[122] D,[110] E[143]).

3.3.4 Possible Applications

Keeping high and stable conductivities for ion and electron is crucial for electrodes in energy storages devices. Besides self-healing and mechanical properties, we further investigate the Li ion conductivity and compatibility with conductive carbon of our polymer system. First, our polymers exhibit the ability to solvate and transport ions as a solid electrolyte, due to the prevalence of oligo(ethylene oxide) moieties in both PENDI and triPy. To demonstrate this, PP-1 supramolecular polymer was doped with salt LiTFSI and solvate ionic liquid (SIL), respectively. After doped with LiTFSI in a 20:1 [EO]:[Li^+] molar ratio, the resulting material PP-1/LiTFSI was sandwiched between stainless steel discs, followed by electrochemical impedance spectroscopy (**Figure 3-18a**). Curve fitting the resulting Nyquist plot to a standard model for ion-conductive

solids reveals the polymer system to have an ionic conductivity >10^{-6} S/cm at 50°C, showcasing the application potential of this material as an electrode binder or solid-state electrolyte in batteries. Once cracking damage occurs, ionic conductivity in a solid electrolyte will decrease dramatically due to the disconnection of conductive pathways. We demonstrated this effect by sandwiching two individual PP-1 films between stainless steel discs for an ionic conductivity test. As shown in **Figure 3-18c**, due to the existence of a physical gap between the films, the measured ionic conductivity of the stack is only about 16% that of a continuous film of PP-1. However, upon heating at 50 °C for 12 h, the physical disconnection was completely healed, resulting in 100% recovery of ionic conductivity. The Young's modulus increases to 132 MPa due to the interaction between Li ion and [EO] units. In order to improve the ionic conductivity further, PP-1 was doped with SIL Li(G4)TFSI. Due to their good compatibility, high doping amount of SIL was applied (33 wt.%). The resulting PP-1/Li(G4)TFSI exhibits high ionic conductivity of 1.01×10^{-5} S/cm even at room temperature, and reasonable Young's modulus (8 MPa).

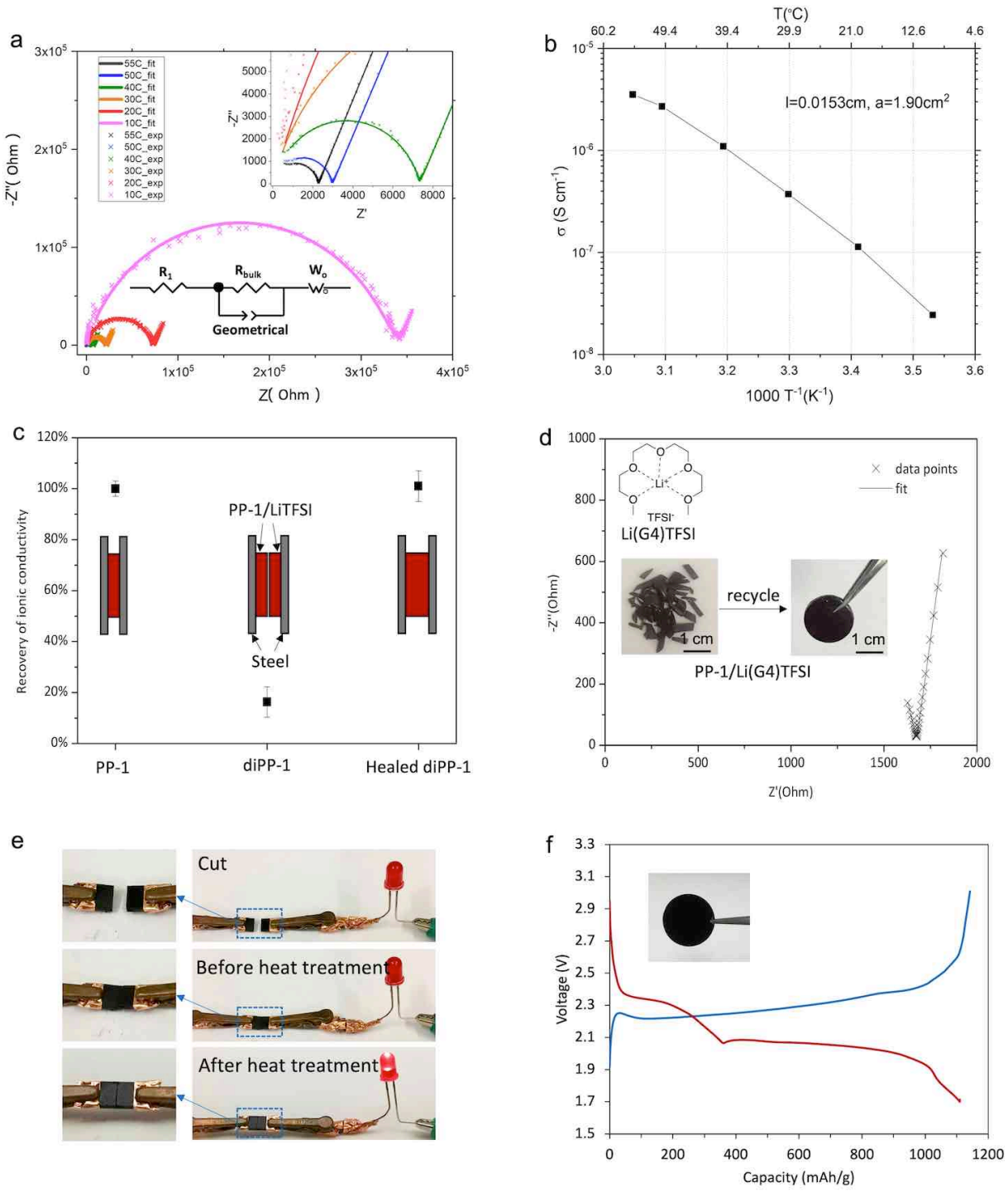

Figure 3-18. (a) Nyquist plots and curve fits at different temperatures in electrochemical impedance spectroscopy tests of PP-1/LiTFSI. The inserted figure indicates the equivalent circuit to fit the plots: R_1 represents the entire internal resistance; R_{bulk} represents the bulk resistance of

electrolyte; Geometrical represents the geometrical capacitance due to the presence of electrolyte with a finite dielectric constant between the two parallel metallic electrodes; W_o represents the resistance against the Warburg diffusion process of Li ion.[3,61] (b) Ionic conductivity of PP-1/LiTFSI at different temperatures. (c) Self-healing recovery test of PP-1/LiTFSI based on ionic conductivity. (d) Nyquist plots and curve fit of PP-1/Li(G4)TFSI at room temperature and recovery of PP-1/Li(G4)TFSI under 40 °C for 12 h (inside). (e) Recovery of composite film as electron conductive pathway in circuit. (f) Discharge/charge voltage profiles at 0.2C rate of sulfur cathode by using PP-1 as binder (sulfur loading = 0.9 mg/cm^{-2}).

Besides, the polymer system possesses good compatibility with carbon and could function as cathode binder in lithium-sulfur battery. We made a freestanding composite film by uniformly dispersing sulfur/MJ430 mesoporous carbon composite (65 wt.%) and carbon black (5 wt.%) in PP-1 film (30 wt.%). Due to the high content of carbon, the resulting film demonstrated high electron conductivity by lighting light-emitting diode (LED) in the electrical circuit (**Figure 3-18e**). The circuit was broken after we cut the composite film and even contacted the two pieces together. However, the LED could illuminate again after heating the broken composite film. This test not only implies the function of PP-1 as effective binder to integrate particles together, but also its self-healing property to recovery the electron conductive pathway. To investigate its effect in real cell, we made the sulfur cathode by dissolving the composite film into N-methyl-2-pyrrolidone and then casting on aluminum foil, followed by solvent evaporation. Consequently, a robust sulfur cathode was made and cycled at C/5 with lithium metal as anode. As shown in **Figure 3-18f**, the cathode exhibits a high initial discharge capacity of 1109 mAh/g, with two typical discharge voltage plateaus at 2.30 V and 2.06 V, respectively. This result shows promise for its use in future electrochemical devices.

To improve the processability and Li ion conductivity of PENDI, we designed PENDI-350 as the third generation PENDI by extending the length of OEG in PENDI-C6 from 3 unit to 7 unit. Compared with PENDI-C6 (**Table 3-2**), PENDI-350 possesses lower self-healing temperature, higher maximum tensile strain. The Li ion conductivity is improved around 2.4 times from 1.08×10^{-4} mS/cm to 2.57×10^{-4} mS/cm. As shown in **Figure 3-19**, the third generation of PENDI (PENDI-350) will be used to form supramolecular network with triPy crosslinker as binder in next chapter for fabricating high-loading, long-cycle-life sulfur cathode.

Table 3-2. Property comparison between PENDI-C6/triPy and PENDI-350/triPy

PP polymers	Maximum tensile strain	Self-healing temperature	Ionic conductivity	Young's modulus
PENDI-C6/triPy	108%	40 °C	1.08×10^{-4} mS/cm	116 MPa
PENDI-350/triPy	185%	30 °C	2.57×10^{-4} mS/cm	29.2 MPa

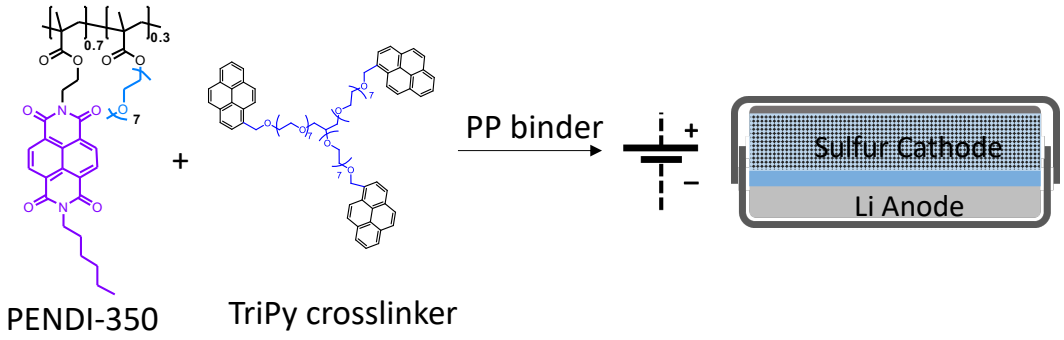

Figure 3-19. Coin cell by using PP as binder for S cathode.

The good ionic conductivity and compatibility with carbon make our PENDI/triPy system promising candidates for applications in areas including artificial skins, sensors, *et al*. Most importantly, the tunable self-healing temperature and mechanical property not only extend its

application potential to a much wider range, but also endows the system with fundamental solution to solve the cracking problem in these applications.

3.4 CONCLUSIONS

In summary, I designed a supramolecular network structure, consisting of PENDI and triPy crosslinker based on reversible pi-pi interactions between electron-deficient NDI and electron-rich Py functionalities. With sophisticated design of its molecular structure, PENDI possesses tunable "molecular handles" for both self-healing property and mechanical properties. Three generations of PENDI are designed to achieve the optimal self-healing temperature of 30 °C and Li ion conductivity of 2.57×10^{-4} mS/cm at room temperature for resulting PENDI/triPy system. Besides, we present an effective and feasible strategy to engineer the self-healing and mechanical properties of supramolecular polymers for diverse applications without requiring synthesis of new covalent structures.

The resulting composites exhibit remarkable features: (1) high stiffness and good toughness to help maintain physical integrity in devices; (2) widely tunable self-healing temperature and mechanical properties to satisfy various application requirements; (3) good ionic conductivity and high self-healing efficiency to provide durable ion-conductive pathways in potential electrochemical applications, especially the energy storage area. Moreover, our strategy to decouple crosslinking properties from the polymer structure is generally applicable, and we hope it will inspire further engineering of improved supramolecular systems for effective integration of self-healing behavior into real devices.

CHAPTER 4: FABRIACTION OF HIGH-SULFUR-LOADING, LONG-CYCLE-LIFE SULFUR CATHODE FOR LITHIUM-SULFUR BATTERY

4.1 INTRODUCTION

4.1.1 Motivation

To achieve practically viable Li-S batteries, a high-loading sulfur cathode is essential.[25] Based on the estimation from Wang *et al*., an areal capacity ≥ 4.0 mAg/cm^2 is needed for Li-S batteries to be comparable to commercial Li-ion batteries.[44]

Sulfur cathode possesses outstanding theoretical gravimetric specific capacity which is around 10 times higher than that of cathodes in Li-ion batteries. As discussed in previous Chapters, however, the practical application of sulfur cathode is impeded by several challenges including: (1) dissolution of LiPSs in bulk organic electrolyte, (2) volume expansion problem of transforming elemental S_8 to Li_2S during discharge process, (3) insulating nature of S_8 and Li_2S_2/Li_2S, *etc*. With increasing sulfur loading in cathode and larger cathode area, these problems will become more significant.

Besides the volume change between S_8 and Li_2S during charge and discharge, there are several other reasons making the high-loading sulfur cathode prone to cracks, especially during the fabrication processes of sulfur cathode. First, sulfur cathode film is made based on slurry casting method. The sulfur cathode film will suffer from the volume shrinkage stress when evaporating slurry solvent to dry the cathode film under heat treatment (50 °C). Second, the huge compression force during cell assembly and packing process also easily causes structural damage

to sulfur cathode, especially when making sulfur cathode with larger area. Third, the repeating dissolution and deposition of LiPSs will change the structure and morphology of cathode which leads to additional tension stress in the cathode. With increasing the sulfur loading of cathode, the shuttle effect will be more significant since the dissolved LiPSs that crossover the bulk electrolyte will be multiplied.

Different strategies have been developed to achieve high-loading sulfur cathode, including porous sulfur hosting matrixes design, cathode structure design, functional binders design, *etc*. As reviewed in **Section 1.4.1** Design of Sulfur Matrix, the physical confinements based on sulfur matrixes not only confine LiPSs within porous structures, but also help mitigate the tension stress to a certain degree. For example, the well-designed core-shell[144,145] or yolk-shell[146] structures have been proven to accommodate the volume expansion of sulfur efficiently. However, the design of sulfur matrixes is mainly relied on nanomaterials, which normally have low packing density, consequently, decreasing the volumetric energy density of the cathode and cell.[147] As an indispensable component in sulfur cathode (**Table 4-1**), binder is designed to glue particles together, including sulfur particles, sulfur matrix particles, and conductive additives, *etc*. After increasing sulfur loading, the number of particle-to-particle junctions in sulfur cathode will increase, making the role of binder more crucial. At the particle level, an ideal binder needs to not only mechanically stabilize the whole architecture of sulfur cathode, but also chemically suppress the loss of LiPSs.

Table 4-1. Desirable functions of binder used to fabricate high-loading sulfur cathode.[148]

	At particle level
Functions	a. Glue sulfur hosts with conductive additives

	b. Confine LiPSs to suppress their dissolution in electrolyte
	c. Withstand the tension stress during volume change
Properties	a. Suitable binding to both LiPSs and sulfur hosts
	b. Short-range flexibility to withstand volume change

4.1.2 Rational and Overview

Herein I report the fabrication of high-loading sulfur cathode with PENDI-based binder. Chapter 2 demonstrates the outstanding LiPSs confining ability of PENDI to improve the cycle life of sulfur cathode with low sulfur loading (< 2 mg/cm^2), which chemically stabilizes LiPSs. To mechanically stabilize the sulfur cathode with high loading, I first improve the toughness of PENDI binder by adding triPy crosslinker to form the supramolecular network binder PENDI/triPy based on pi-pi interactions. To improve the mechanical properties of binder further, PVDF is added to enhance both the stiffness and toughness of resulting binder PENDI/triPy/PVDF. As shown in **Figure 4-1**, the fabrication of high-loading, long-cycle-life sulfur cathode consists of two steps based on the fabricated cathode in Chapter 2: First, a high-loading sulfur cathode to achieve areal capacity > 4 mAh/cm^2 is fabricated by increasing the thickness of sulfur cathode with PENDI/triPy binder. Second, a cathode with initial discharge capacity > 10 mAh is achieve by increasing the diameter of sulfur cathode with PENDI/triPy/PVDF binder.

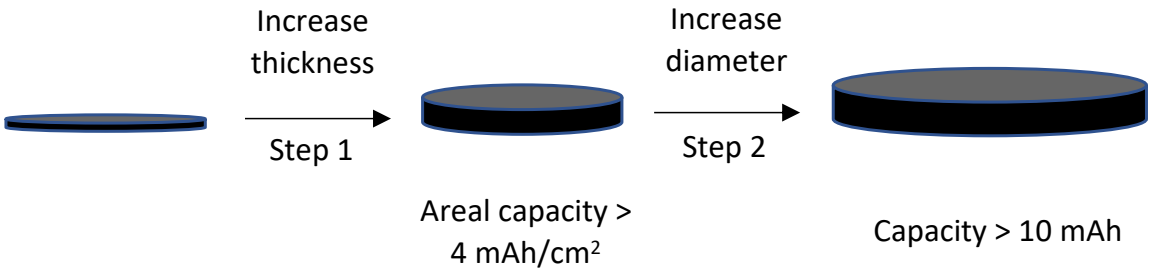

Figure 4-1. Fabrication of high-loading, long-cycle-life sulfur cathode by gradually improving the thickness and diameter of sulfur cathode with tough and stiff binders.

4.2 EXPERIMENTAL SECTION

4.2.1 Materials

Mesoporous carbon MJ430 (Porous Carbon CNovel™; Toyo Tanso USA, Inc.) was washed with 2 M HCl in ethanol for purification. Anhydrous 1,3-dioxolane (DOL, 99.8%, Aldrich), anhydrous 1,2-dimethoxythane (DME, 99.8%, Aldrich) were dried with 4Å molecular sieves and then stored in an argon-filled glovebox (Vacuum Technology Inc, <0.01ppm H_2O and O_2) before use. Lithium bis-(trifluoromethanesulfonyl)imide (LiTFSI) and $LiNO_3$ were purchased from 3M and dried at 120°C under argon, then stored/used in an argon-filled glovebox. Lithium chips (99.9%, 15.6mm diameter, 0.45 mm thickness) and other cases used for coin cell assembly (including o-ring, spring, spacer, caps) were purchased from MTI Corp and stored/used in an argon atmosphere glove box. All other chemicals and reagents were purchased from Aldrich.

4.2.2 Carbon Modification

To improve its affinity with sulfur, MJ430 is modified with thiol functional group based on previous report, following the reaction procedure in **Figure 4-2**.[69] Washed MJ430 carbon was mixed with 20 mol% 4-aminophenylthiol in THF and sonicated for 20 mins. The mixture was placed in an ice bath, followed by adding equivalent molar of isoamylnitrite and doubled molar of HCl to initiate in situ diazotization, which releases N_2 gas bobble. Then the mixture was heated at 70 °C and stirred vigorously for 12 hours. The final reaction mixture was washed four times by

using ethanol : ammonium hydroxide mixture (v/v = 2:1), THF, DI water, and acetone, respectively. Washed carbon then was dried under vacuum at 90 °C overnight.

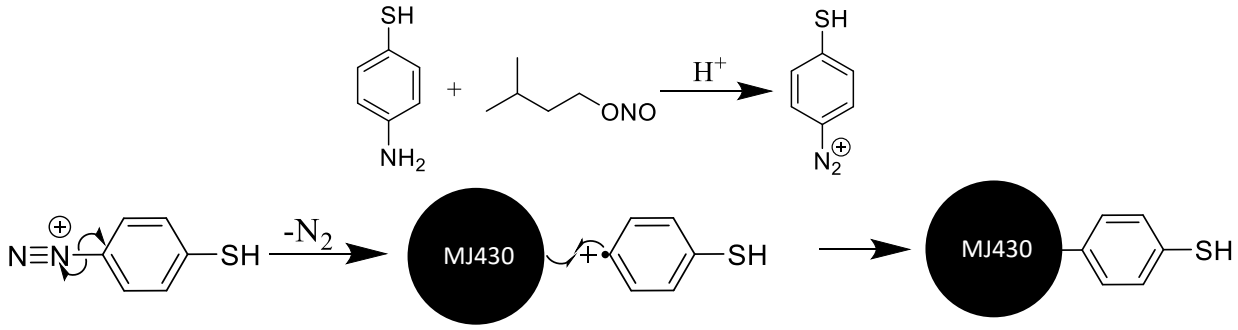

Figure 4-2. Surface modification of MJ430 with thiol functional group.

4.2.3 Fabrication of Sulfur Cathode

The fabrication of sulfur cathode follows the same procedure as **Section 2.2.7** except that the binders used in this section are based on PENDI, PENDI/triPy, PENDI/triPy/PVDF. PENDI used in this chapter is the third generation PENDI (PEDNI-350).

4.2.4 Assembly of Lithium-Sulfur Coin Cell

The assembly of lithium-sulfur coin cell in this section is the same as **Section 2.2.8**.

4.2.5 Uniaxial Tensile Measurements

The mechanical properties of binders were measured based on the uniaxial tensile measurements at room temperature with a loading rate of 50 mm/min, following the same procedure in **Section 3.2.9**. The Young's modulus, maximum stress, maximum strain, toughness, *etc*. of the binders were calculated and obtained based on the resulting stress-strain curves from the uniaxial tensile measurements.

4.3 RESULTS AND DISCUSSION

4.3.1 Sulfur Cathode with PENDI Binder

Chapter 2 has demonstrated the outstanding LiPSs confining ability of PENDI as binder in sulfur cathode with low sulfur loading (1 mg/cm^2). Here we further investigate the fabrication of sulfur cathode with PENDI binder at higher sulfur loading (>2 mg/cm^2) by gradually improving the sulfur loading from 1.0 to 2.1 and then 3.8 mg/cm^2. The resulting cathodes deliver initial discharge capacities of 1189, 1098, 1052 mAh/g at 0.1 C rate (**Figure 4-3**), respectively. Despite the slight change in discharge capacity, their discharge/charge voltage profiles keep almost the same trend: two discharge plateaus at 2.3 and 2.1 V are observed, which refer to the phase-conversion reaction from solid elemental S_8 to soluble long-chain LiPSs and then to solid short-chain LiPSs, respectively. The characteristic over-potential peaks at the beginning of the charge voltage profiles, referring to the two-phase reaction of converting solid Li_2S into liquid LiPSs, are also observed.

Despite increasing sulfur loading to 3.8 mg/cm^2, the polarization ΔE (0.26 V, **Figure 4-3**) of cathode with PENDI binder is lower than that of cathode with PVDF binder (0.32 V, **Figure 4-4**). The lower ΔE of PENDI cathode could benefit from its stronger electrolyte affinity. As shown in **Figure 4-5a**, the electrolyte affinities of different binders are evaluated based on the solvent evaporation rate of DOL/DME based electrolyte after mixing with binders.[52] PEO is also used as reference due to its well-known strong affinity with DOL/DME electrolyte, showing the slowest solvent evaporation rate in **Figure 4-5a**. PENDI shows a much lower evaporation rate than PVDF. Besides, the final weight of PENDI is close to that of PEO, and about 10% higher than that of PVDF after 60 mins, which demonstrates much stronger affinity to electrolyte than PVDF. The

electrochemical impedance spectroscopy (**Figure 4-5b**) shows that PENDI possesses good Li ion conductivity of 1.4×10^{-2} mS/cm at room temperature, which reaches the same order of magnitude as amorphous PEO. On the contrary, the Li ion conductivity of PVDF is 3.2×10^{-3} mS/cm, which is one order of magnitude lower than that of PENDI.[149]

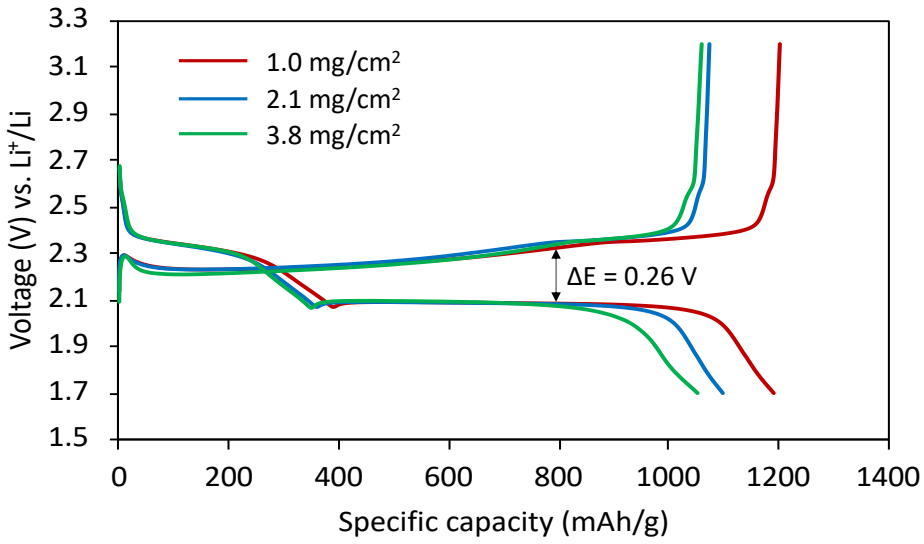

Figure 4-3. The discharge/charge voltage profiles of PENDI cathodes with different sulfur loading (1.0 to 2.1 and then 3.8 mg/cm^2) at 0.1C rate.

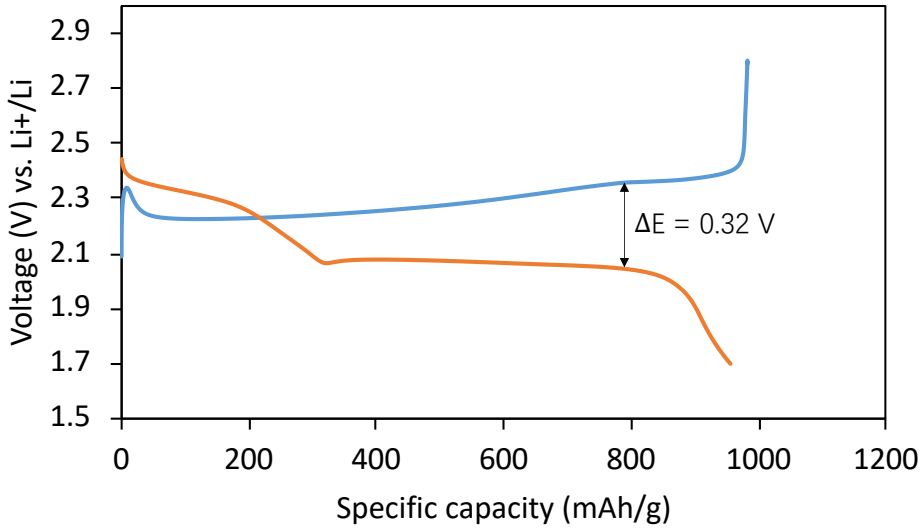

Figure 4-4. The discharge/charge voltage profile of PVDF cathode with sulfur loading of 3.4 mg/cm^2 at 0.1C rate.

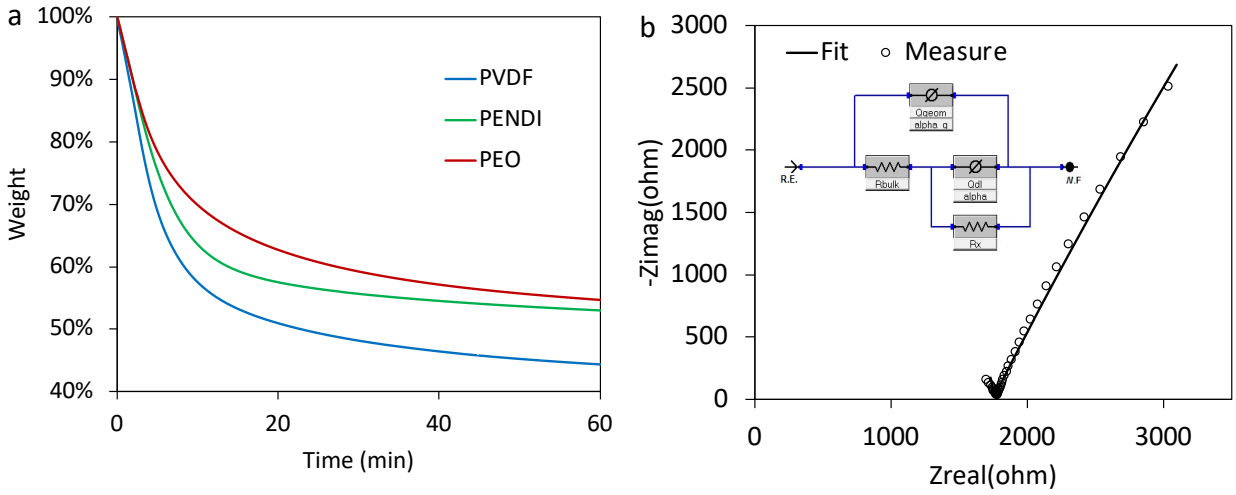

Figure 4-5. (a) Plot to show differences in evaporation rate of electrolyte using different polymeric binders under room temperature; (b) Nyquist plot and curve fitting in electrochemical impedance spectroscopy of PENDI.

Despite the successful fabrication of high-loading (sulfur loading > 2 mg/cm^2) cathodes with PENDI binder, the cycling stabilities of the cathodes are not ideal showing notable cracks. As shown in **Figure 4-6a**, although sulfur cathode with PENDI binder demonstrates decent retention in discharge capacity (77%) and high coulombic efficiency (> 97%), the cathode fails suddenly after 58 cycles. I attribute the failure of the cathode to its mechanical damage due to two reasons: First, significant shuttle effect is not observed. The high coulombic efficiency (> 97%) at 58th cycle demonstrates good cycling stability. Meanwhile, the discharge/charge voltage profiles at 5th and 50th cycles show clear overpotentials at the beginning of charge profiles (**Figure 4-6b**). This universal characteristic overpotential peak was referred to the two-phase reaction of converting solid Li_2S into liquid LiPSs.[94] This extra driving force is needed to nucleate the new

phase (soluble LiPSs). Therefore, due to the lack of soluble LiPSs, extra free energy is still needed at the beginning of charge even after 50 cycles. Second, SEM images (**Figure 4-7a)** shows that cracks with width of 10-20 μm are uniformly distributed in the cathode (sulfur loading = 3.8 mg/cm^2) due to the failure in resisting volume expansion stress. We attribute this to the smaller molecular structure and higher glass transition temperature (69 °C, **Figure 4-7b**) of PENDI compared with commonly used binders, such as PVDF and PEO. Therefore, I speculate that the loss of conductive pathway due to cracking leads to the failure of cell cycling.

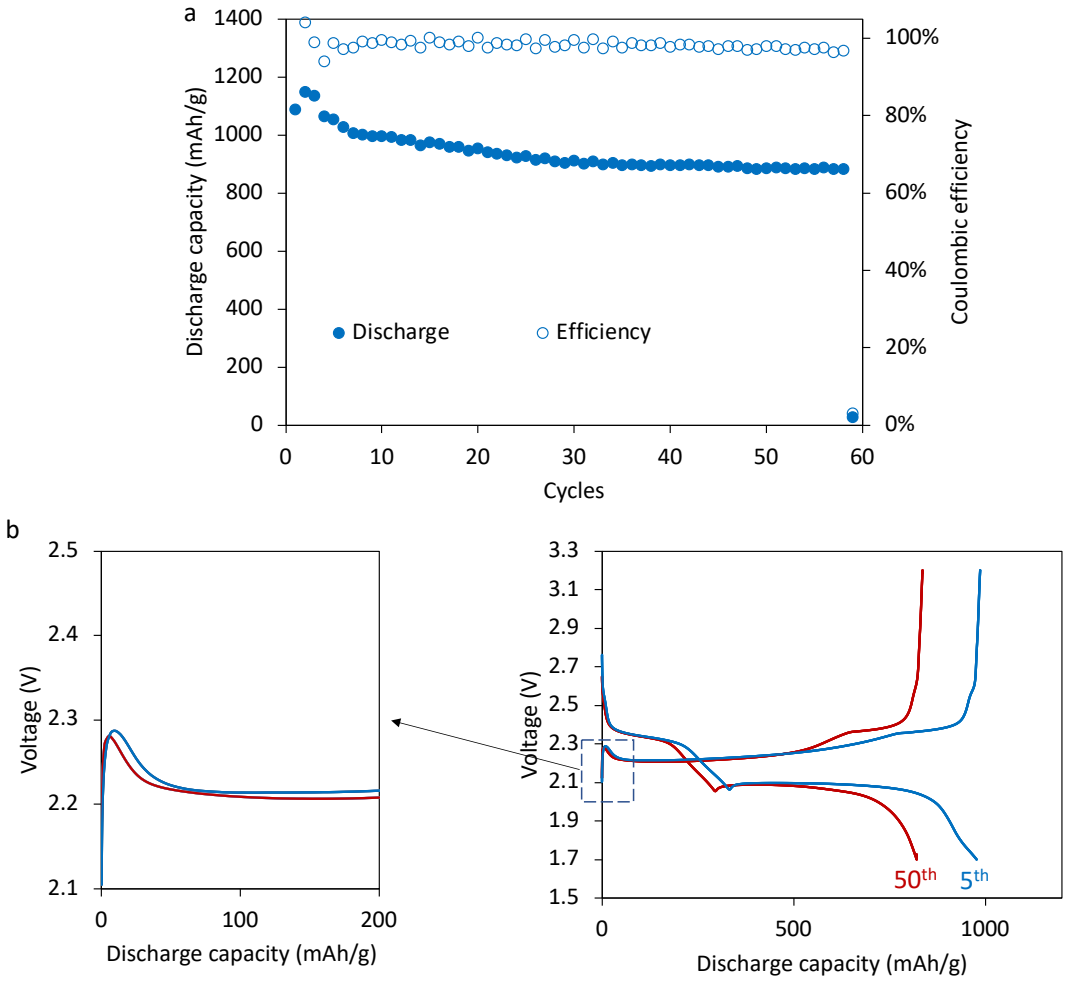

Figure 4-6. (a) Cell performances of cathode with PENDI as binder (sulfur loading = 2.1 mg/cm^2) at 0.1C rate; (b) The discharge/charge voltage profiles at 5th and 50th cycles of the cathode in (a).

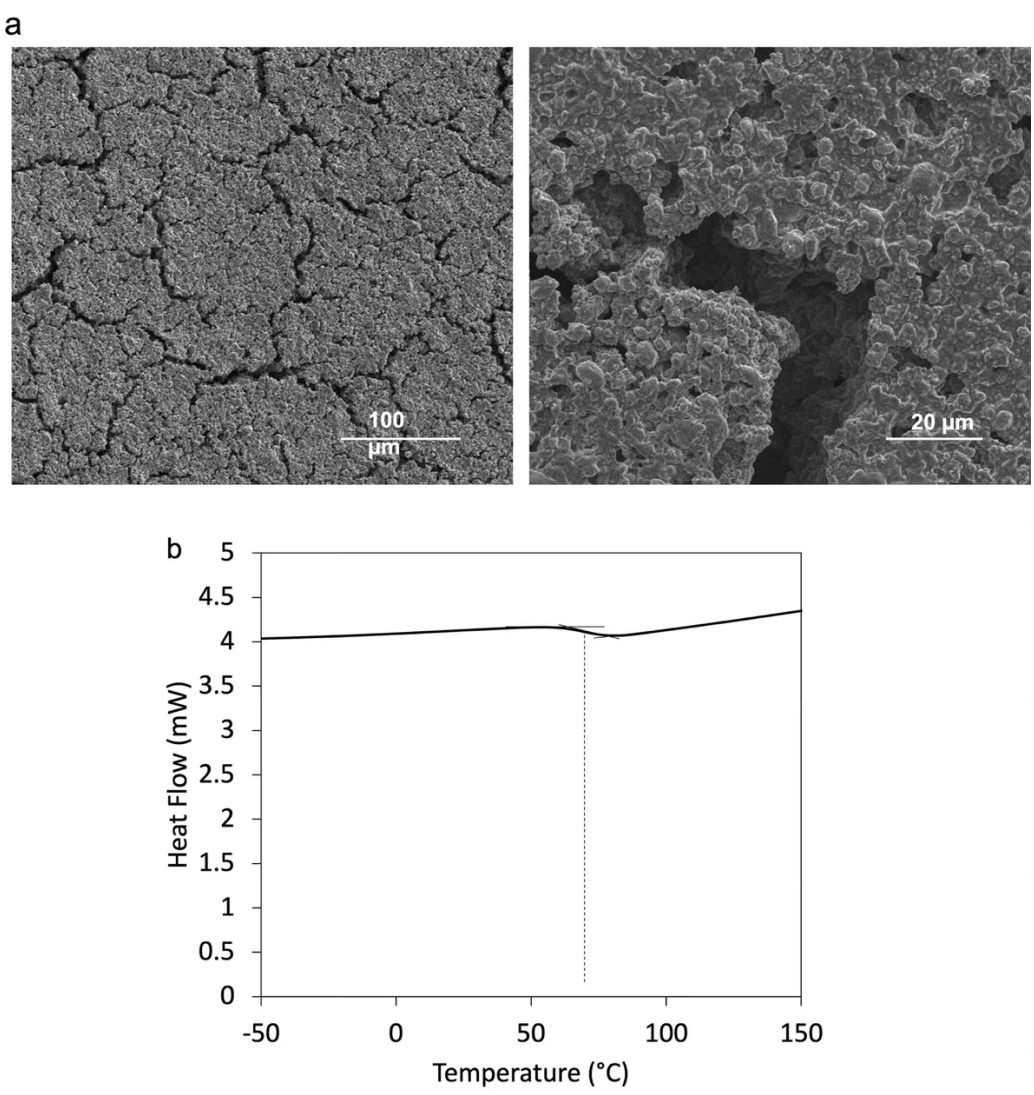

Figure 4-7. (a) Scanning electron microscope images of PENDI cathodes; (b) DSC test of PENDI with heating rate of 10 °C/min.

4.3.2 High-Area-Capacity Sulfur Cathode with PENDI/triPy Binder

As discussed in Chapter 3, the reversible interaction between Py and NDI units enables the formation of a supramolecular network PENDI/triPy (PP). To improve the toughness of PENDI binder for mitigating cracks, I added triPy crosslinker to form the PENDI/triPy binder. The reversible interaction between NDI and Py dissipates energy to enhance the mechanical integrity

of sulfur cathode. To optimize the cathode performance, I investigated the effect of different triPy:PENDI ratio (based on the molecular ratio between NDI unit and Py unit) on cathode cycling performance by keeping the weight of PENDI/triPy constant. Different triPy:PENDI ratios, including 1:6, 1:3, 1:1, are used. The corresponding cathodes are denoted as PP-6, PP-3, PP-1. As shown in **Figure 4-8**, the discharge capacity retentions of PP-1 (86%, sulfur loading = 2.5 mg/cm^2, **Figure 4-8a**) and PP-3 (88%, sulfur loading = 2.5 mg/cm^2, **Figure 4-8b**) are much higher than that of PP-6 (75%, sulfur loading = 2.3 mg/cm^2, **Figure 4-8c**) and pure PENDI (77%, sulfur loading = 2.0 mg/cm^2, **Figure 4-6a**). We attribute this to the higher ratio of triPy in PP-1 and PP-3, resulting in better mechanical properties.

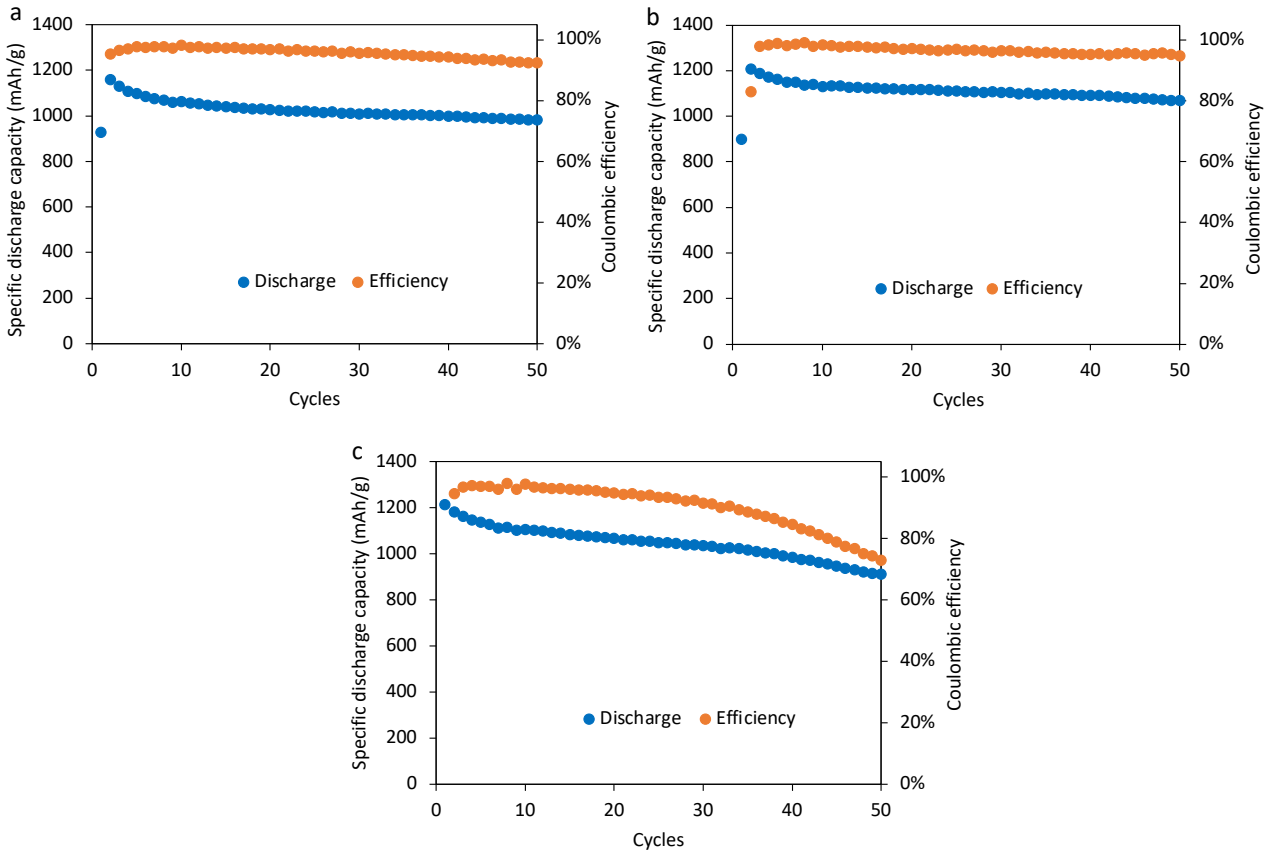

Figure 4-8. Cell performaces of cathodes with binders of (a) PP-1 (sulfur loading = 2.5 mg/cm^2), (b) PP-3 (sulfur loading = 2.5 mg/cm^2), and (c) PP-6 (sulfur loading = 2.3 mg/cm^2) at 0.1C rate.

As shown in **Figure 4-9**, the mechanical properties of the binders are evaluated based on their stress-strain curves.[150] The toughnesses of binders are caculated by integrating their stress-strain curves based on **Equaltion 4-1**, where $\varepsilon, \varepsilon_f, \sigma$ refer to strain, the strain upon failure and stress, respectively:

$$Toughness = \frac{Energy}{Volume} = \int_0^{\varepsilon_f} \sigma \, d\varepsilon \qquad (4-1)$$

After adding triPy, the maximum strain of the binder is improved from 17% (PENDI), to 124% (PP-3) and 188% (PP-1). The improved strain enables the binder to withstand larger volume expansion. The toughness of binder refers to their ability to dissipate energy before rupturing. Compared with the toughness of PENDI (0.25 kJ/m^3), the toughness of PP-3 and PP-1 are around 8 times (2.01 kJ/m^3) and 10 times (2.54 kJ/m^3) higher. Although both the maximum strain and toughness of PP-1 are higher than that of PP-3, the cycling stability of PP-3 is slightly better than that of PP-1. I attribute this to the relative higher ratio of PENDI in PP-3 than that in PP-1, which endows the cathode with higher LiPSs confining ability. Therefore, I choose PP-3 with the ratio between triPy and PENDI as 1:3 as the optimized PP binder in the following study.

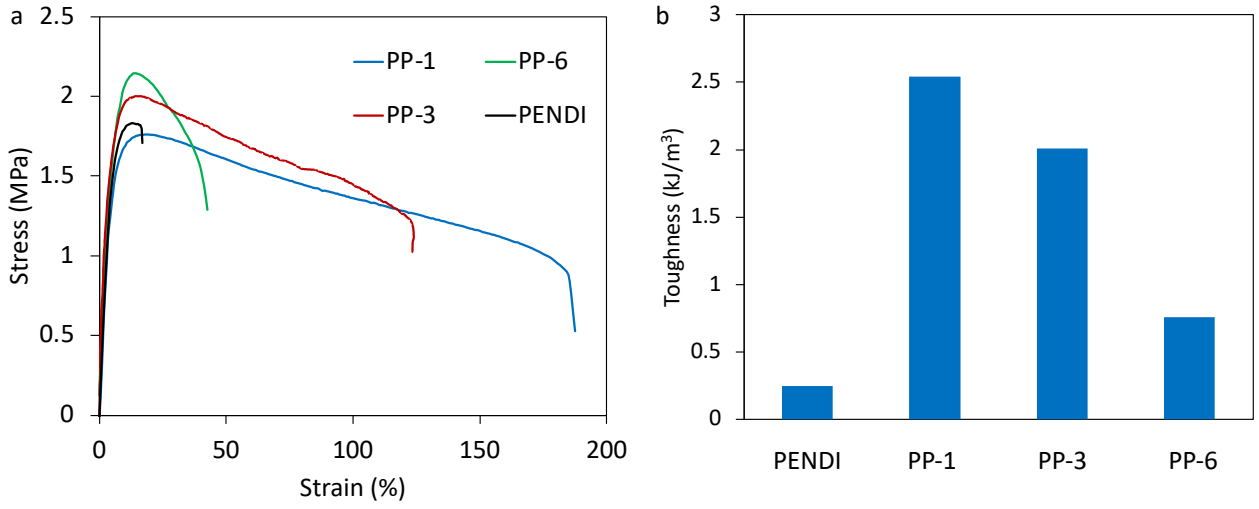

Figure 4-9. (a) Stress–strain curves of PENDI/triPy binders with different molar ratio between NDI and Py units. (b) Calculated toughnesses of PENDI/triPy binders by integrating the the stress-strain curves.

Table 4-2. Mechanical properties of PENDI/tryPy binders based on stress-strain curves.

	Young's modulus (MPa)	**Toughness (kJ/m^3)**	**Maximum stress (MPa)**	**Maximum strain (%)**
PENDI	36.4	0.25	1.80	17
PP-1	33.3	2.54	1.70	188
PP-3	43.7	2.01	2.01	124
PP-6	34.2	0.76	2.13	42

With the optimized PP binder, I further studied the cathode performances at different C rate. As shown in **Figure 4-10**, the initial discharge capacity is as high as 1441 mAh/g (86% of the theoretical gravimetric specific capacity) which demonstrates high sulfur utilization. The discharge capacity reaches around 934 mAh/g even at 1C rate, indicating good high C rate performance. The discharge capacity drops sharply when the C rate reaches 2C rate. Interestingly, the discharge capacity can recover almost fully after shifting the C rate from 2C back to 1C again. To evaluate the LiPSs confining ability of PP binder, I studied the performances of sulfur cathodes with PP binder at both low C rate (C/10 rate, **Figure 4-11a**) and high C rate (1C rate, **Figure 4-11b**) with low sulfur loading (1 mg/cm^2). The utilization of low sulfur loading is to isolate the effect of volume expansion first. Cathodes with PVDF as binders were prepared for comparison. As shown in **Figure 4-11a**, the initial discharge capacity of PP cathode reaches 1235 mAh/g and remains 74% after 100 cycles under C/10 rate. On the contrary, the capacity retention of PVDF cathode is only

43%, which is 31% lower than PP cathode. After increasing the C rate to 1C, PP cathode possesses outstanding capacity retention of almost 100%, which is much higher than that of PVDF cathode (77%). Besides, the coulombic efficiency of PP binder is around 5% higher than that of PVDF cathode, demonstrating much lower shuttle effect. We attribute this to the outstanding LiPSs trapping ability of PENDI which significantly prevents the dissolution of LiPSs from cathode side, and consequently reduces side reactions.

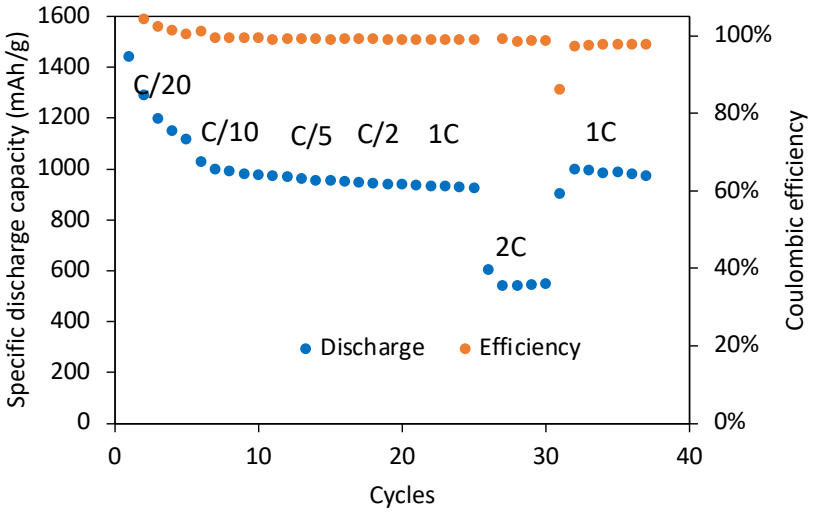

Figure 4-10. Cell performances of cathode with PP binder at different C rate (sulfur loading = 1 mg/cm^2).

Comparing the performances of cathodes with PENDI binder (**Figure 2-10**) and PP binder (**Figure 4-10, Figure 4-11**), PP binder possess similarly outstanding LiPSs confining ability with PENDI. Differently, its much higher toughness and maximum strain enable PP binder to mechanically stabilize sulfur cathode with higher sulfur loading. As shown in **Figure 4-12**, the performance of sulfur cathode with PP binder is tested at both C/10 and 1C rates with high sulfur loading = 3.5 mg/cm^2. **Figure 4-12a** demonstrates initial discharge specific capacity of 1166 mAh/g at C/10 rate and high capacity retention of 86% after 80 cycles. The areal capacities in the

first 10 cycles are higher than 4 mAh/cm^2 (**Figure 4-12b**) at C/10 rate, and still reaches 3.6 mAh/cm^2 after 80 cycles. Therefore, the utilization of PP binder enables the improvement of cathode areal capacity to the target of 4 mAh/cm^2 by increasing the thickness of sulfur cathode (**Figure 4-12c**).

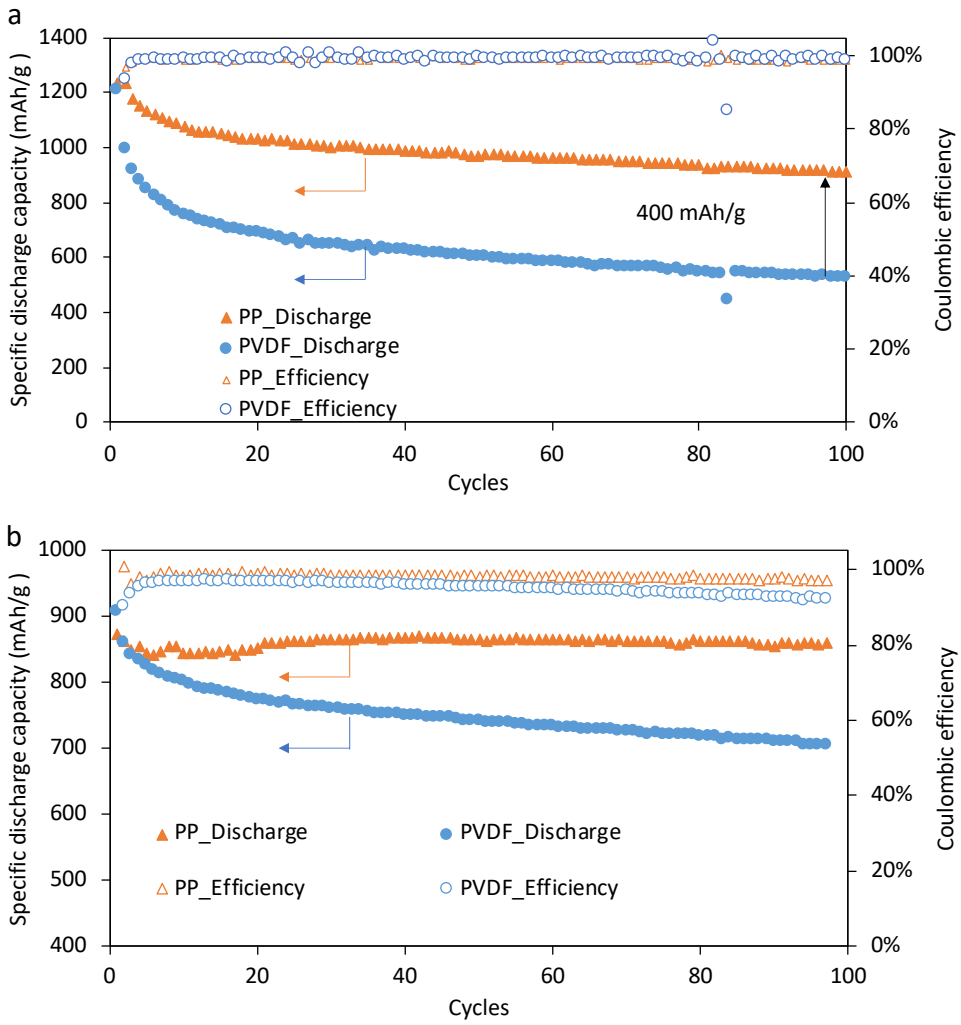

Figure 4-11. Cycling performance of cathodes with PP binder at (a) low C rate (C/10) and (b) high C rate (1C). Sulfur loading = 1 mg/cm^2.

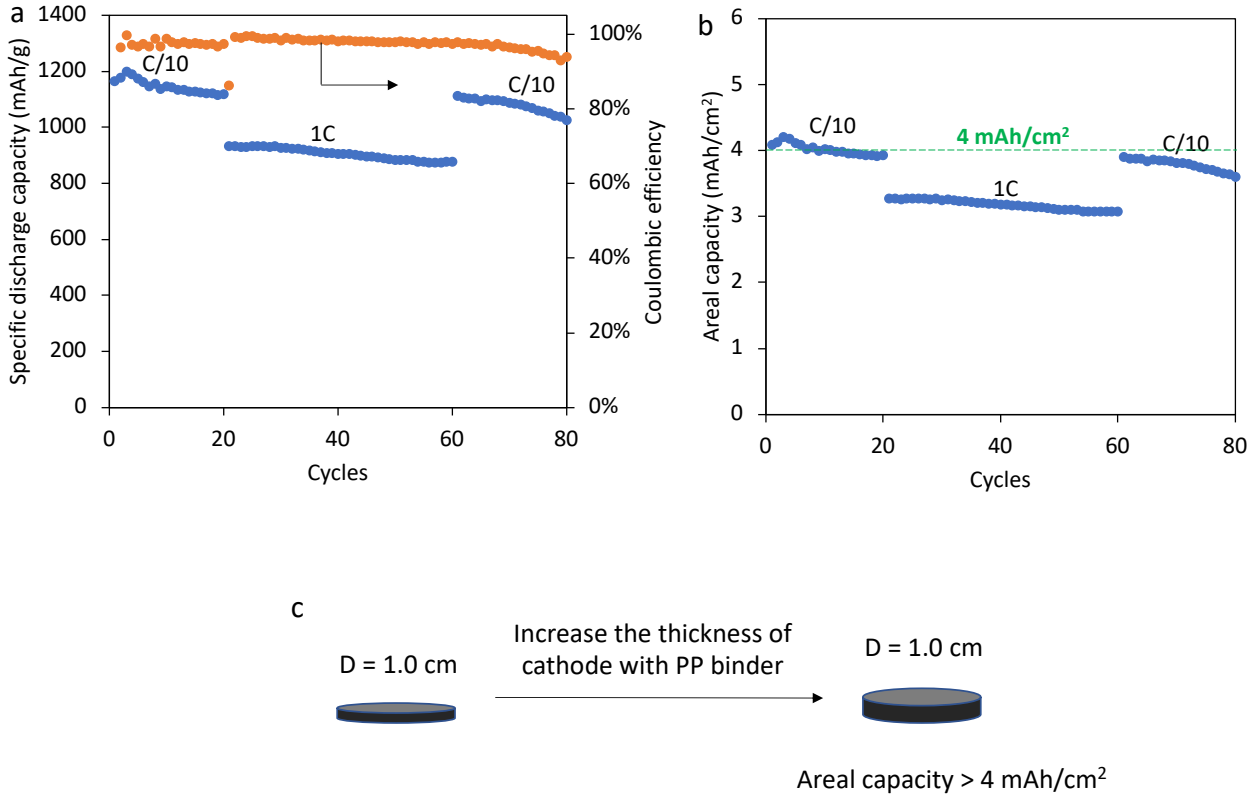

Figure 4-12. Cycling performances, including specific discharge capacity (a) and areal capacity (b), of sulfur cathode at low C rate (C/10) and high C rate (1C). Sulfur loading = 3.5 mg/cm². (c) Improving the areal capacity of sulfur cathode by increasing cathode thickness.

So far, we have demonstrated that both PENDI and PP-3 have excellent LiPSs trapping ability. The existence of reversible pi-pi interaction in PP-3 ensures the fabrication of intact cathode with higher sulfur loading. We have reached the target to increase the initial areal discharge capacity of sulfur cathode to 4.0 mAh/cm². Now we are keeping improving the capacity of the cathode by increasing the diameter of cathode from 1.0 cm to 1.6 cm (**Figure 4-13a**), leading to an increasement in cathode volume/area by 156%. However, cathodes with PP-3 binder encounters the detaching and cracking issue during the fabrication process of cathode film. Even

for cathode with PP-1 binder, which has higher toughness than PP-3, the cracks are still formed (**Figure 4-13b**).

As shown in **Figure 4-13c**, when we increase the sulfur loading of cathodes with PP-1 binder to 3.8 and 4.2 mg/cm^2, the initial discharge capacities reach 951 and 762 mAh/g at C/10 rate, respectively. Their discharge capacities remain very stable in the first seven cycles. This demonstrates there is no significant LiPSs dissolution problem due to the excellent LiPSs confining ability of PENDI. However, the discharge capacity drops sharply from the 8th cycles. We attribute this change trend to the poor mechanical integration of the cathodes. From the cathode image (**Figure 4-13b**), we can see that cracks are formed before cycling. After immersing the prepared cathode in electrolyte for 48 hours, the cathode with cracks is easily to disintegrate (**Figure 4-15a**), which prevents the electron transportation within cathode during cycling. Different from the cycling failure of cathode caused by mechanical damage, the LiPSs dissolution problem of sulfur cathode typically leads to a significant capacity drop at the first several cycles. This is because the initial cycles have the highest LiPSs diffusion driving force. As for capacity decay caused by cracks, cracks are formed gradually and uniformly (**Figure 4-7a**), leading to relative smooth capacity decay. Once cathode disintegrates and detaches from Al current collector, there will be a sharp capacity decrease. We attribute this mechanical failure to the increased area of sulfur cathode which leads to increasement in tension stress during the cathode fabrication process. To solve this problem, we need to increase the cathode mechanical property further.

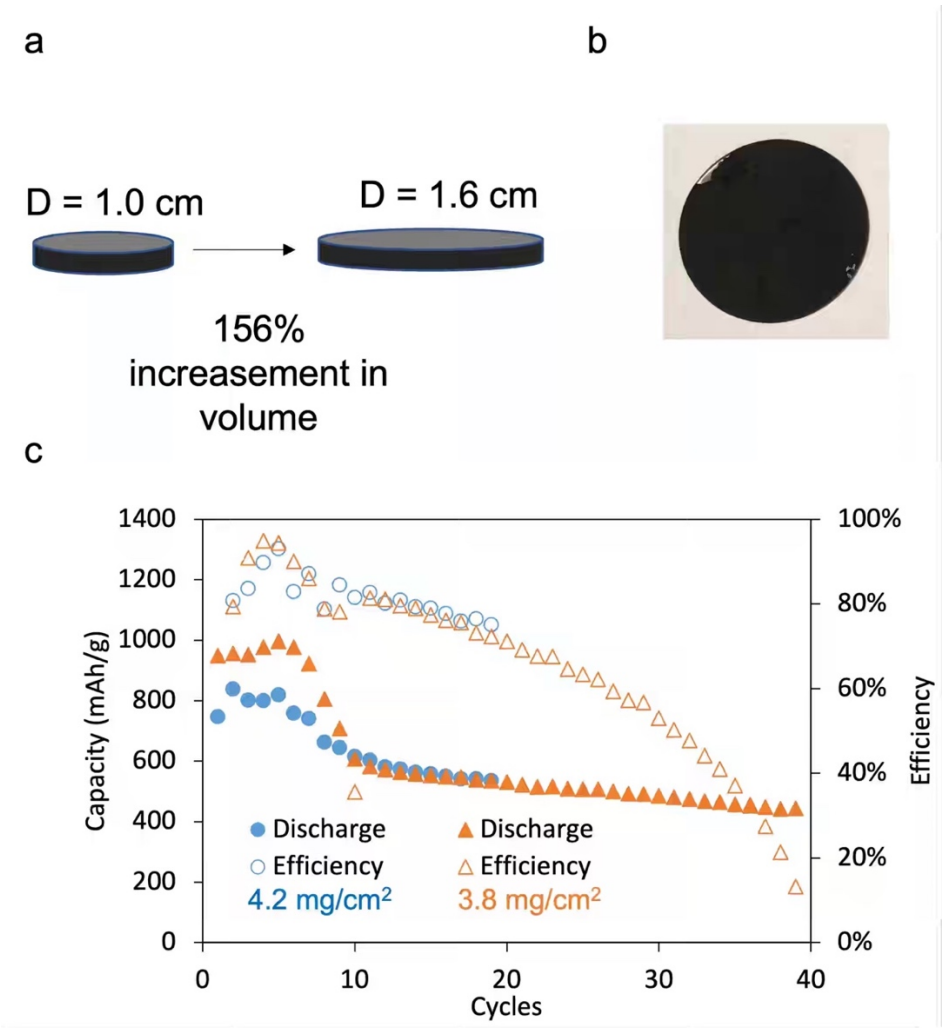

Figure 4-13. (a) Fabrication of high-capacity sulfur cathode by increasing cathode diameter from 1.0 cm to 1.6 cm; (b) Sulfur cathode with cracks before cycling; (c) Cell performances of cathodes with PP-1 binders at C/10 rate with sulfur loading of 3.5 mg/cm^2 and 4.2 mg/cm^2.

4.3.3 High-Capacity Sulfur Cathode with PENDI/triPy/PVDF Binder

To mitigate the damage of sulfur cathode with high loading and high area, the toughness of sulfur cathode needs to be enhanced further. As shown in **Figure 4-9a** and **Equation 4-1**, toughness is related to the area under the stress-strain curve. To be tough, the binder should withstand both high strain and high strain. The ideal volume expansion for converting S_8 to Li_2S

is around 80%. Then the corresponding axial elongation is around 22% if treating S_8/L_2S particle as sphere. From the practical perspective, only the toughness within the strain of cathode will benefits to improve the integration of sulfur cathode. Given the fact that the maximum axial strain of PP-3 is 125%, much higher than that of 22%, further improving the strain wouldn't mitigate the formation of cracks significantly. On the contrary, improving the strain and Young's modulus of the binder will be more promising to improve the integration of sulfur cathode.

Despite its poor LiPSs confining ability, PVDF as a commonly used binder has good stickiness and high Young's modules (> 1.67 GPa). From another perspective, addition of PVDF could possibly complement PP-3 to improve the binder toughness by increasing the stain and Young's modulus. A resulting PENDI/triPy/PVDF was made by adding PVDF into PP-3 with PP-3:PVDF = 3:1 by weight. Compared with PP-3, the addition of PVDF decreases the maximum stain from124% to 61% (**Figure 4-14**, **Table 4-3**). However, the maximum stress and Young's modulus of PENDI/triPy/PVDF are 4.9 and 4.6 times higher than that of PP-3, leading to the increasement of toughness from 2.01 to 5.45 kJ/cm^3. When comparing the toughness at the same strain, taking 50% for example, the toughness of PENDI/triPy/PVDF is around 3.9 times higher than that of PP-3.

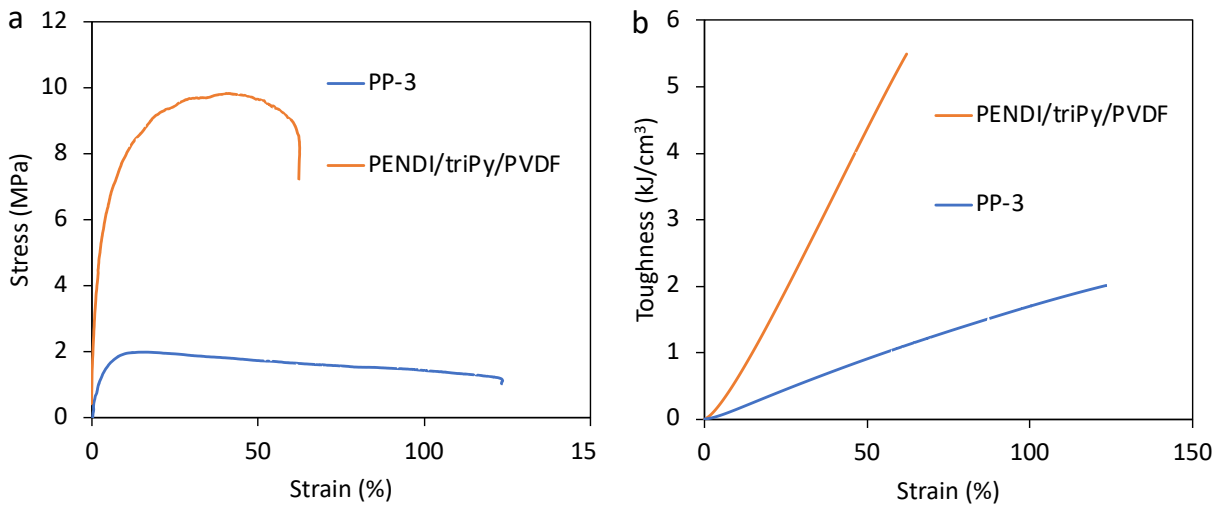

Figure 4-14. The stress-strain curves (a) and the toughness-strain curves (b) of PP-3 and PENDI/triPy/PVDF. The toughness at different strain is calculated based on the stress-strain curves and **Equation 4-1**.

Table 4-3. Mechanical properties of PP-3 and PENDI/triPy/PVDF binders based on stress-strain curves.

	Young's modulus (MPa)	**Toughness (kJ/m³)**	**Maximum stress (MPa)**	**Maximum strain (%)**
PP-3	43.7	2.01	2.01	124
PENDI/triPy/PVDF	203.4	5.45	9.82	61

As shown in **Figure 4-15**, sulfur cathode with PP binder tends to peel off from the Al foil and breaks into pieces after immersed into electrolyte for 48 hours. On the contrary, PENDI/triPy/PVDF binder helps sulfur cathode maintain intact after immersed in electrolyte for 48 h. Figure **4-16a** shows the cell performances of PENDI/triPy/PVDF cathode (sulfur loading = 4.4 mg/cm²) at different C rate. The initial discharge capacity of the cathode reaches 10.5 mAh

with a specific discharge capacity of 1208 mAh/g at C/20 rate, which reaches the target of 10 mAh cathode capacity at the initial cycle. The discharge capacity remains 7.6 mAh after 80 cycles. The cathode with PENDI/triPy/PVDF binder also demonstrates high specific discharge capacity (947 mAh/g) even cycling at C/2 rate, as well as excellent capacity retention of 77% based on the 2nd cycle at C/10 rate after 80 cycles. As shown in **Figure 4-16b**, cathode with PENDI/triPy/PVDF binder demonstrates stable discharge/charge voltage profile within 80 cycles at different C rate. Typical discharge voltage profiles with two plateaus at both 2nd and 80th cycles are observed (**Figure 4-16c**), demonstrating stable discharge reaction to convert S_8 to Li_2S. Besides, the polarization ΔE (0.33 V) at the 80th cycle is slightly higher than that (0.31 V) at the 2nd cycle, which exhibits stable cell resistance.

The performance of cathode with PVDF binder (sulfur loading = 4.2 mg/cm^2) was investigated for comparison. Although cathode with PVDF binder shows high initial discharge capacity of 11.2 mAh at C/20 rate, the cell fails quickly after the 1st discharge process (**Figure 4-17a**). In the following charge process, a typical shuttle effect voltage profile is observed. This means that cathode with PVDF binder is suffering from significant shuttle effect.

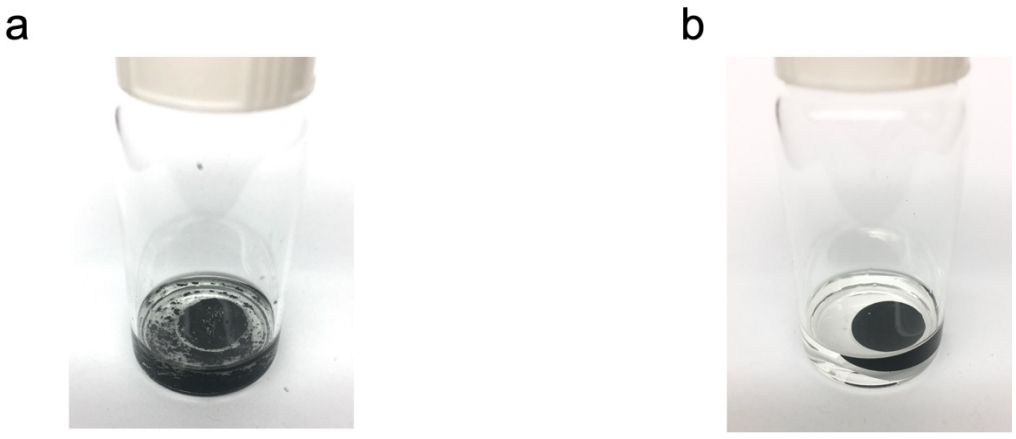

Figure 4-15. Images of cathode with PP binder (a) and PENDI/triPy/PVDF binder (b) after immersed in DOL/DME electrolyte for 48 hours.

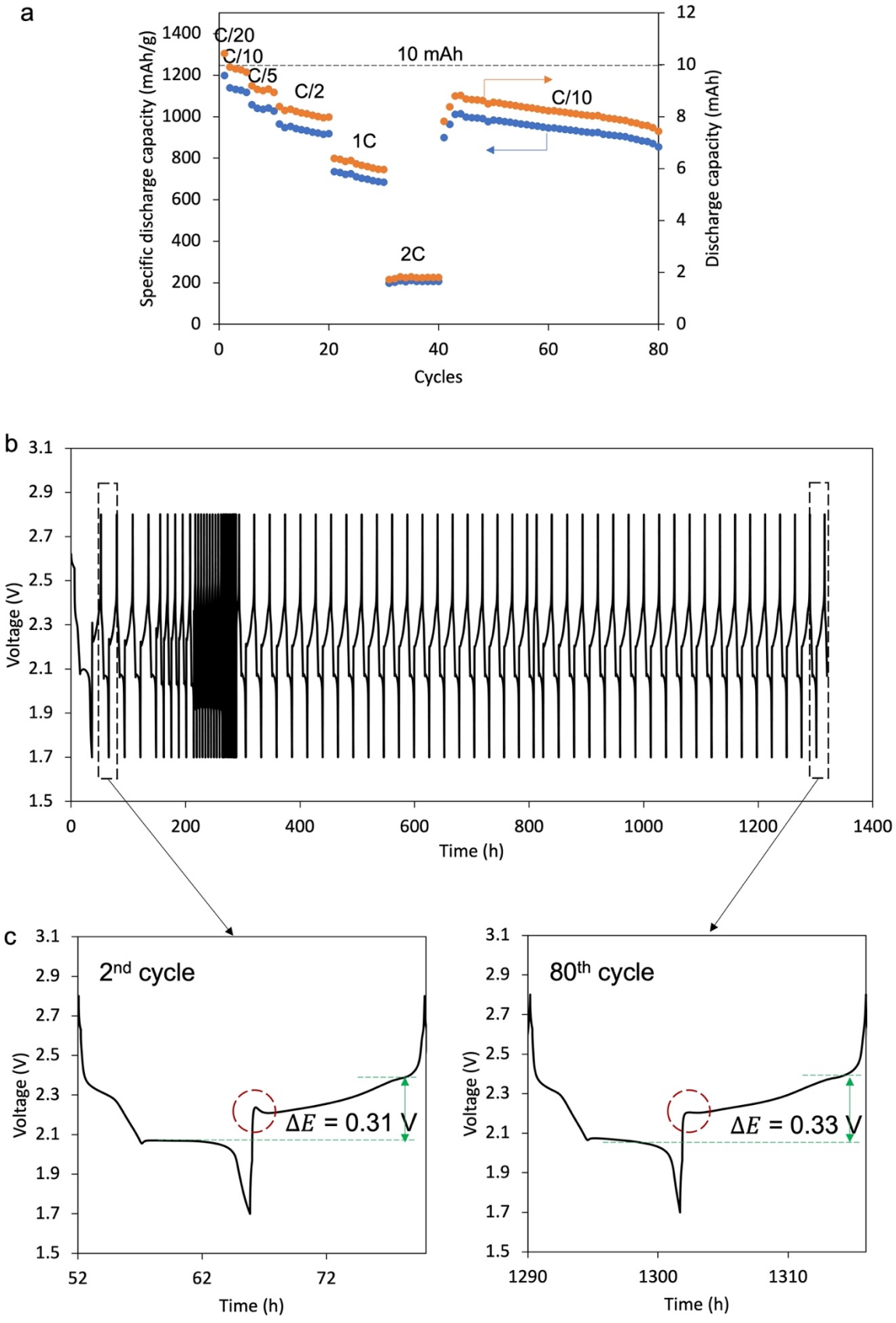
a
Specific discharge capacity (mAh/g)
Discharge capacity (mAh)
Cycles
C/20
C/10
C/5
C/2
1C
2C
10 mAh
C/10
b
Voltage (V)
Time (h)
c
2nd cycle
80th cycle
ΔE = 0.31 V
ΔE = 0.33 V
Voltage (V)
Time (h)

Figure 4-16. (a) Cell performance of cathode with PENDI/triPy/PVDF binder at different C rate (sulfur loading = 4.4 mg/cm^2); (b) The corresponding discharge/charge voltage profile of cathode with PENDI/triPy/PVDF binder in 80 cycles at different C rate; (c) The corresponding discharge/charge voltage profile of cathode with PENDI/triPy/PVDF binder at 2nd cycle (C/10 rate) and 80th cycle (C/10 rate).

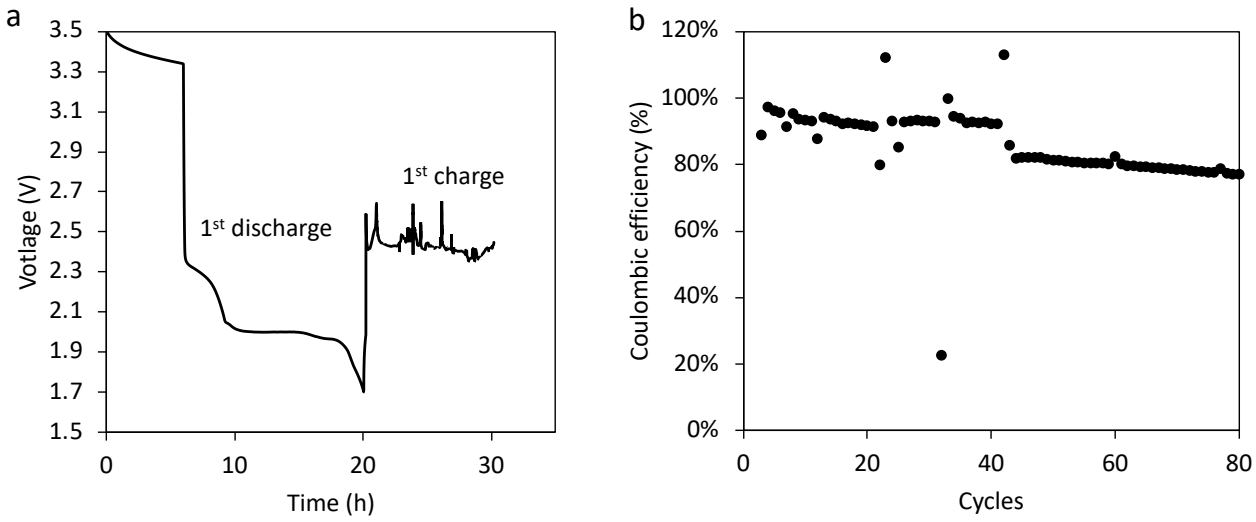

c

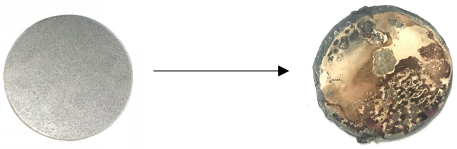

Figure 4-17. (a) Discharge/charge voltage profile of cathode with PVDF binder (sulfur loading = 4.2 mg/cm^2); (b) The corresponding coulombic efficiency of cathode with PENDI/triPy/PVDF binder in Figure 4-16a; (c) Images of fresh Li anode and Li anode after 30 cycles.

Although cathode with PENDI/triPy/PVDF binder demonstrates strong LiPSs confining ability and high retention of discharge capacity, shuttle effect is still observed during the cycling

based on the following evidence: First, the characteristic overpotential peak at the beginning of charge voltage profile appears at the 2nd cycle, however, then disappears at the 80th cycle (**Figure 4-16c**, red cycles). The disappearance of the overpotential peak, referring to the phase reaction to convert solid Li_2S to liquid LiPSs, demonstrates that significant amount of LiPSs has already dissolved in the bulk electrolyte. Second, the coulombic efficiency of cathode with PENDI/triPy/PVDF decreases with the increase of cycles (**Figure 4-17b**). The coulombic efficiency at the 80th cycle is only 77%, demonstrating that 23% of the specific charged capacity is consumed in the anode side due to the side reactions between LiPSs, organic electrolyte and Li mental. Third, side reaction in the anode side is clearly observed from the optical image of Li anode after cycling. As shown in **Figure 4-17c**, the smooth and even surface of fresh Li anode is corroded and covered with rough solid electrolyte interface layer, which consumes both fresh Li mental and organic electrolyte.

4.4 CONCLUSIONS

In this chapter, I developed a series of binders based on PENDI to achieve high-loading, long-cycle-life sulfur cathode (**Figure 4-18**). Due to the excellent LiPSs confining ability, cathode with PENDI binder demonstrates 47% improvement in discharge capacity retention after 200 cycles at low sulfur loading (1 mg/cm^2) when compared with cathode with PVDF binder. By utilizing triPy crosslinker, the toughness of the resulting PP-3 binder is enhanced by 8 times, which enables the fabrication of sulfur cathode with high areal discharge capacity of 4.1 mAh/cm^2 at C/10 rate. To integrate the cathode further, PVDF is added to form the PENDI/triPy/PVDF binder which improves the toughness and Young's modules by 2.7 and 4.6 times, respectively, leading to the fabrication of high-loading, high-capacity cathode with discharge capacity > 10 mAh. The

resulting cathode also demonstrates high retention of discharge capacity of 0.28% per cycle. The discharge capacity of the cathode still reaches 7.4 mAh after long cycling time of 1320 hours. Compared with PENDI cathode, we attribute the improved mechanical integration of cathode based on PENI/triPy/PVDF binder to two reasons: First, the reversible interaction between NDI and Py improves the strain and toughness which helps dissipate the stress energy. Second, the existence of PVDF improves the stiffness and stress of the binder which helps withstand the stress caused by volume expansion and fabrication pressure. For comparison, cathode with PVDF binder at high sulfur loading fails after the first discharge process. Despite the excellent LiPSs confining ability of PENDI-based binder, shuttle effect is observed during the cycling of cathode with PENDI/triPy/PVDF binder.

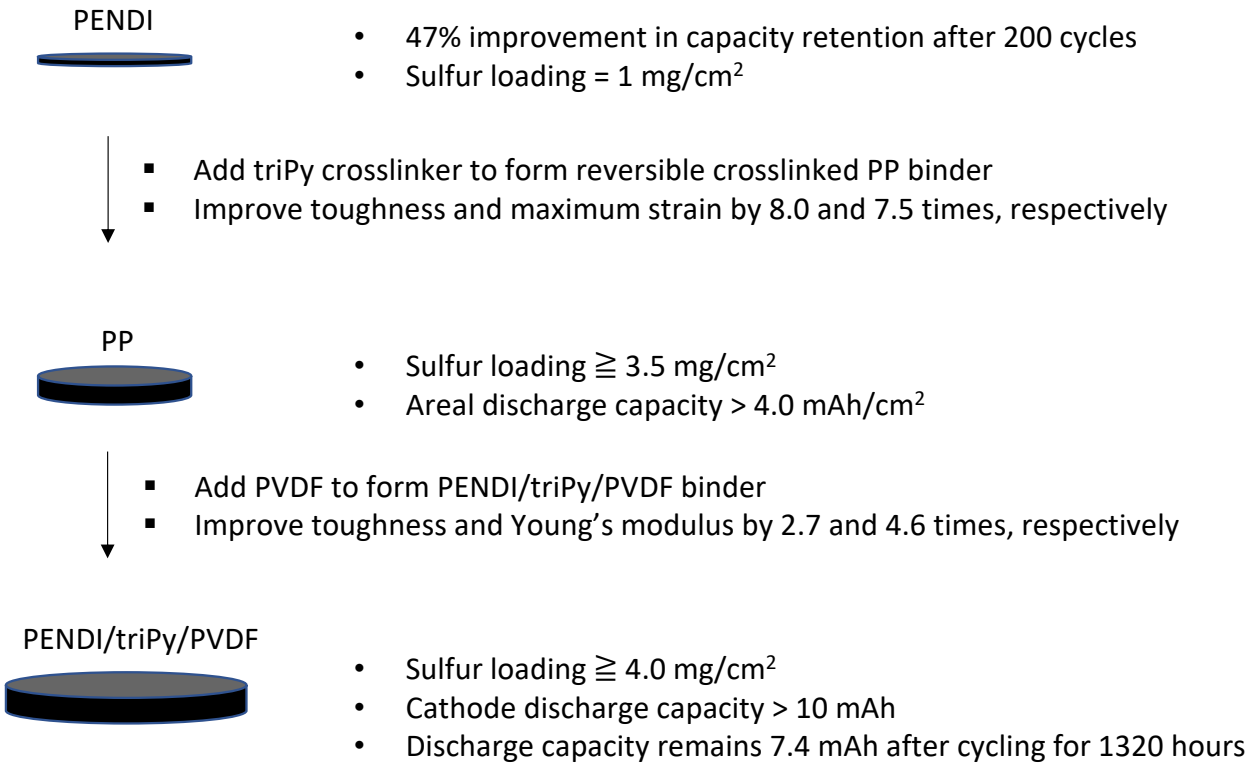

Figure 4-18. Summary of the PENDI-based binders and the corresponding fabricated cathodes with increased sulfur loading, areal capacity, and cathode capacity.

CHAPTER 5: CONCLUSIONS AND FUTURE PERSPECTIVES

5.1 CONCLUSIONS

This doctoral dissertation has focused on my efforts to study and develop multi-functional binders based on PEDNI for high-loading, long-cycle-life sulfur cathode in lithium-sulfur batteries. Chapter 1 introduced the major challenges in sulfur cathode and the motivation of this research. By adopting molecular engineering approach, Chapters 2-4 cover my research from confining LiPSs in molecular level, designing reversibly crosslinked network structure in supramolecular level, and then fabricating high-loading sulfur cathode in device level.

5.1.1 Confining LiPSs Through Redox Mediation and Chemical Interactions

Despite its advantages including superior energy density and low cost, the development of lithium-sulfur batteries is hindered by the dissolution of LiPSs, leading to significant capacity decay even for cathode with low sulfur loading. Here I have developed a novel binder PENDI based on redox active naphthalene diimide (NDI) which entraps LiPSs through chemical interactions and oxidations. First, reductive NDI transforms long-chain LiPSs into short-chain LiPSs and mediates the conversion of LiPSs into sulfates and polythionates on the surface of host matrix, which prevents the dissolution of LiPSs due to the low solubility of reduction products Li_2S_2, and Li_2S, oxidation products thiosulfate and polythionate. Second, carbonyl groups in NDI and the formed NDI^{2-} dianions from the reaction between NDI and LiPSs, further confine LiPSs *via* chemical interactions. The cathodes with PENDI binder exhibit high initial discharge capacity (1207 mAh/g at 0.1C rate) and 47% improvement in capacity retention after 200 cycles compared to the one using PVDF as a binder. I provide a promising strategy to control dissolution of LiPSs

via an organic redox active binder to achieve long-cycle-life sulfur cathode. The versatile design flexibility of NDI derivatives suggests potential to improve Li-S performance further.

5.1.2 Modulating the Mechanical and Self-healing Properties of Reversibly Crosslinked PENDI/triPy Network Structure

To improve the mechanical property of PENDI, supramolecular network structure PENDI/triPy is developed which not only enhances the mechanical property significantly to mitigate the formation of cracks, but also enables to self-heal cracks that have already formed. Although various self-healing polymers have been developed, individual designs are generally limited to a narrow range of mechanical properties and self-healing temperatures, as it's challenging to tune these characteristics over a wide range without re-engineering the molecular structure entirely. Here, a strategy to decouple self-healing and mechanical properties from the covalent structure of supramolecular polymers and a novel material system developed using this strategy, which is based on non-covalent pi–pi interactions between NDI and Py derivatives, are reported. Through targeted, stoichiometric addition of small model compounds, both binding strength and overall density of crosslinking interactions are modulated successfully. This strategy allows us to tune both self-healing temperature (30–60 °C) and Young's modulus (63–250 MPa) of our materials over a wide range, without changing the structure of polymer components. The rational design strategy and resultant material platform demonstrated not only provide an efficiently way to improve the mechanical properties of PENDI, but also represent a first step towards a class of supramolecular polymers for electrochemical devices with highly tunable mechanical and self-healing properties.

5.1.3 Fabricating High-Loading, Long-Cycle-Life Sulfur Cathode Based on PENDI Binders

Chapter 2 has demonstrated the outstanding LiPSs confining ability of PENDI in molecular level. In the supramolecular level, Chapter 3 provided strategy to enhance the mechanical properties of PENDI. Building upon Chapter 2 and Chapter 3, Chapter 4 integrates all the proposed molecular designs and focuses on developing and optimizing high-loading, long-cycle-life sulfur cathode. By utilizing triPy crosslinker, the toughness of the resulting PENDI/triPy binder is enhanced by 8 times, which enables the fabrication of sulfur cathode with high areal discharge capacity of 4.1 mAh/cm^2 at C/10 rate. I attribute the improvement to the reversible interaction between NDI and Py which improves the maximum strain and toughness of the binder. To integrate the cathode further, PVDF is added to form the PENDI/triPy/PVDF binder which improves the toughness and Young's modules by 2.7 and 4.6 times, respectively, helping withstand the stress caused by volume expansion/shrinkage and fabrication pressure. The resulting high-loading cathode demonstrates high discharge capacity (> 10 mAh) and capacity retention of 0.28%/cycle. The discharge capacity of the cathode still reaches 7.6 mAh after a long cycling time of 1320 hours.

5.2 FUTURE PERSPECTIVES

5.2.1 Design of Highly Stretchable Binder with Double Network Structure

Chapter 4 demonstrated the crucial role of a binder with high mechanical properties in the fabrication of high-loading sulfur cathode. The resulting PENDI/triPy/PVDF binder mechanically stabilizes sulfur cathode *via* two mechanisms: First, the high Young's modulus (203.4 MPa) enables the binder withstand tension stress elastically. However, due to its poor elasticity, the binder undergoes non-elastic deformation once the strain is larger than ~4% (**Figure 4-14a**).

Second, the toughness (5.45 kJ/m^3) of the binder dissipates the stress energy by reversibly breaking the reversible pi-pi interactions between NDI and Py units or permanently breaking the polymer chains, leading to irreversible damage of the binder.

Besides high toughness, a high stretchability of the binder is also desired to improve the mechanical reversibility for high-loading sulfur cathode. Sun and co-workers reported a highly stretchable double network structure which consisting of reversibly and covalently crosslinked networks.[151] As shown in **Figure 5-1**, after combining the alginate-based reversibly crosslinked network and polyacrylamide-based covalently network, both the toughness and Young's modules of the resulting double network structure are improved dramatically. Especially, the elastic strain and maximum strain are improved to around 300% and 1700%, respectively.

Therefore, a similar double network structure based on reversibly crosslinked PENDI/triPy network and covalently crosslinked poly(ethylene glycol) dimethacrylate (PEGDMA) is promising to improve the toughness and stretchability of the PENDI-based binder simultaneously. In detail, the reversibly breaking of pi-pi interaction between NDI and Py dissipates the stress energy. The covalent crosslinks preserver the memory of the initial state which recover the binder state after unloading the deformation stress. Consequently, the stretchability of the binder will be enhanced which enables longer cycle life of sulfur cathode. To achieve the ideal result, the crosslinking density, relative molecular ratio between the two network structures, molecular weight of the PEGDMA monomer, *etc*. need to be optimized.

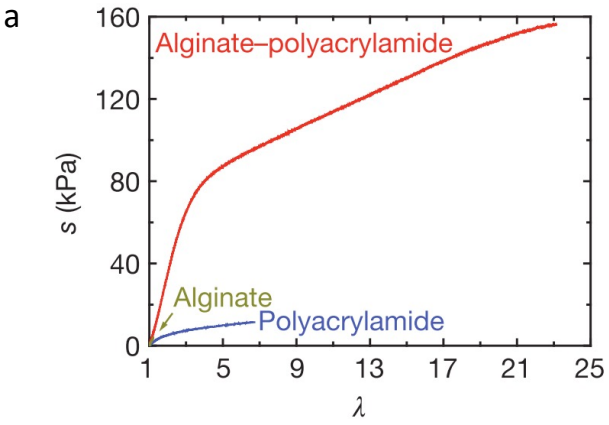
a
160
120
80
40
0
s (kPa)
Alginate–polyacrylamide
Alginate
Polyacrylamide
1
5
9
13
17
21
25
λ

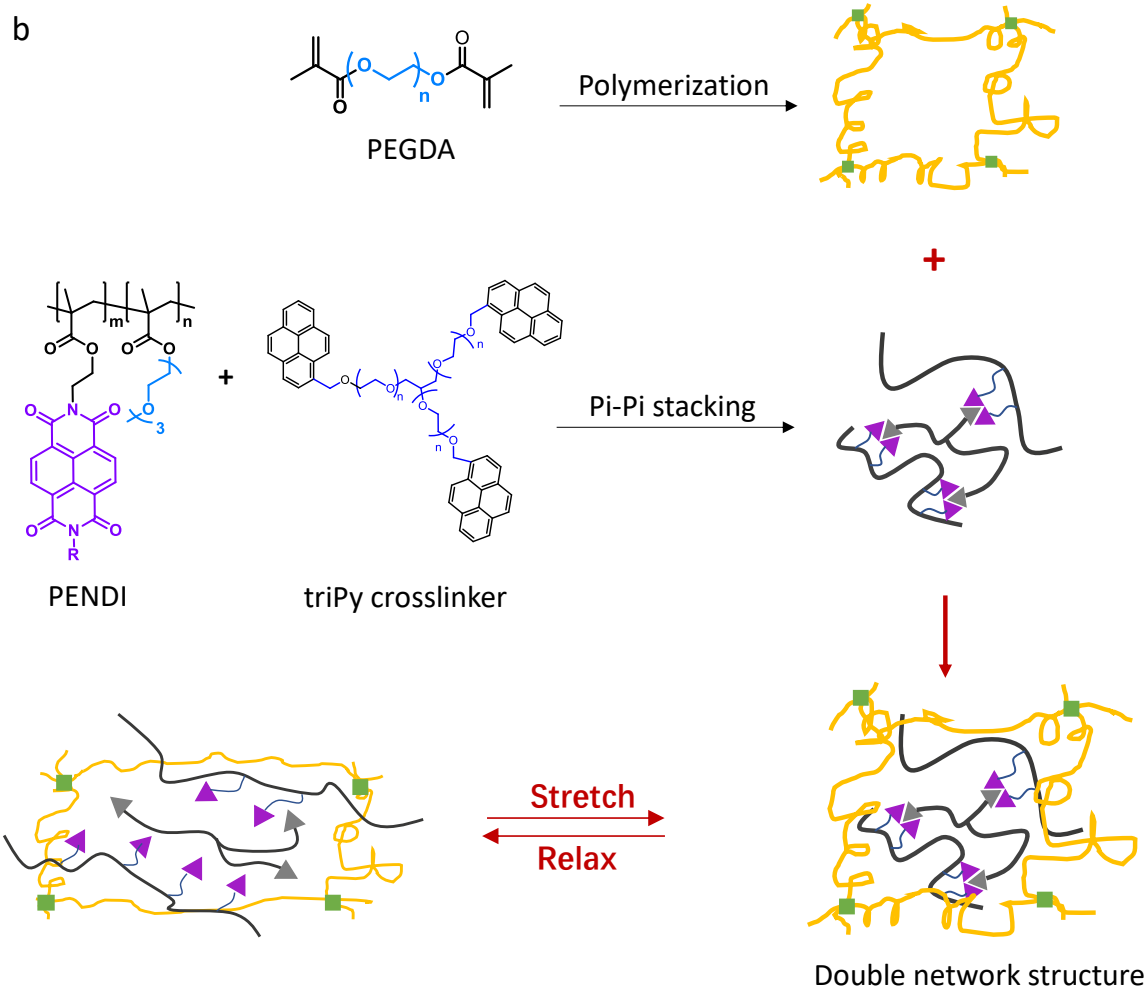
b
PEGDA
Polymerization
+
PENDI
+
triPy crosslinker
Pi-Pi stacking
Stretch
Relax
Double network structure

Figure 5-1. (a) The reported double network structure based on alginate and polyarcylamide;[151] (b) The proposed double network structure based on PENDI/triPy and PEGDMA to enhance the stretchability and toughness of PENDI-based binder.

5.2.2 Passivation of Lithium Anode

Despite the excellent LiPSs confining ability of PENDI-based binder, considerable shuttle effect is observed during the cycling of high-loading (> 4 mg/cm^2) and high-capacity (> 10 mAh) cathodes with PENDI/triPy/PVDF binder (**Figure 4-17b** and **Figure 4-17c**). As the most electropositive element on the periodic table, lithium metal could react with DOL/DME organic electrolyte to form the solid-electrolyte interphase (SEI) layer. An uneven SEI layer enables the electron transfer to react with LiPSs, leading to redox shuttling effect. Meanwhile, the continue consumption of electrolyte could possibly reduce the Li ion conductivity and increase the internal resistance. To stabilize the cycling performance of the whole cell, necessary passivation of the lithium anode is needed to stabilize the SEI and prevent side reactions in the anode side.

5.2.3 Optimization of E/S Ratio

From the scope of the whole cell device, the electrolyte/sulfur (E/S) weight ratio profoundly affect the energy density of the cell. As shown in **Figure 5-2**, both the sulfur loading, and E/S ratio play crucial role in gravimetric energy density of the cell. From one hand, a low E/S ratio could improve the gravimetric energy density of the cell by increasing the weight ratio of electrode active materials, which are sulfur in cathode and lithium mental in anode. From the other hand, decent amount of electrolyte helps wet the electrodes well, reduce the polarization and internal resistance, consequently, improve the Li ion conductivity and reaction kinetics. Given the

fact that electrolyte will be continually consumed during the cell cycling, an optimized E/S ratio is highly desired to improve the energy density of the cell in long-term cycling. As shown in **Figure 5-2b**, I have primarily studied the effect of E/S ratio on cathode cycling performances. By reducing E/S weight ratio from 10 to 7, the specific discharge capacity won't be affected. A lower E/S ratio of 5 enable the cathode with more stable cycling performances, however, lower specific discharge capacity. To achieve the best performance in terms of both cycling stability and energy density, a systematic optimization is needed.

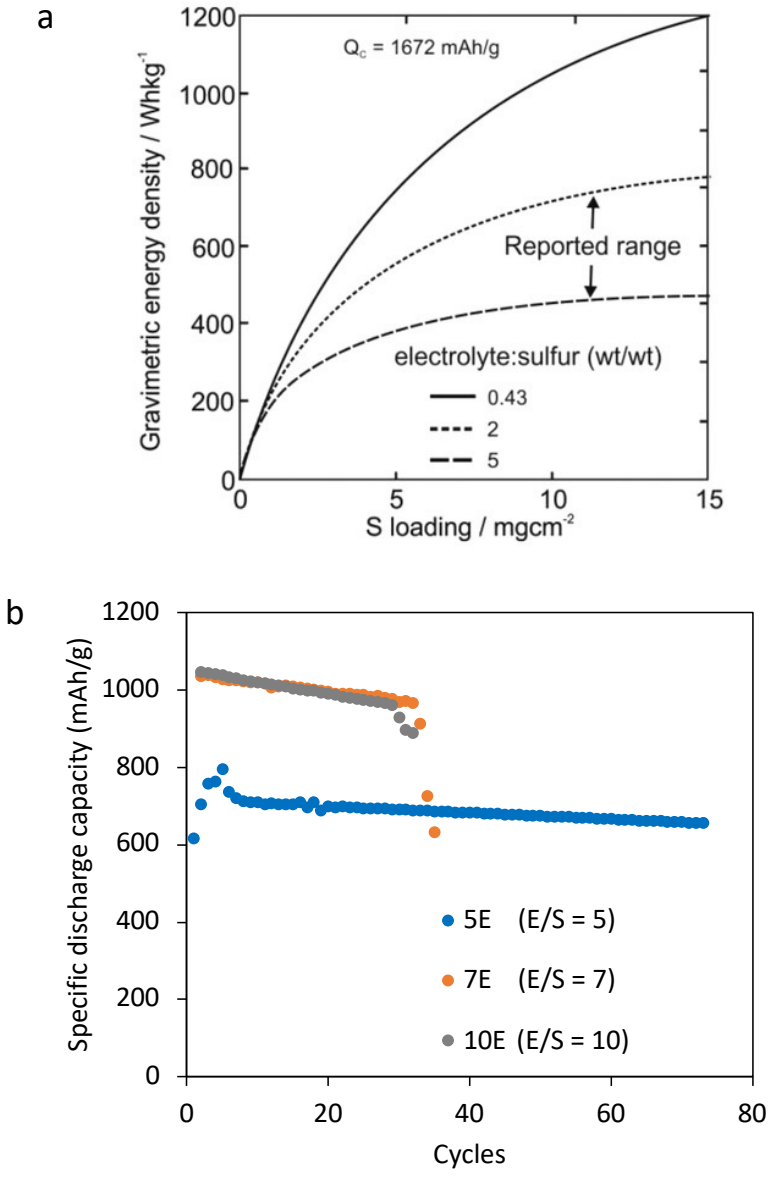

Figure 5-2. (a) The effect of E/S ratio on the relation between specific energy and sulfur loading;[152] (b) Cycling performances of cathodes with different E/S ratios. The sulfur loadings are 4.1 mg/cm^2 (5E), 4.7 mg/cm^2 (7E) and 4.2 mg/cm^2 (10E).

BIBLIOGRAPHY

(1) Dunn, B.; Kamath, H.; Tarascon, J. M. Electrical Energy Storage for the Grid: A Battery of Choices. *Science*. **2011**, *334* (6058), 928–935.

(2) Lin, D.; Liu, Y.; Cui, Y. Reviving the Lithium Metal Anode for High-Energy Batteries. *Nat Nano* **2017**, *12* (3), 194–206.

(3) Liu, W.; Lee, S. W.; Lin, D.; Shi, F.; Wang, S.; Sendek, A. D.; Cui, Y. Enhancing Ionic Conductivity in Composite Polymer Electrolytes with Well-Aligned Ceramic Nanowires. *Nat. Energy* **2017**, *2* (5), 17035–17041.

(4) Nitta, N.; Wu, F.; Lee, J. T.; Yushin, G. Li-Ion Battery Materials: Present and Future. *Mater. Today* **2015**, *18* (5), 252–264.

(5) Kalnaus, S.; Wang, Y.; Turner, J. A. Mechanical Behavior and Failure Mechanisms of Li-Ion Battery Separators. *J. Power Sources* **2017**, *348*, 255–263.

(6) Goodenough, J. B.; Park, K. S. The Li-Ion Rechargeable Battery: A Perspective. *J. Am. Chem. Soc.* **2013**, *135* (4), 1167–1176.

(7) Zhou, L.; Zhang, K.; Hu, Z.; Tao, Z.; Mai, L.; Kang, Y.-M.; Chou, S.-L.; Chen, J. Recent Developments on and Prospects for Electrode Materials with Hierarchical Structures for Lithium-Ion Batteries. *Adv. Energy Mater.* **2018**, *8* (6), 1701415–1701437.

(8) Li, F.; Liu, Q.; Hu, J.; Feng, Y.; He, P.; Ma, J. Recent Advances in Cathode Materials for Rechargeable Lithium-Sulfur Batteries. *Nanoscale* **2019**, *11* (33), 15418–15439.

(9) Yang, Y.; Zheng, G.; Cui, Y. Nanostructured Sulfur Cathodes. *Chem. Soc. Rev.* **2013**, *42* (7), 3018–3032.

(10) Rosenman, A.; Markevich, E.; Salitra, G.; Aurbach, D.; Garsuch, A.; Chesneau, F. F. Review on Li-Sulfur Battery Systems: An Integral Perspective. *Adv. Energy Mater.* **2015**, *5* (16), 1500212–1500232.

(11) Pang, Q.; Liang, X.; Kwok, C. Y.; Nazar, L. F. Advances in Lithium-Sulfur Batteries Based on Multifunctional Cathodes and Electrolytes. *Nat. Energy* **2016**, *1* (9), 16132–16142.

(12) Manthiram, A.; Fu, Y.; Su, Y. S. Challenges and Prospects of Lithium-Sulfur Batteries. *Acc. Chem. Res.* **2013**, *46* (5), 1125–1134.

(13) Ren, W.; Ma, W.; Zhang, S.; Tang, B. Recent Advances in Shuttle Effect Inhibition for Lithium Sulfur Batteries. *Energy Storage Mater.* **2019**, *23*, 707–732.

(14) Wang, D. W.; Zeng, Q.; Zhou, G.; Yin, L.; Li, F.; Cheng, H. M.; Gentle, I. R.; Lu, G. Q. M. Carbon-Sulfur Composites for Li-S Batteries: Status and Prospects. *J. Mater. Chem. A* **2013**, *1* (33), 9382–9394.

(15) Ai, G.; Dai, Y.; Mao, W.; Zhao, H.; Fu, Y.; Song, X.; En, Y.; Battaglia, V. S.; Srinivasan, V.; Liu, G. Biomimetic Ant-Nest Electrode Structures for High Sulfur Ratio Lithium–Sulfur Batteries. *Nano Lett.* **2016**, *16* (9), 5365–5372.

(16) Kang, W.; Deng, N.; Ju, J.; Li, Q.; Wu, D.; Ma, X.; Li, L.; Naebe, M.; Cheng, B. A Review of Recent Developments in Rechargeable Lithium–Sulfur Batteries. *Nanoscale* **2016**, *8* (37), 16541–16588.

(17) Pan, H.; Chen, J.; Cao, R.; Murugesan, V.; Rajput, N. N.; Han, K. S.; Persson, K.; Estevez, L.; Engelhard, M. H.; Zhang, J. G.; et al. Non-Encapsulation Approach for High-Performance Li-S Batteries through Controlled Nucleation and Growth. *Nat. Energy* **2017**, *2* (10), 813–820.

(18) Chen, L.; Dietz Rago, N. L.; Bloom, I. D.; Shaw, L. L. New Insights into the Electrode

Mechanism of Lithium Sulfur Batteries via Air-Free Post-Test Analysis. *Chem. Commun.* **2016**, *52* (64), 9913–9916.
(19) Seh, Z. W.; Li, W.; Cha, J. J.; Zheng, G.; Yang, Y.; McDowell, M. T.; Hsu, P. C.; Cui, Y. Sulphur-TiO2 Yolk-Shell Nanoarchitecture with Internal Void Space for Long-Cycle Lithium-Sulphur Batteries. *Nat. Commun.* **2013**, *4*, 1331–1336.
(20) Fang, R.; Zhao, S.; Sun, Z.; Wang, D. W.; Cheng, H. M.; Li, F. More Reliable Lithium-Sulfur Batteries: Status, Solutions and Prospects. *Adv. Mater.* **2017**, *29* (48), 1606823–1606847.
(21) Peng, L.; Wei, Z.; Wan, C.; Li, J.; Chen, Z.; Zhu, D.; Baumann, D.; Liu, H.; Allen, C. S.; Xu, X.; et al. A Fundamental Look at Electrocatalytic Sulfur Reduction Reaction. *Nat. Catal.* **2020**, *3* (9), 762–770.
(22) Li, T.; Bai, X.; Gulzar, U.; Bai, Y. J.; Capiglia, C.; Deng, W.; Zhou, X.; Liu, Z.; Feng, Z.; Proietti Zaccaria, R. A Comprehensive Understanding of Lithium–Sulfur Battery Technology. *Adv. Funct. Mater.* **2019**, *29* (32), 1901730–1901785.
(23) Fang, R.; Zhao, S.; Pei, S.; Qian, X.; Hou, P. X.; Cheng, H. M.; Liu, C.; Li, F. Toward More Reliable Lithium-Sulfur Batteries: An All-Graphene Cathode Structure. *ACS Nano* **2016**, *10* (9), 8676–8682.
(24) Moon, S.; Jung, Y. H.; Jung, W. K.; Jung, D. S.; Choi, J. W.; Kim, D. K. Encapsulated Monoclinic Sulfur for Stable Cycling of Li-S Rechargeable Batteries. *Adv. Mater.* **2013**, *25* (45), 6547–6553.
(25) Hu, Y.; Chen, W.; Lei, T.; Jiao, Y.; Huang, J.; Hu, A.; Gong, C.; Yan, C.; Wang, X.; Xiong, J. Strategies toward High-Loading Lithium–Sulfur Battery. *Adv. Energy Mater.* **2020**, *10* (17), 2000082–2000100.
(26) Hart, C. J.; Cuisinier, M.; Liang, X.; Kundu, D.; Garsuch, A.; Nazar, L. F. Rational Design of Sulphur Host Materials for Li-S Batteries: Correlating Lithium Polysulphide Adsorptivity and Self-Discharge Capacity Loss. *Chem. Commun.* **2015**, *51* (12), 2308–2311.
(27) Ji, X.; Lee, K. T.; Nazar, L. F. A Highly Ordered Nanostructured Carbon-Sulphur Cathode for Lithium-Sulphur Batteries. *Nat. Mater.* **2009**, *8* (6), 500–506.
(28) Xin, S.; Gu, L.; Zhao, N. H.; Yin, Y. X.; Zhou, L. J.; Guo, Y. G.; Wan, L. J. Smaller Sulfur Molecules Promise Better Lithium'sulfur Batteries. *J. Am. Chem. Soc.* **2012**, *134* (45), 18510–18513.
(29) Li, X.; Cao, Y.; Qi, W.; Saraf, L. V; Xiao, J.; Nie, Z.; Mietek, J.; Zhang, J. G.; Schwenzer, B.; Liu, J. Optimization of Mesoporous Carbon Structures for Lithium-Sulfur Battery Applications. *J. Mater. Chem.* **2011**, *21* (41), 16603–16610.
(30) Weinberger, C.; Ren, S.; Hartmann, M.; Wagner, T.; Karaman, D. Ş.; Rosenholm, J. M.; Tiemann, M. Bimodal Mesoporous CMK-5 Carbon: Selective Pore Filling with Sulfur and SnO_2 for Lithium Battery Electrodes. *ACS Appl. Nano Mater.* **2018**, *1* (1), 455–462.
(31) Raccichini, R.; Varzi, A.; Passerini, S.; Scrosati, B. The Role of Graphene for Electrochemical Energy Storage. *Nat. Mater.* **2015**, *14* (3), 271–279.
(32) Hua, W.; Yang, Z.; Nie, H.; Li, Z.; Yang, J.; Guo, Z.; Ruan, C.; Chen, X.; Huang, S. Polysulfide-Scission Reagents for the Suppression of the Shuttle Effect in Lithium-Sulfur Batteries. *ACS Nano* **2017**, *11* (2), 2209–2218.
(33) Xu, N.; Qian, T.; Liu, X.; Liu, J.; Chen, Y.; Yan, C. Greatly Suppressed Shuttle Effect for Improved Lithium Sulfur Battery Performance through Short Chain Intermediates. *Nano Lett.* **2017**, *17* (1), 538–543.

(34) Liang, X.; Hart, C.; Pang, Q.; Garsuch, A.; Weiss, T.; Nazar, L. F. A Highly Efficient Polysulfide Mediator for Lithium-Sulfur Batteries. *Nat. Commun.* **2015**, *6* (1), 5682–5689.
(35) Zeng, T.; Hu, X.; Ji, P.; Zhou, G. Effects of Sulfur Carriers with Different Morphologies on Performances of Lithium–Sulfur Battery. *Solid State Ionics* **2016**, *291*, 47–68.
(36) Zhang, S.; Tsuzuki, S.; Ueno, K.; Dokko, K.; Watanabe, M. Upper Limit of Nitrogen Content in Carbon Materials. *Angew. Chemie - Int. Ed.* **2015**, *54* (4), 1302–1306.
(37) Song, J.; Xu, T.; Gordin, M. L.; Zhu, P.; Lv, D.; Jiang, Y. B.; Chen, Y.; Duan, Y.; Wang, D. Nitrogen-Doped Mesoporous Carbon Promoted Chemical Adsorption of Sulfur and Fabrication of High-Areal-Capacity Sulfur Cathode with Exceptional Cycling Stability for Lithium-Sulfur Batteries. *Adv. Funct. Mater.* **2014**, *24* (9), 1243–1250.
(38) Song, J.; Gordin, M. L.; Xu, T.; Chen, S.; Yu, Z.; Sohn, H.; Lu, J.; Ren, Y.; Duan, Y.; Wang, D. Strong Lithium Polysulfide Chemisorption on Electroactive Sites of Nitrogen-Doped Carbon Composites For High-Performance Lithium–Sulfur Battery Cathodes. *Angew. Chemie* **2015**, *127* (14), 4399–4403.
(39) Peng, H. J.; Hou, T. Z.; Zhang, Q.; Huang, J. Q.; Cheng, X. B.; Guo, M. Q.; Yuan, Z.; He, L. Y.; Wei, F. Strongly Coupled Interfaces between a Heterogeneous Carbon Host and a Sulfur-Containing Guest for Highly Stable Lithium-Sulfur Batteries: Mechanistic Insight into Capacity Degradation. *Adv. Mater. Interfaces* **2014**, *1* (7), 1400227–1400236.
(40) Pang, Q.; Kundu, D.; Cuisinier, M.; Nazar, L. F. Surface-Enhanced Redox Chemistry of Polysulphides on a Metallic and Polar Host for Lithium-Sulphur Batteries. *Nat. Commun.* **2014**, *5*, 4759–4766.
(41) Zheng, J.; Tian, J.; Wu, D.; Gu, M.; Xu, W.; Wang, C.; Gao, F.; Engelhard, M. H.; Zhang, J. G.; Liu, J.; et al. Lewis Acid-Base Interactions between Polysulfides and Metal Organic Framework in Lithium Sulfur Batteries. *Nano Lett.* **2014**, *14* (5), 2345–2352.
(42) Demir-Cakan, R.; Morcrette, M.; Nouar, F.; Davoisne, C.; Devic, T.; Gonbeau, D.; Dominko, R.; Serre, C.; Férey, G.; Tarascon, J. M. Cathode Composites for Li-S Batteries via the Use of Oxygenated Porous Architectures. *J. Am. Chem. Soc.* **2011**, *133* (40), 16154–16160.
(43) Pang, Q.; Liang, X.; Kwok, C. Y.; Nazar, L. F. Advances in Lithium-Sulfur Batteries Based on Multifunctional Cathodes and Electrolytes. *Nat. Energy* **2016**, *1* (9), 1–11.
(44) Peng, H. J.; Huang, J. Q.; Cheng, X. B.; Zhang, Q. Review on High-Loading and High-Energy Lithium–Sulfur Batteries. *Adv. Energy Mater.* **2017**, *7* (24), 1700260–1200313.
(45) Liu, J.; Sun, M.; Zhang, Q.; Dong, F.; Kaghazchi, P.; Fang, Y.; Zhang, S.; Lin, Z. A Robust Network Binder with Dual Functions of Cu2+ Ions as Ionic Crosslinking and Chemical Binding Agents for Highly Stable Li-S Batteries. *J. Mater. Chem. A* **2018**, *6* (17), 7382–7388.
(46) Nakazawa, T.; Ikoma, A.; Kido, R.; Ueno, K.; Dokko, K.; Watanabe, M. Effects of Compatibility of Polymer Binders with Solvate Ionic Liquid Electrolytes on Discharge and Charge Reactions of Lithium-Sulfur Batteries. *J. Power Sources* **2016**, *307*, 746–752.
(47) Lacey, M. J.; Jeschull, F.; Edstrom, K.; Brandell, D. Why PEO as a Binder or Polymer Coating Increases Capacity in the Li-S System. *Chem. Commun.* **2013**, *49* (76), 8531–8533.
(48) Frischmann, P. D.; Hwa, Y.; Cairns, E. J.; Helms, B. A. Redox-Active Supramolecular Polymer Binders for Lithium-Sulfur Batteries That Adapt Their Transport Properties in Operando. *Chem. Mater.* **2016**, *28* (20), 7414–7421.
(49) Han, P.; Chung, S. H.; Chang, C. H.; Manthiram, A. Bifunctional Binder with

Nucleophilic Lithium Polysulfide Immobilization Ability for High-Loading, High-Thickness Cathodes in Lithium-Sulfur Batteries. *ACS Appl. Mater. Interfaces* **2019**, *11* (19), 17393–17399.

(50) Han, P.; Chung, S. H.; Chang, C. H.; Manthiram, A. Bifunctional Binder with Nucleophilic Lithium Polysulfide Immobilization Ability for High-Loading, High-Thickness Cathodes in Lithium-Sulfur Batteries. *ACS Appl. Mater. Interfaces* **2019**, *11* (19), 17393–17399.

(51) Lacey, M. J.; Jeschull, F.; Edström, K.; Brandell, D. Why PEO as a Binder or Polymer Coating Increases Capacity in the Li–S System. *Chem. Commun* **2013**, *49*, 8531–8533.

(52) Chen, J.; Henderson, W. A.; Pan, H.; Perdue, B. R.; Cao, R.; Hu, J. Z.; Wan, C.; Han, K. S.; Mueller, K. T.; Zhang, J. G.; et al. Improving Lithium-Sulfur Battery Performance under Lean Electrolyte through Nanoscale Confinement in Soft Swellable Gels. *Nano Lett.* **2017**, *17* (5), 3061–3067.

(53) Zhang, H.; Hu, X.; Zhang, Y.; Wang, S.; Xin, F.; Chen, X.; Yu, D. 3D-Crosslinked Tannic Acid/Poly(Ethylene Oxide) Complex as a Three-in-One Multifunctional Binder for High-Sulfur-Loading and High-Stability Cathodes in Lithium-Sulfur Batteries. *Energy Storage Mater.* **2019**, *17*, 293–299.

(54) Chen, W.; Qian, T.; Xiong, J.; Xu, N.; Liu, X.; Liu, J.; Zhou, J.; Shen, X.; Yang, T.; Chen, Y.; et al. A New Type of Multifunctional Polar Binder: Toward Practical Application of High Energy Lithium Sulfur Batteries. *Adv. Mater.* **2017**, *29* (12), 1605160–1605166.

(55) Ai, G.; Dai, Y.; Ye, Y.; Mao, W.; Wang, Z.; Zhao, H.; Chen, Y.; Zhu, J.; Fu, Y.; Battaglia, V.; et al. Investigation of Surface Effects through the Application of the Functional Binders in Lithium Sulfur Batteries. *Nano Energy* **2015**, *16*, 28–37.

(56) Liu, J.; Galpaya, D. G. D.; Yan, L.; Sun, M.; Lin, Z.; Yan, C.; Liang, C.; Zhang, S. Exploiting a Robust Biopolymer Network Binder for an Ultrahigh-Areal-Capacity Li-S Battery. *Energy Environ. Sci.* **2017**, *10* (3), 750–755.

(57) Sun, J.; Sun, Y.; Pasta, M.; Zhou, G.; Li, Y.; Liu, W.; Xiong, F.; Cui, Y. Entrapment of Polysulfides by a Black-Phosphorus-Modified Separator for Lithium-Sulfur Batteries. *Adv. Mater.* **2016**, *28* (44), 9797–9803.

(58) Bai, S.; Liu, X.; Zhu, K.; Wu, S.; Zhou, H. Metal-Organic Framework-Based Separator for Lithium-Sulfur Batteries. *Nat. Energy* **2016**, *1* (7), 1–6.

(59) Hwang, J. Y.; Kim, H. M.; Shin, S.; Sun, Y. K. Designing a High-Performance Lithium–Sulfur Batteries Based on Layered Double Hydroxides–Carbon Nanotubes Composite Cathode and a Dual-Functional Graphene–Polypropylene–Al2O3 Separator. *Adv. Funct. Mater.* **2018**, *28* (3), 1704294–1704305.

(60) Ghazi, Z. A.; He, X.; Khattak, A. M.; Khan, N. A.; Liang, B.; Iqbal, A.; Wang, J.; Sin, H.; Li, L.; Tang, Z. MoS2/Celgard Separator as Efficient Polysulfide Barrier for Long-Life Lithium-Sulfur Batteries. *Adv. Mater.* **2017**, *29* (21), 1606817–1606822.

(61) Wang, G.; Lai, Y.; Zhang, Z.; Li, J.; Zhang, Z. Enhanced Rate Capability and Cycle Stability of Lithium–Sulfur Batteries with a Bifunctional MCNT@PEG-Modified Separator. *J. Mater. Chem. A* **2015**, *3* (13), 7139–7144.

(62) Zhou, W.; Yu, Y.; Chen, H.; Disalvo, F. J.; Abruña, H. D. Yolk-Shell Structure of Polyaniline-Coated Sulfur for Lithium-Sulfur Batteries. *J. Am. Chem. Soc.* **2013**, *135* (44), 16736–16743.

(63) Meini, S.; Elazari, R.; Rosenman, A.; Garsuch, A.; Aurbach, D. The Use of Redox Mediators for Enhancing Utilization of Li2S Cathodes for Advanced Li-S Battery

Systems. *J. Phys. Chem. Lett.* **2014**, *5* (5), 915–918.
(64) Ponraj, R.; Kannan, A. G.; Ahn, J. H.; Kim, D. W. Improvement of Cycling Performance of Lithium-Sulfur Batteries by Using Magnesium Oxide as a Functional Additive for Trapping Lithium Polysulfide. *ACS Appl. Mater. Interfaces* **2016**, *8* (6), 4000–4006.
(65) Wang, N.; Hong, Y.; Liu, T. X.; Wang, Q.; Huang, J. Sucrose Derived Microporous-Mesoporous Carbon for Advanced Lithium-Sulfur Batteries. *Ceram. Int.* **2021**, *47*, 899–906.
(66) Schuster, J.; He, G.; Mandlmeier, B.; Yim, T.; Lee, K. T.; Bein, T.; Nazar, L. F. Spherical Ordered Mesoporous Carbon Nanoparticles with High Porosity for Lithium-Sulfur Batteries. *Angew. Chemie - Int. Ed.* **2012**, *51* (15), 3591–3595.
(67) Cao, J.; Chen, C.; Zhao, Q.; Zhang, N.; Lu, Q.; Wang, X.; Niu, Z.; Chen, J. A Flexible Nanostructured Paper of a Reduced Graphene Oxide–Sulfur Composite for High-Performance Lithium–Sulfur Batteries with Unconventional Configurations. *Adv. Mater.* **2016**, *28* (43), 9629–9636.
(68) Sun, Z.; Zhang, J.; Yin, L.; Hu, G.; Fang, R.; Cheng, H.-M.; Li, F. Conductive Porous Vanadium Nitride/Graphene Composite as Chemical Anchor of Polysulfides for Lithium-Sulfur Batteries. *Nat. Commun.* **2017**, *8*, 14627–14634.
(69) Li, Y.; Murphy, I. A.; Chen, Y.; Lin, F.; Wang, X.; Wang, S.; Hubble, D.; Jang, S. H.; Muller, K. T.; Wang, C.; et al. A Multi-Functional Interface Derived from Thiol-Modified Mesoporous Carbon in Lithium-Sulfur Batteries. *J. Mater. Chem. A* **2019**, *7* (21), 13372–13381.
(70) Chen, W.; Lei, T.; Qian, T.; Lv, W.; He, W.; Wu, C.; Liu, X.; Liu, J.; Chen, B.; Yan, C.; et al. A New Hydrophilic Binder Enabling Strongly Anchoring Polysulfides for High-Performance Sulfur Electrodes in Lithium-Sulfur Battery. *Adv. Energy Mater.* **2018**, *8* (12), 1702889–1702896.
(71) Yuan, J. J.; Kong, Q. R.; Huang, Z.; Song, Y. Z.; Li, M. Y.; Fang, L. F.; Zhu, B. K.; Li, H. Y. A Well-Designed Polymer as a Three-in-One Multifunctional Binder for High-Performance Lithium-Sulfur Batteries. *J. Mater. Chem. A* **2021**, *9* (5), 2970–2979.
(72) Liao, J.; Wang, J.; Liu, Z.; Ye, Z. Polar Benzimidazole-Containing (Sulfonated) Poly(Arylene Ether Ketone)s as Bifunctional Binders for Lithium-Sulfur Battery Cathodes with High Sulfur Loadings. *ACS Appl. Energy Mater.* **2019**, *2* (9), 6732–6740.
(73) Hwa, Y.; Frischmann, P. D.; Helms, B. A.; Cairns, E. J. Aqueous-Processable Redox-Active Supramolecular Polymer Binders for Advanced Lithium/Sulfur Cells. *Chem. Mater.* **2018**, *30* (3), 685–691.
(74) Lu, Z.; Sui, F.; Miao, Y. E.; Liu, G.; Li, C.; Dong, W.; Cui, J.; Liu, T.; Wu, J.; Yang, C. Polyimide Separators for Rechargeable Batteries. *J. Energy Chem.* **2021**, *58*, 170–197.
(75) Hernández, G.; Lago, N.; Shanmukaraj, D.; Armand, M.; Mecerreyes, D. Polyimide-Polyether Binders–Diminishing the Carbon Content in Lithium[Sbnd]Sulfur Batteries. *Mater. Today Energy* **2017**, *6*, 264–270.
(76) Xie, J.; Peng, H. J.; Song, Y. W.; Li, B. Q.; Xiao, Y.; Zhao, M.; Yuan, H.; Huang, J. Q.; Zhang, Q. Spatial and Kinetic Regulation of Sulfur Electrochemistry on Semi-Immobilized Redox Mediators in Working Batteries. *Angew. Chemie - Int. Ed.* **2020**, *59* (40), 17670–17675.
(77) Liang, X.; Kwok, C. Y.; Lodi-Marzano, F.; Pang, Q.; Cuisinier, M.; Huang, H.; Hart, C. J.; Houtarde, D.; Kaup, K.; Sommer, H.; et al. Tuning Transition Metal Oxide-Sulfur Interactions for Long Life Lithium Sulfur Batteries: The "Goldilocks" Principle. *Adv.*

Energy Mater. **2016**, *6* (6), 1501636–1501644.
(78) Yuan, H.; Peng, H. J.; Li, B. Q.; Xie, J.; Kong, L.; Zhao, M.; Chen, X.; Huang, J. Q.; Zhang, Q. Conductive and Catalytic Triple-Phase Interfaces Enabling Uniform Nucleation in High-Rate Lithium–Sulfur Batteries. *Adv*. *Energy Mater*. **2019**, *9* (1), 1802768–1802775.
(79) Liang, X.; Nazar, L. F. In Situ Reactive Assembly of Scalable Core-Shell Sulfur-MnO2 Composite Cathodes. *ACS Nano* **2016**, *10* (4), 4192–4198.
(80) Wang, Y.; Zhang, R.; Chen, J.; Wu, H.; Lu, S.; Wang, K.; Li, H.; Harris, C. J.; Xi, K.; Kumar, R. V.; et al. Enhancing Catalytic Activity of Titanium Oxide in Lithium–Sulfur Batteries by Band Engineering. *Adv*. *Energy Mater*. **2019**, *9* (24), 1900953–1900963.
(81) Reiner, B. R.; Foxman, B. M.; Wade, C. R. Electrochemical and Structural Investigation of the Interactions between Naphthalene Diimides and Metal Cations. *Dalt*. *Trans*. **2017**, *46* (29), 9472–9480.
(82) Genene, Z.; Mammo, W.; Wang, E.; Andersson, M. R. Recent Advances in N-Type Polymers for All-Polymer Solar Cells. *Adv*. *Mater*. **2019**, *31* (22), 1807275–1807314.
(83) Jung, B. J.; Lee, K.; Sun, J.; Andreou, A. G.; Katz, H. E. Air-Operable, High-Mobility Organic Transistors with Semifluorinated Side Chains and Unsubstituted Naphthalenetetracarboxylic Diimide Cores: High Mobility and Environmental and Bias Stress Stability from the Perfluorooctylpropyl Side Chain. *Adv*. *Funct*. *Mater*. **2010**, *20* (17), 2930–2944.
(84) Jung, J. W.; Jo, J. W.; Chueh, C. C.; Liu, F.; Jo, W. H.; Russell, T. P.; Jen, A. K.-Y. Fluoro-Substituted n-Type Conjugated Polymers for Additive-Free All-Polymer Bulk Heterojunction Solar Cells with High Power Conversion Efficiency of 6.71%. *Adv*. *Mater*. **2015**, *27* (21), 3310–3317.
(85) Tachikawa, N.; Yamauchi, K.; Takashima, E.; Park, J. W.; Dokko, K.; Watanabe, M. Reversibility of Electrochemical Reactions of Sulfur Supported on Inverse Opal Carbon in Glyme-Li Salt Molten Complex Electrolytes. *Chem*. *Commun*. **2011**, *47* (28), 8157–8159.
(86) Seh, Z. W.; Zhang, Q.; Li, W.; Zheng, G.; Yao, H.; Cui, Y. Stable Cycling of Lithium Sulfide Cathodes through Strong Affinity with a Bifunctional Binder. *Chem*. *Sci*. **2013**, *4* (9), 3673–3677.
(87) Ma, L.; Zhuang, H.; Lu, Y.; Moganty, S. S.; Hennig, R. G.; Archer, L. A. Tethered Molecular Sorbents: Enabling Metal-Sulfur Battery Cathodes. *Adv*. *Energy Mater*. **2014**, *4* (17), 1400390–1400398.
(88) Chen, H.; Wang, C.; Dai, Y.; Qiu, S.; Yang, J.; Lu, W.; Chen, L. Rational Design of Cathode Structure for High Rate Performance Lithium-Sulfur Batteries. *Nano Lett*. **2015**, *15* (8), 5443–5448.
(89) Sun, K.; Zhang, Q.; Bock, D. C.; Tong, X.; Su, D.; Marschilok, A. C.; Takeuchi, K. J.; Takeuchi, E. S.; Gan, H. Interaction of TiS 2 and Sulfur in Li-S Battery System. *J*. *Electrochem*. *Soc*. **2017**, *164* (6), 1291–1297.
(90) Liao, J.; Liu, Z.; Liu, X.; Ye, Z. Water-Soluble Linear Poly(Ethylenimine) as a Superior Bifunctional Binder for Lithium-Sulfur Batteries of Improved Cell Performance. *J*. *Phys*. *Chem*. *C* **2018**, *122* (45), 25917–25929.
(91) Pang, Q.; Kundu, D.; Cuisinier, M.; Nazar, L. F. Surface-Enhanced Redox Chemistry of Polysulphides on a Metallic and Polar Host for Lithium-Sulphur Batteries. *Nat*. *Commun*. **2014**, *5*, 1–8.
(92) Cuisinier, M.; Cabelguen, P. E.; Evers, S.; He, G.; Kolbeck, M.; Garsuch, A.; Bolin, T.;

Balasubramanian, M.; Nazar, L. F. Sulfur Speciation in Li-S Batteries Determined by Operando X-Ray Absorption Spectroscopy. *J. Phys. Chem. Lett.* **2013**, *4* (19), 3227–3232.
(93) Druschel, G. K.; Hamers, R. J.; Banfield, J. F. Kinetics and Mechanism of Polythionate Oxidation to Sulfate at Low PH by O2 and Fe3+. *Geochim. Cosmochim. Acta* **2003**, *67* (23), 4457–4469.
(94) Yang, Y.; Zheng, G.; Misra, S.; Nelson, J.; Toney, M. F.; Cui, Y. High-Capacity Micrometer-Sized Li 2S Particles as Cathode Materials for Advanced Rechargeable Lithium-Ion Batteries. *J. Am. Chem. Soc.* **2012**, *134* (37), 15387–15394.
(95) Qin, J.; Lin, F.; Hubble, D.; Wang, Y.; Li, Y.; Murphy, I. A.; Jang, S. H.; Yang, J.; Jen, A. K. Y. Tuning Self-Healing Properties of Stiff, Ion-Conductive Polymers. *J. Mater. Chem. A* **2019**, *7* (12), 6773–6783.
(96) Someya, T.; Bao, Z.; Malliaras, G. G. The Rise of Plastic Bioelectronics. *Nature* **2016**, *540* (7633), 379–385.
(97) Tee, B. C. K.; Wang, C.; Allen, R.; Bao, Z. An Electrically and Mechanically Self-Healing Composite with Pressure- and Flexion-Sensitive Properties for Electronic Skin Applications. *Nat Nano* **2012**, *7* (12), 825–832.
(98) Cao, Y.; Morrissey, T. G.; Acome, E.; Allec, S. I.; Wong, B. M.; Keplinger, C.; Wang, C. A Transparent, Self-Healing, Highly Stretchable Ionic Conductor. *Adv. Mater.* **2017**, *29* (10), 1605099–1605107.
(99) Li, C.-H.; Wang, C.; Keplinger, C.; Zuo, J.-L.; Jin, L.; Sun, Y.; Zheng, P.; Cao, Y.; Lissel, F.; Linder, C.; et al. A Highly Stretchable Autonomous Self-Healing Elastomer. *Nat Chem* **2016**, *8* (6), 618–624.
(100) Liu, X.; Su, G.; Guo, Q.; Lu, C.; Zhou, T.; Zhou, C.; Zhang, X. Hierarchically Structured Self-Healing Sensors with Tunable Positive/Negative Piezoresistivity. *Adv. Funct. Mater.* **2018**, *28* (15), 1706658–1706667.
(101) Choi, S.; Kwon, T.-W.; Coskun, A.; Choi, J. W. Highly Elastic Binders Integrating Polyrotaxanes for Silicon Microparticle Anodes in Lithium Ion Batteries. *Science* **2017**, *357* (6348), 279–283.
(102) Wu, H.; Chan, G.; Choi, J. W.; Ryu, I.; Yao, Y.; McDowell, M. T.; Lee, S. W.; Jackson, A.; Yang, Y.; Hu, L.; et al. Stable Cycling of Double-Walled Silicon Nanotube Battery Anodes through Solid–Electrolyte Interphase Control. *Nat. Nanotechnol.* **2012**, *7* (5), 310–315.
(103) Wu, M.; Xiao, X.; Vukmirovic, N.; Xun, S.; Das, P. K.; Song, X.; Olalde-Velasco, P.; Wang, D.; Weber, A. Z.; Wang, L.-W.; et al. Toward an Ideal Polymer Binder Design for High-Capacity Battery Anodes. *J. Am. Chem. Soc.* **2013**, *135* (32), 12048–12056.
(104) Wang, C.; Wu, H.; Chen, Z.; McDowell, M. T.; Cui, Y.; Bao, Z. Self-Healing Chemistry Enables the Stable Operation of Silicon Microparticle Anodes for High-Energy Lithium-Ion Batteries. *Nat. Chem.* **2013**, *5* (12), 1042–1048.
(105) Whiteley, J. M.; Taynton, P.; Zhang, W.; Lee, S.-H. Ultra-Thin Solid-State Li-Ion Electrolyte Membrane Facilitated by a Self-Healing Polymer Matrix. *Adv. Mater.* **2015**, *27* (43), 6922–6927.
(106) Cheng, H.; Huang, Y.; Cheng, Q.; Shi, G.; Jiang, L.; Qu, L. Self-Healing Graphene Oxide Based Functional Architectures Triggered by Moisture. *Adv. Funct. Mater.* **2017**, *27* (42), 1703096–1703103.
(107) Rao, Y.; Chortos, A.; Pfattner, R.; Lissel, F.; Chiu, Y.; Feig, V.; Xu, J.; Kurosawa, T.; Gu, X.; Wang, C.; et al. Stretchable Self-Healing Polymeric Dielectrics Cross-Linked Through

Metal–Ligand Coordination. *J. Am. Chem. Soc.* **2016**, *138* (18), 6020–6027.
(108) Oh, J. Y.; Rondeau-Gagné, S.; Chiu, Y.-C.; Chortos, A.; Lissel, F.; Wang, G.-J. N.; Schroeder, B. C.; Kurosawa, T.; Lopez, J.; Katsumata, T.; et al. Intrinsically Stretchable and Healable Semiconducting Polymer for Organic Transistors. *Nature* **2016**, *539* (7629), 411–415.
(109) Chortos, A.; Liu, J.; Bao, Z. Pursuing Prosthetic Electronic Skin. *Nat Mater* **2016**, *15* (9), 937–950.
(110) Neal, J. A.; Mozhdehi, D.; Guan, Z. Enhancing Mechanical Performance of a Covalent Self-Healing Material by Sacrificial Noncovalent Bonds. *J. Am. Chem. Soc.* **2015**, *137* (14), 4846–4850.
(111) Cordier, P.; Tournilhac, F.; Soulié-Ziakovic, C.; Leibler, L. Self-Healing and Thermoreversible Rubber from Supramolecular Assembly. *Nature* **2008**, *451* (7181), 977–980.
(112) Nakahata, M.; Takashima, Y.; Yamaguchi, H.; Harada, A. Redox-Responsive Self-Healing Materials Formed from Host–Guest Polymers. *Nat. Commun.* **2011**, *2*, 511–516.
(113) Ur Rehman, H.; Chen, Y.; Hedenqvist, M. S.; Li, H.; Xue, W.; Guo, Y.; Guo, Y.; Duan, H.; Liu, H. Self-Healing Shape Memory PUPCL Copolymer with High Cycle Life. *Adv. Funct. Mater.* **2018**, *28* (7), 1704109–1704122.
(114) Faghihnejad, A.; Feldman, K. E.; Yu, J.; Tirrell, M. V.; Israelachvili, J. N.; Hawker, C. J.; Kramer, E. J.; Zeng, H. Adhesion and Surface Interactions of a Self-Healing Polymer with Multiple Hydrogen-Bonding Groups. *Adv. Funct. Mater.* **2014**, *24* (16), 2322–2333.
(115) Zhou, B.; He, D.; Hu, J.; Ye, Y.; Peng, H.; Zhou, X.; Xie, X.; Xue, Z. A Flexible, Self-Healing and Highly Stretchable Polymer Electrolyte *via* Quadruple Hydrogen Bonding for Lithium-Ion Batteries. *J. Mater. Chem. A* **2018**, *6* (25), 11725–11733.
(116) Kim, D.; Hyun, S.; Han, S. M. Freestanding Silicon Microparticle and Self-Healing Polymer Composite Design for Effective Lithiation Stress Relaxation. *J. Mater. Chem. A* **2018**, *6* (24), 11353–11361.
(117) Yang, D.; Wang, Y.; Li, Z.; Xu, Y.; Cheng, F.; Li, P.; Li, H. Color-Tunable Luminescent Hydrogels with Tough Mechanical Strength and Self-Healing Ability. *J. Mater. Chem. C* **2018**, *6* (5), 1153–1159.
(118) Mozhdehi, D.; Ayala, S.; Cromwell, O. R.; Guan, Z. Self-Healing Multiphase Polymers via Dynamic Metal–Ligand Interactions. *J. Am. Chem. Soc.* **2014**, *136* (46), 16128–16131.
(119) Cromwell, O. R.; Chung, J.; Guan, Z. Malleable and Self-Healing Covalent Polymer Networks through Tunable Dynamic Boronic Ester Bonds. *J. Am. Chem. Soc.* **2015**, *137* (20), 6492–6495.
(120) Hart, L. R.; Hunter, J. H.; Nguyen, N. A.; Harries, J. L.; Greenland, B. W.; Mackay, M. E.; Colquhoun, H. M.; Hayes, W. Multivalency in Healable Supramolecular Polymers: The Effect of Supramolecular Cross-Link Density on the Mechanical Properties and Healing of Non-Covalent Polymer Networks. *Polym. Chem.* **2014**, *5* (11), 3680–3688.
(121) Feldman, K. E.; Kade, M. J.; Meijer, E. W.; Hawker, C. J.; Kramer, E. J. Model Transient Networks from Strongly Hydrogen-Bonded Polymers. *Macromolecules* **2009**, *42* (22), 9072–9081.
(122) Hentschel, J.; Kushner, A. M.; Ziller, J.; Guan, Z. Self-Healing Supramolecular Block Copolymers. *Angew. Chemie Int. Ed.* **2012**, *51* (42), 10561–10565.
(123) Chen, Y.; Kushner, A. M.; Williams, G. A.; Guan, Z. Multiphase Design of Autonomic Self-Healing Thermoplastic Elastomers. *Nat Chem* **2012**, *4* (6), 467–472.

(124) Williams, G. A.; Ishige, R.; Cromwell, O. R.; Chung, J.; Takahara, A.; Guan, Z. Mechanically Robust and Self-Healable Superlattice Nanocomposites by Self-Assembly of Single-Component "Sticky" Polymer-Grafted Nanoparticles. *Adv. Mater.* **2015**, *27* (26), 3934–3941.
(125) Fox, J.; Wie, J. J.; Greenland, B. W.; Burattini, S.; Hayes, W.; Colquhoun, H. M.; MacKay, M. E.; Rowan, S. J. High-Strength, Healable, Supramolecular Polymer Nanocomposites. *J. Am. Chem. Soc.* **2012**, *134* (11), 5362–5368.
(126) Kovalenko, I.; Zdyrko, B.; Magasinski, A.; Hertzberg, B.; Milicev, Z.; Burtovyy, R.; Luzinov, I.; Yushin, G. A Major Constituent of Brown Algae for Use in High-Capacity Li-Ion Batteries. *Science* **2011**, *334* (6052), 75–79.
(127) Shi, Y.; Zhou, X.; Yu, G. Material and Structural Design of Novel Binder Systems for High-Energy, High-Power Lithium-Ion Batteries. *Acc. Chem. Res.* **2017**, *50* (11), 2642–2652.
(128) Carpi, F.; Bauer, S.; De Rossi, D. Stretching Dielectric Elastomer Performance. *Science (80-.).* **2010**, *330* (6012), 1759–1761.
(129) Mannsfeld, S. C. B.; Tee, B. C. K.; Stoltenberg, R. M.; Chen, C. V. H. H.; Barman, S.; Muir, B. V. O.; Sokolov, A. N.; Reese, C.; Bao, Z. Highly Sensitive Flexible Pressure Sensors with Microstructured Rubber Dielectric Layers. *Nat Mater* **2010**, *9* (10), 859–864.
(130) Leng, F.; Tan, C. M.; Pecht, M. Effect of Temperature on the Aging Rate of Li Ion Battery Operating above Room Temperature. *Sci. Rep.* **2015**, *5* (1), 12967–12978.
(131) Bandhauer, T. M.; Garimella, S.; Fuller, T. F. A Critical Review of Thermal Issues in Lithium-Ion Batteries. *J. Electrochem. Soc.* **2011**, *158* (3), 1–25.
(132) Chen, Y.; Lu, B.; Chen, Y.; Feng, X. Breathable and Stretchable Temperature Sensors Inspired by Skin. *Sci. Rep.* **2015**, *5* (1), 11505–11515.
(133) Bandodkar, A. J.; Jia, W.; Yardımcı, C.; Wang, X.; Ramirez, J.; Wang, J. Tattoo-Based Noninvasive Glucose Monitoring: A Proof-of-Concept Study. *Anal. Chem.* **2015**, *87* (1), 394–398.
(134) Grindy, S. C.; Learsch, R.; Mozhdehi, D.; Cheng, J.; Barrett, D. G.; Guan, Z.; Messersmith, P. B.; Holten-Andersen, N. Control of Hierarchical Polymer Mechanics with Bioinspired Metal-Coordination Dynamics. *Nat Mater* **2015**, *14* (12), 1210–1216.
(135) Vadehra, G. S.; Maloney, R. P.; Garcia-Garibay, M. A.; Dunn, B. Naphthalene Diimide Based Materials with Adjustable Redox Potentials: Evaluation for Organic Lithium-Ion Batteries. *Chem. Mater.* **2014**, *26* (24), 7151–7157.
(136) Nielsen, M. B.; Jeppesen, J. O.; Laut, J.; Lomholt, C.; Damgaard, D.; Jacobsen, J. P.; Becher, J.; Stoddart, J. F. Binding Studies between Tetrathiafulvalene Derivatives and Cyclobis(Paraquat-p-Phenylene). *J. Org. Chem.* **2001**, *66* (10), 3559–3563.
(137) Greenland, B. W.; Burattini, S.; Hayes, W.; Colquhoun, H. M. Design, Synthesis and Computational Modelling of Aromatic Tweezer-Molecules as Models for Chain-Folding Polymer Blends. *Tetrahedron* **2008**, *64* (36), 8346–8354.
(138) Ahn, B. K.; Lee, D. W.; Israelachvili, J. N.; Waite, J. H. Surface-Initiated Self-Healing of Polymers in Aqueous Media. *Nat. Mater.* **2014**, *13* (9), 867–872.
(139) Roy, N.; Bruchmann, B.; Lehn, J.-M. DYNAMERS: Dynamic Polymers as Self-Healing Materials. *Chem. Soc. Rev.* **2015**, *44* (11), 3786–3807.
(140) Taylor, D. L.; in het Panhuis, M. Self-Healing Hydrogels. *Adv. Mater.* **2016**, *28* (41), 9060–9093.
(141) Wei, Z.; Yang, J. H.; Liu, Z. Q.; Xu, F.; Zhou, J. X.; Zrínyi, M.; Osada, Y.; Chen, Y. M.

Novel Biocompatible Polysaccharide-Based Self-Healing Hydrogel. *Adv. Funct. Mater.* **2015**, *25* (9), 1352–1359.
(142) Li, C.-H.; Wang, C.; Keplinger, C.; Zuo, J.-L.; Jin, L.; Sun, Y.; Zheng, P.; Cao, Y.; Lissel, F.; Linder, C.; et al. A Highly Stretchable Autonomous Self-Healing Elastomer. *Nat. Chem.* **2016**, *8* (6), 618–624.
(143) Burattini, S.; Greenland, B. W.; Merino, D. H.; Weng, W.; Seppala, J.; Colquhoun, H. M.; Hayes, W.; Mackay, M. E.; Hamley, I. W.; Rowan, S. J. A Healable Supramolecular Polymer Blend Based on Aromatic Π–π Stacking and Hydrogen-Bonding Interactions. *J. Am. Chem. Soc.* **2010**, *132* (34), 12051–12058.
(144) Nan, C.; Lin, Z.; Liao, H.; Song, M. K.; Li, Y.; Cairns, E. J. Durable Carbon-Coated Li2S Core-Shell Spheres for High Performance Lithium/Sulfur Cells. *J. Am. Chem. Soc.* **2014**, *136* (12), 4659–4663.
(145) Zhou, W.; Xiao, X.; Cai, M.; Yang, L. Polydopamine-Coated, Nitrogen-Doped, Hollow Carbon-Sulfur Double-Layered Core-Shell Structure for Improving Lithium-Sulfur Batteries. *Nano Lett.* **2014**, *14* (9), 5250–5256.
(146) Seh, Z. W.; Li, W.; Cha, J. J.; Zheng, G.; Yang, Y.; McDowell, M. T.; Hsu, P. C.; Cui, Y. Sulphur-TiO2 Yolk-Shell Nanoarchitecture with Internal Void Space for Long-Cycle Lithium-Sulphur Batteries. *Nat. Commun.* **2013**, *4*, 1331–1336.
(147) Zhang, C.; Lv, W.; Tao, Y.; Yang, Q. H. Towards Superior Volumetric Performance: Design and Preparation of Novel Carbon Materials for Energy Storage. *Energy Environ. Sci.* **2015**, *8* (5), 1390–1403.
(148) Peng, H. J.; Huang, J. Q.; Cheng, X. B.; Zhang, Q. Review on High-Loading and High-Energy Lithium–Sulfur Batteries. *Adv. Energy Mater.* **2017**, *7* (24), 1700260–1200313.
(149) Wang, F.; Li, L.; Yang, X.; You, J.; Xu, Y.; Wang, H.; Ma, Y.; Gao, G. Influence of Additives in a PVDF-Based Solid Polymer Electrolyte on Conductivity and Li-Ion Battery Performance. *Sustain. Energy Fuels* **2018**, *2* (2), 492–498.
(150) Burnworth, M.; Tang, L.; Kumpfer, J. R.; Duncan, A. J.; Beyer, F. L.; Fiore, G. L.; Rowan, S. J.; Weder, C. Optically Healable Supramolecular Polymers. *Nature* **2011**, *472* (7343), 334–337.
(151) Sun, J.-Y.; Zhao, X.; Illeperuma, W. R. K.; Chaudhuri, O.; Oh, K. H.; Mooney, D. J.; Vlassak, J. J.; Suo, Z. Highly Stretchable and Tough Hydrogels. *Nature* **2012**, *489* (7414), 133–136.
(152) Pope, M. A.; Aksay, I. A. Structural Design of Cathodes for Li-S Batteries. *Adv. Energy Mater.* **2015**, *5* (16), 1500124–1500146.